

# Lawrence Berkeley National Laboratory

## Recent Work

**Title**

Tutorial: Reactive high power impulse magnetron sputtering (R-HiPIMS)

**Permalink**

<https://escholarship.org/uc/item/74s0t81f>

**Journal**

Journal of Applied Physics, 121(17)

**ISSN**

0021-8979

**Author**

Anders, A

**Publication Date**

2017-05-07

**DOI**

10.1063/1.4978350

Peer reviewed

Published in

Journal of Applied Physics **121**, 171101 (2017)

<http://doi.org/10.1063/1.4978350>

(get the original PDF from the link above, at no charge in 2017)

This tutorial is part of a *Special Topic Section on Reactive HiPIMS*, published by Journal of Applied Physics; for the collection go here:

<http://aip.scitation.org/toc/jap/121/17?expanded=121>

## **Tutorial: Reactive High Power Impulse Magnetron Sputtering (R-HiPIMS)**

**André Anders**

Lawrence Berkeley National Laboratory, 1 Cyclotron Road, Berkeley, California 94720, USA

Email: [aanders@lbl.gov](mailto:aanders@lbl.gov)

### **ACKNOWLEDGMENTS**

Contributions by many colleagues are gratefully acknowledged, especially by those who visited the Plasma Applications Group in Berkeley. Work at Lawrence Berkeley National Laboratory is supported by the U.S. Department of Energy under Contract No. DE-AC02-05CH11231.

## Abstract

High Power Impulse Magnetron Sputtering (HiPIMS) is a coatings technology that combines magnetron sputtering with pulsed power concepts. By applying power in pulses of high amplitude and relatively low duty cycle large fractions of sputtered atoms and near-target gases are ionized. In contrast to conventional magnetron sputtering, HiPIMS is characterized by self-sputtering or repeated gas recycling for high and low sputter yield materials, respectively, and both for most intermediate materials. The dense plasma in front of the target has the dual function of sustaining the discharge and providing plasma-assistance to film growth, affecting the microstructure of growing films. Many technologically interesting thin films are compound films, which are composed of one or more metals and a reactive gas, most often oxygen or nitrogen. When reactive gas is added non-trivial consequences arise for the system because the target may become “poisoned”, i.e., a compound layer forms on the target surface affecting the sputtering yield and the yield of secondary electron emission, and thereby all other parameters. It is emphasized that the target state depends not only on the reactive gas’ partial pressure (balanced via gas flow and pumping) but also on the ion flux to the target, which can be controlled by pulse parameters. This is a critical technological opportunity for reactive HiPIMS (R-HiPIMS). The scope of this tutorial is focused on plasma processes and mechanisms of operation, and only briefly touches upon film properties. It introduces R-HiPIMS in a systematic, step-by-step approach by covering sputtering, magnetron sputtering, reactive magnetron sputtering, pulsed reactive magnetron sputtering, HiPIMS, and finally R-HiPIMS. The tutorial is concluded by considering variations of R-HiPIMS known as Modulated Pulsed Power Magnetron Sputtering (MPPMS) and deep-oscillation magnetron sputtering (DOMS), and combinations of R-HiPIMS with superimposed dc magnetron sputtering.

## I. INTRODUCTION

Magnetron sputtering is a mature, widely used deposition technology for thin films. Its roots can be traced back to observations of (pulsed) diode sputtering by Grove in the middle of the 19<sup>th</sup> century.<sup>1</sup> Commercially viable device solutions, magnetrons, became available in the 1970s. This tutorial is not a review of the development of magnetron sputtering, and of the latest development in terms of high power impulse magnetron sputtering, HiPIMS, where power is applied in pulses of high power with no or little power applied between those pulses. Rather, this tutorial explains the underlying physics of the latest development of HiPIMS as applied to producing compound films and multilayers in a reactive gas environment. The literature is generously cited but no attempt is made to survey the field in a complete manner. The goal is to explain the logical steps leading to the development of reactive HiPIMS (R-HiPIMS), thereby providing a good foundation to understand and appreciate the contributions to the Special Topic Section of Journal of Applied Physics on R-HiPIMS. We start by briefly recalling the basics of sputtering in general and magnetron sputtering in particular. These sections are kept short as entire books have been written on the subject.<sup>2,3</sup> The next section deals with reactive magnetron sputtering, which is characterized by the presence of a reactive gas such as nitrogen or oxygen to produce nitride or oxide coatings. Also here, many papers and books have been written on the subject<sup>4</sup> and the treatment is for brief reference only. In the following section, the physics of HiPIMS is introduced – here we need to spend a bit more time since the field is still young and developing. After HiPIMS is explained, we can

make the step and combine the knowledge related to reactive magnetron sputtering and HiPIMS to arrive at the physics of R-HiPIMS.

## II. SPUTTERING

Sputtering is the process of removing surface atoms from a target by particle (usually ion) bombardment. The liberated surface atoms can move to a surface to be coated, the substrate, and may condense there, thereby contributing to forming a solid (thin) film or (thick) coating. Film nucleation and growth are fields of science on their own; we focus here on the sputtering process using a magnetron. Figure 1 illustrates that energetic ions, with energies of typically several 100 eV, penetrate the target and cause collision cascades in the target.

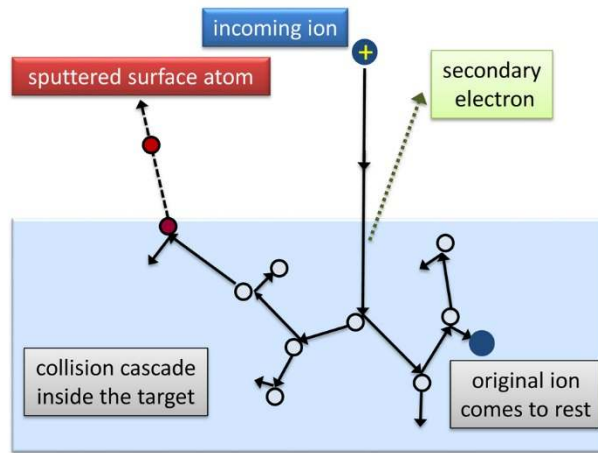


FIG. 1. Schematic illustration of the sputtering process: A collision cascade is triggered inside the target, caused by an energetic ion, knocking off one or more surface atoms. The fate of the original ion, which comes to rest in the target, depends on its chemical nature and will be discussed later in this tutorial. Besides surface atoms, secondary electrons may also be emitted – they play an important role in sustaining the discharge, as discussed later.

The penetration depth of ions, size of the collision cascade, and number of surface atoms removed depend on the mass and energy of ions as well as on the composition and structure of the target. Collision cascades are well understood based on theories of electronic and nuclear stopping powers, and most practically described by Monte Carlo modeling using the universal Ziegler-Biersack-Littmark (ZBL) potential.<sup>5,6</sup> In terms of film deposition by sputtering, an important parameter is the sputtering yield  $Y$ , defined as the ratio of the number of sputtered atoms,  $N_a$ , to the number of incident ions,  $N_i$ :

$$Y = N_a / N_i . \quad (1)$$

In order to cause any sputtering, the incoming ion needs to have a minimum threshold energy,  $E_{th}$ . The threshold energy is directly related to the surface binding energy,  $E_{SB}$ , and also depends on the mass of the incident ion  $M_i$  and the target atoms,  $M_a$ , respectively,<sup>7</sup>

$$E_{th} = E_{SB} \begin{cases} (1 + 5.7(M_i/M_a))/\Lambda & \text{for } M_i \leq M_a \\ 6.7/\Lambda & \text{for } M_i \geq M_a \end{cases} \quad (2)$$

where

$$\Lambda = \frac{4M_i M_a}{(M_i + M_a)^2} \quad (3)$$

is the energy transfer factor in an elastic collision.

The sputtering yield can very well be approximated by semi-empirical formula like those derived by Sigmund,<sup>8</sup> Bohdanský<sup>9</sup> or Yamamura and Tawara.<sup>7</sup> The latter, somewhat lengthy formula and its fitting parameters are provided in the *Supplementary Material*. Generally, the yield curves show a maximum between 10 and 100 keV (Fig. 2).

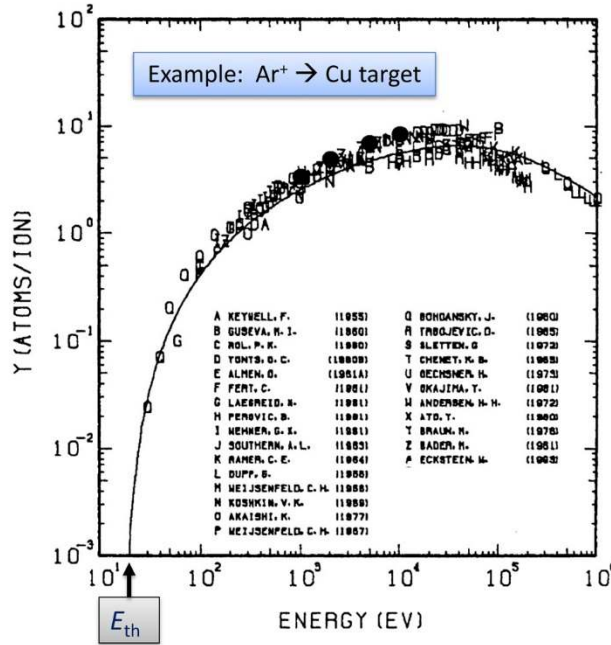


FIG. 2. Sputter yield as a function of ion energy for the example of argon ions impacting a copper target (Reprinted Fig. 120 of the compilation of data from Yamamura and Tawara,<sup>7</sup> with permission from Elsevier).

The practically used ion energies in sputtering are much lower than the range shown in Fig. 2. In the relevant energy range, between 300 eV and 3 keV, the yield functions  $Y(E_i)$  can be reasonably well fitted by a very simple allometric function

$$Y(E_i) = a E_i^b, \quad (4)$$

where the  $a$  and  $b$  are fit parameters for a given combination of ion and target materials (see *Supplementary Material*). Sputtering of the target by ions of the same material is called *self-sputtering*. For self-sputtering, the exponent  $b$  can be approximated by

$$b = 0.106 M^{0.387}, \quad (5)$$

where  $M$  is the atomic mass number of the self-sputtering element ( $M_i = M_a = M$ ).

Sputtered atoms have typically a few electron-volt (eV) of kinetic energy due to the ballistic processes in the collision cascade. This is described by the Thompson energy distribution<sup>10,11</sup>

$$f_{\text{Thompson}}(E) = \begin{cases} A \frac{E \left[ 1 - \sqrt{(E_{SB} + E)/\Lambda E_i} \right]}{(E + E_{SB})^3} & \text{if } 0 \leq E \leq \Lambda E_i \\ 0 & \text{if } E > \Lambda E_i \end{cases} \quad (6)$$

where  $\Lambda$  was defined by Eq. (3),  $A$  is a normalization factor,  $E_i$  is the energy of incident ions, and  $E_{SB}$  is the surface binding energy of the target atoms, which is listed in Table S1 for many elementary targets (*AIP Publishing add link here*). The symbol  $E$  is here used here for energy and should not be confused with electric field  $E$  used in later equations; the distinction is generally easily made from the context. The *energy* distribution function depends on the target material because it is essentially determined by the surface binding energy.<sup>12</sup>

$$f_{\text{Thompson}}(E) \propto \frac{E}{(E + E_{SB})^3}. \quad (7)$$

The distribution (7) has a peak at  $E_{SB}/2$  and falls with  $E^{-2}$ . Even the low energy atoms, i.e. those near the peak of the distribution, have several eV of kinetic energy, leading to the relatively high velocity of

$$v_a \approx (E_{SB}/M_a)^{1/2} \quad (8)$$

For example, a titanium atom (isotope 48,  $M_a = 48 \times 1.66 \times 10^{-27}$  kg,  $E_{SB}(\text{Ti}) = 3.30$  eV =  $5.3 \times 10^{-19}$  J) near the peak of the distribution would move away from the target with a velocity of about 2600 m/s. As a consequence, such atom would travel through the plasma near the target in a few  $\mu\text{s}$ , and the chance for ionization is small. Most sputtered species are neutral atoms although a small fraction of sputtered material is removed in clusters of atoms, which can be understood by collective phenomena in the collision cascade.<sup>13</sup>

A sputtered atom's kinetic energy and moment are very important to film deposition because the microstructure is affected provided the atom has not lost its energy due to collisions with the background gas. It is desirable to operate the coating process at low pressure such that the mean free path of the atom is comparable to or larger than the target-substrate distance. Operation of a plasma, producing the primary ions for sputtering, is enabled at low pressure when the plasma electrons are effectively used. This leads us to the magnetron, a sputtering device with effective electron trapping.

### III. MAGNETRON SPUTTERING

As the name suggests, the magnetron uses a magnet (most often, but not always, a permanent magnet) to effectively trap and utilize energetic electrons for ionization processes at low pressure. The magnetron discharge is a magnetically enhanced glow discharge. The magnetic field is used to “magnetize” electrons, which means that electrons can complete many gyrations, effectively allowing an electron to travel a much longer path in the same general space in front of the target than without magnet. This allows us to operate the magnetron discharge at a much lower pressure (typically 1 Pa or even lower) than a conventional glow discharges (typically 10 Pa or higher). Magnetization of electrons requires that the magnetic field is sufficiently strong so that the gyration radius

$$r_{g,e} = \frac{m_e u_{e\perp}}{eB}. \quad (9)$$

is much smaller than a characteristic device dimension; here  $u_{e\perp}$  is the electron’s velocity component perpendicular to the magnetic field vector  $\mathbf{B}$ ,  $e$  is the elementary charge, and  $m_e$  is the electron mass. A good characteristic dimension is the curvature radius of the magnetic field vector over the target, i.e., for all practical matters, about  $\sim 1$  cm (Fig. 3). The ions produced are accelerated by the electric field toward the target causing the desired target sputtering process.

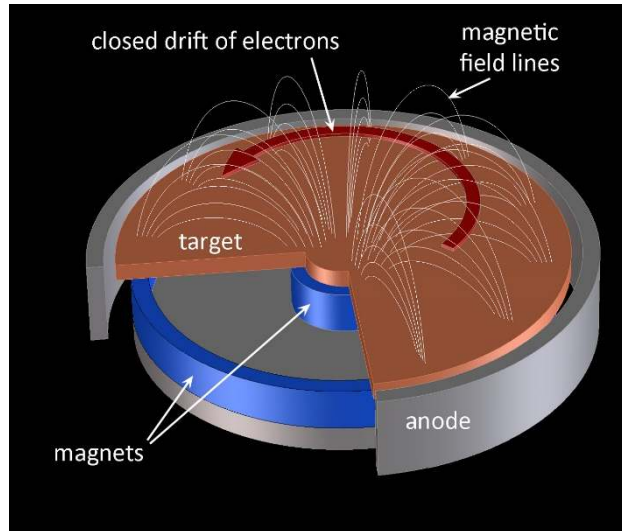


FIG. 3. Schematic of a planar magnetron with a disk target (Reprinted Fig. 1 from ref.<sup>14</sup>, with permission from Elsevier).

Magnetic field lines are approximate equipotential lines due to the high mobility of electrons along the field lines. As a result, the electric field is essentially perpendicular to the magnetic field lines. (The situation is more complicated in the presence of collective effects – discussed later.) If we average over the periodic motion of gyration and the oscillatory motion of electrons along the field lines, we arrive at an average electron drift motion in the  $\mathbf{E} \times \mathbf{B}$  direction. This drift can be understood keeping in mind

that the gyration is not described by a circle but by a path characterized by electron acceleration and deceleration during each gyration. The clever design of a magnetron makes use of the drift by closing the drift path: electrons, on average, drift back to the point where they came from, as indicated by the large curved arrow in Fig. 3. The velocity of this drift is<sup>15</sup>

$$\mathbf{v}_{\text{ExB}} = \frac{\mathbf{E} \times \mathbf{B}}{B^2} . \quad (10)$$

The absolute value,  $v_{\text{ExB}} = E / B$ , is typically in the range between  $10^5$  and  $10^6$  m/s, see ref.<sup>16,17</sup>.

This is simplified in several ways. First, the actual motion of electrons is also subject to other drifts, such as the diamagnetic drift due to the electron pressure gradient (fluid model), or, if expressed in the guiding center model of individual electrons, the magnetic gradient drift and the curvature drift.<sup>18</sup> Difficulties arise primarily from the fact that the local electric field is determined by the plasma and plasma boundaries, which should be taken into account in a self-consistent manner. In a first approximation, however, one can take the magnetic field given by the permanent magnets of the magnetron, and assume a reasonable electric field distribution, and then solve the equation of motion

$$m_e \frac{d\mathbf{v}_e}{dt} = -e(\mathbf{E} + \mathbf{v}_e \times \mathbf{B}) . \quad (11)$$

The solution for a rectangular target magnetron is plotted in Fig. 4, nicely showing the drift over the racetrack when averaging over gyration and back-an-forth motion.

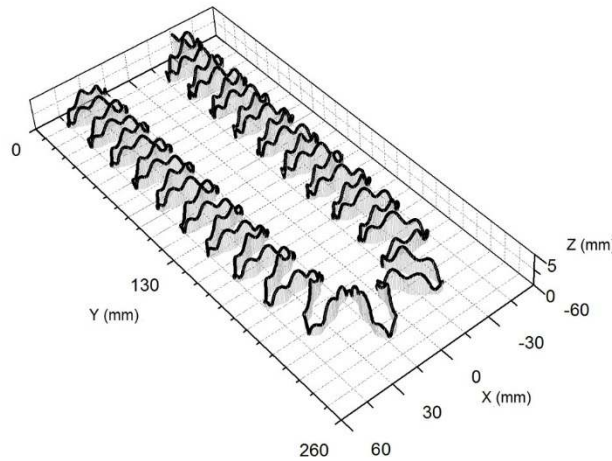


FIG. 4. 3D-view of an electron trajectory above the surface of one section of a rectangular target magnetron, calculated by solving the equation of motion in a given magnetic and electric field (Reprint of Fig. 6(a) from ref.<sup>19</sup>, with permission from IOP Publishing Ltd).

Energetic electrons colliding with process gas atoms may ionize them, producing a plasma consisting of electrons and ions. Most (positive) ions are attracted back to the (negative) target and are responsible for sputtering of the target, while sputtered atoms can travel to the substrate to form a film.<sup>20</sup> The



microstructure of a film is determined by the substrate temperature and the energy of the atoms, as illustrated by the Thornton structure zone diagram.<sup>21</sup> As we will see, in the context of R-HiPIMS, we care about the ionization of sputtered atoms *and* process gas, and how ions arrive at the substrate. Windows and Savvides<sup>22,23</sup> introduced a magnetron version designed to transport some of the magnetron plasma to the substrate by intentionally unbalancing the magnetic field. This is accomplished by using inner and outer magnets of different strengths. For example, Fig. 5 shows a magnetron whose outer magnet ring is stronger than the central magnet. Magnetic field lines connect the magnetron and the substrate. The plasma has then two purposes: to deliver ions to the target for sputtering, and also to supply ions to assist in the growth of films, affecting their microstructure (described by a generalized Thornton diagram<sup>24</sup>).

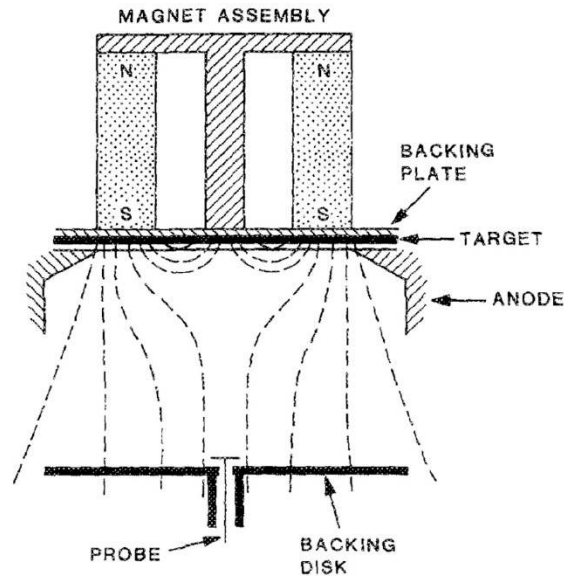


FIG. 5. Principle of an unbalanced magnetron designed to guide some plasma to the substrate, thereby providing a means to affect the microstructure of deposited films (in this figure, a probe and a backing disk for making measurements are placed in the location of the substrate; Reprint of Fig. 1 from ref.<sup>22</sup>, with permission from the American Vacuum Society).

Transport of charged particles in a magnetron is greatly affected by collisions and collective phenomena, such as spokes<sup>25,26</sup> and flares,<sup>27</sup> discussed later in more detail. Collisions and collective phenomena help that electrons escape and actually reach the anode, thereby closing the discharge circuit. Without collisions and collective phenomena the magnetron would not work. The magnetron is one of several much-investigated plasma devices that make use of crossed electric and magnetic fields. For example, Hall thrusters, used for propulsion of satellites, are closely related; their physics is discussed in a different Tutorial.<sup>28</sup>

When ions impact the target they not only cause sputtering but also release secondary electrons (Fig. 1). The corresponding yield,  $Y_{SE}$ , is defined in analogy to Eq. (1) as

$$Y_{SE} = N_e / N_i , \quad (12)$$

where  $N_e$  is the number of electrons emitted by the impact of  $N_i$  ions. Some  $Y_{SE}$  data for argon ion bombardment can be found in the work by Szapiro and Rocca.<sup>29</sup> Magnetrons typically operate with less than 1 kV of voltage, and therefore the energy of ions impacting the target is generally less than 1 keV for singly charged ions, and less than 2 keV for doubly charged. For those kinetic energies, the electron emission mechanism is primarily determined by the potential energy of the arriving ion projectiles (so-called *potential emission*) and occurs at the target surface due to resonance and Auger electron transitions.<sup>30</sup> Experimental data of the secondary emission yields for various ions satisfy the fit<sup>31</sup>

$$Y_{SE} = 0.032(0.78 E_{pot} - 2\phi) . \quad (13)$$

where  $E_{pot}$  is the potential energy of the incoming primary ion, which is in most cases the ionization energy (in eV), and  $\phi$  is the work function of the target material (in eV), i.e. the height of the potential barrier for electrons, which is approximately 4.5 eV for most metals (emission from compound surfaces is discussed later). According to Eq. (13), in order for any potential emission to occur, the condition

$$0.78 E_{pot} > 2\phi \quad (14)$$

needs to be fulfilled. In conventional magnetron sputtering, with voltages applied in direct current (dcMS) or medium-frequency pulsed (mfMS, typically 10-350 kHz), or radio frequency (rfMS, typically with 13.56 MHz), the process plasma contains noble gases, often argon for cost reasons, and the condition (14) is readily fulfilled because the ionization energy of argon is 15.76 eV. Singly charged metal ions do not fulfill condition (14).

Secondary electrons are very important to sustaining the discharge because they can directly ionize the process gas and also supply energy to other electrons, enabling them to cause ionizing collisions. Secondary electrons are an “engine” of the discharge. Thornton<sup>20</sup> considered secondary electrons not just one but *the* (only) engine of the discharge. This leads us to the Thornton paradigm, a condition for the minimum voltage required to maintain the discharge, which in its simplest form can be written as

$$V_{disch} \geq \frac{E_{i,eff}}{Y_{SE,eff}} , \quad (15)$$

where  $E_{i,eff}$  is the effective energy cost for the average ion–electron pair created, and  $Y_{SE,eff}$  is the effective secondary electron emission yield. The effective yield is notably smaller than the commonly tabulated values of the secondary emission yield  $Y_{SE}$  because emitted electrons are likely recaptured by the cathode (target) due to the curved electron trajectory in the magnetic field. The emission formula needs to include the escape probability  $p_{escape}$ , which is complementary to the recapture probability  $p_{recap}$ , i.e.  $p_{escape} = 1 - p_{recap}$ , and  $Y_{SE,eff} = p_{escape} Y_{SE}$ . The local current density of secondary electron emission relevant to the discharge is therefore

$$j_{SE} = p_{escape} Y_{SE} j_i \equiv Y_{SE,eff} j_i \quad (16)$$

where  $j_i$  is the local current density of ions arriving at the target. If they escape, secondary electrons move through the sheath adjacent to the target and thereby gain energy that corresponds to 80-90% of the applied voltage. For example, the target potential may be -400 V with respect to ground (= anode), and about 340 V of the 400 V may be dropping in the sheath, and the rest in the magnetic presheath (Fig. 6).

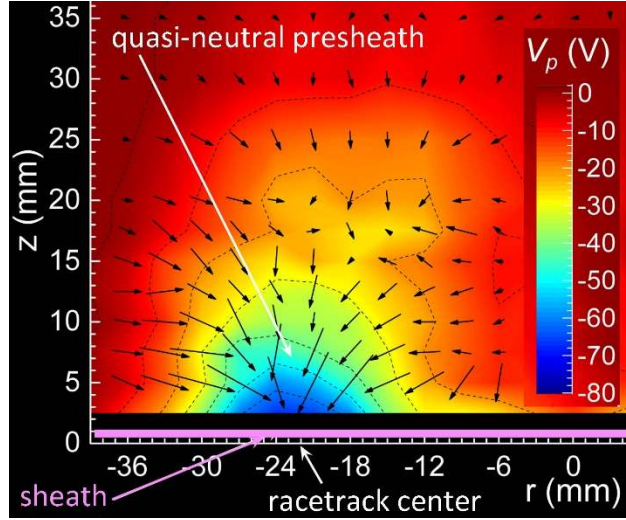


FIG. 6. Plasma potential distribution in front of a target, measured with an emissive probe for dc magnetron sputtering; the color indicates the potential, and the arrows show the electric field vectors;  $z$  is the distance from the target,  $r$  is the radial position relative to target axis of symmetry; the racetrack is at a radius of 22 mm from the target center. Please note that the sheath is very thin ( $< 1$  mm) and not measured by the probe but indicated schematically. The presheath shows the typical shape as dictated by the magnetic field lines (dashed white lines), which are approximate equipotential lines; the potential distribution shows deviations from the here-shown in regions of spokes and flares, as discussed later (image adapted from ref.<sup>32</sup>, with permission from AIP Publishing).

The difference between sheath and presheath primarily lies in the fact that the sheath is essentially void of electrons and dominated by the ion space charge, while the presheath contains quasineutral plasma. The condition of quasi-neutrality is that positive and negative charges approximately balance:

$$\sum_{\alpha} Q_{\alpha} n_{i,\alpha} - n_e - \sum_{\beta} Q_{\beta} n_{i,\beta} \approx 0, \quad (17)$$

where the indices  $\alpha$  and  $\beta$  refer to all kinds of positive and negative ions present, respectively; and charge state number and density are denoted by  $Q$  and  $n$ , respectively. When singly charged, positive ions dominate the plasma (as is often the case in magnetron sputtering) one can simplify Eq. (17) to

$$n_e \approx n_i, \quad (18)$$

which means that the densities of electrons and ions are approximately equal. However, even a small difference between electron and ion densities, the net charge density  $\rho = n_i - n_e$ , is associated with an electric field gradient as described by Gauss' law:

$$\epsilon_0 \nabla \cdot \mathbf{E} = \rho . \quad (19)$$

Since  $\mathbf{E} = -\nabla V$ , Gauss' law is often written as the Poisson equation relating the local potential  $V$  to the local space charge  $\rho$ :

$$\nabla^2 V = -\rho / \epsilon_0 , \quad (20)$$

where  $\epsilon_0 = 8.854 \times 10^{-12}$  F/m is the permittivity of free space. Such relation needs to be used, not Eq. (18), when investigating plasma instabilities and the detailed potential structure of the presheath.

Coming back to the secondary electrons that escaped from the target and gained energy in the sheath: they are able to produce about  $N_{ei}$  electron-ion pairs, where  $N_{ei} = eV_{sheath} / E_{i,eff}$ . While Thornton stressed the role of secondary electrons, the Thornton paradigm (15) is incomplete. The presheath voltage also plays an important role for electron heating and consequently for ionization of the process gas, and also of sputtered atoms in the case of HiPIMS. The presheath voltage is approximately the difference between the discharge voltage (between anode and cathode) and the sheath voltage. While this voltage is clearly much less than the voltage drop in the sheath, the number of electrons present in the presheath is much greater than the number of electrons in the sheath. Namely, only the secondary electrons gain energy in the sheath. In the presheath, in contrast, all electrons of the quasineutral presheath plasma can gain energy. This suggests comparing the heating power provided to secondary electrons via the sheath to the heating power provided to plasma electrons in the presheath.<sup>33</sup> The former can be written as the product of the secondary electron current and the sheath voltage:

$$P_{sheath} = I_{SE,eff} V_{sheath} \quad (21)$$

while the latter is the product of the presheath voltage and about ½ of the discharge current, assuming that the electrons carrying the current to the anode are produced, on average, in the presheath about half-way in the presheath, hence

$$P_{presheath} = I_{disch} V_{presheath} / 2 . \quad (22)$$

The discharge current at the target surface is composed of arriving ion current and the current of secondary electrons escaping:  $I_{disch} = I_i + I_{SE,eff}$ , and using (16) in the integral form,  $I_{SE,eff} = Y_{SE,eff} I_i$  can express the current of secondary electrons as

$$I_{SE,eff} = I_{disch} \left( 1 - 1 / (1 + Y_{SE,eff}) \right) \quad (23)$$

which leads to an expression for the ratio of sheath to presheath heating<sup>34</sup>

$$\frac{P_{sheath}}{P_{presheath}} = 2 \left( 1 - \frac{1}{1 + Y_{SE,eff}} \right) \left( \frac{V_{disch}}{V_{presheath}} - 1 \right) \quad (24)$$

For example, assuming that  $Y_{SE,eff} \approx 0.05$ ,  $V_{disch} \approx 400$  V, and  $V_{presheath} \approx 60$  V we find a ratio of 0.54, i.e. heating by secondary electrons and heating in the presheath are approximately equal in this example.

None of them can be neglected. The Thornton paradigm (15), a condition for the minimum voltage to sustain the magnetron discharge, is incomplete since it does not account for electron heating in the presheath. A generalized Thornton equation, accounting for both secondary electrons and presheath heating, has recently been derived by Brenning *et al.*<sup>35</sup>

Until now we have implicitly assumed that the plasma is evenly distributed along the racetrack. This is, under most conditions, not the case. One observes that the ionization processes in the presheath are concentrated in moving regions of enhanced ionization, which have been called localized ionization zones or “spokes” in analogy to “spokes” in Hall thrusters, a term originally introduced by Janes and Lowder.<sup>36</sup> For magnetrons, localized ionization zones or spokes have been first noted for HiPIMS<sup>37,38,39,40</sup> and later also for dcMS.<sup>25,41,42</sup> When observing spokes we see light emitted from the regions of greatest electron impact excitation of atoms and ions. The energy-dependent cross sections for excitation and ionization have similar shape and lie in approximately the same energy range (Fig. 7), therefore it is reasonable to identify the region of greatest light emission with the region of most intense ionization.

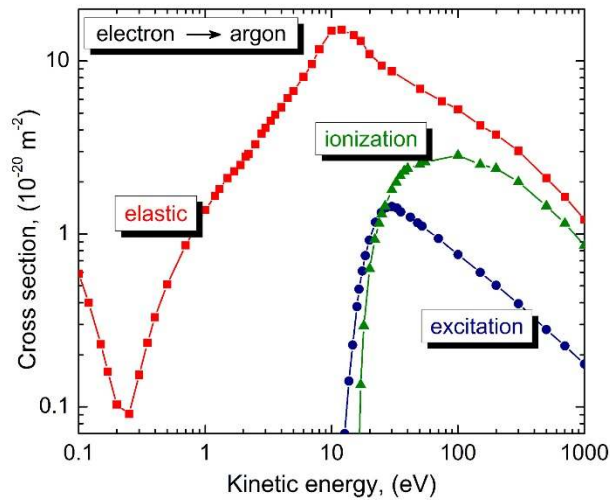


FIG. 7. Energy-dependent cross sections for electron-argon interactions (Reprint of Fig. 9 from ref.<sup>38</sup>, showing data from the collection of A.V. Phelps,<sup>43</sup> with permission of AIP Publishing).

The change in ion density, and analogously electron density, can be written by a rate equation of the form

$$\frac{dn_i}{dt} = K_\alpha n_{Ar} n_e - K_\beta n_e^2 n_i - \nabla \cdot (n_i \mathbf{v}_i) \quad (25)$$

where  $K_\alpha$  and  $K_\beta$  are the ionization and recombination rate coefficients, and the last term describes the plasma flow. The ionization and recombination rate coefficients are<sup>44,45</sup>

$$K_\alpha = \int f_e(E_e) E_e^{1/2} \sigma_{e-Ar}(E_e) dE_e \quad (26)$$

$$K_\beta \approx \frac{4}{9} \left( \frac{2\pi}{m_e} \right)^{1/2} \left( \frac{e^2}{4\pi\epsilon_0} \right)^5 (kT_e)^{-9/2} \quad (27)$$

where  $E_e$  is the electron energy,  $f_e(E_e)$  is the electron energy distribution function, and  $\sigma_{e-Ar}$  is the electron-atom ionization cross section as shown in Fig. 6. From these equations, and taking into account that the neutral gas density in dcMS is approximately the same everywhere, the determining factor in excitation and ionization is the electron energy. The fact that we find spokes suggests that energetic electrons responsible for ionization are not evenly distributed but locally energized in a manner associated with the potential structure of drifting spokes.<sup>34</sup> This in turn suggest to focus investigations on the potential structure of spokes.

The number of spokes mainly depends on the gas pressure and power<sup>42</sup> (and in the case of HiPIMS also on the target material<sup>38</sup>). For dcMS one can find conditions where exactly one spoke exists in a research-sized magnetron. This provides an opportunity to readily study spoke features such as the spoke drift velocity and the structure of the potential distribution.<sup>32</sup> Fig. 8 shows that the bright region of plasma is associated with a high potential, while the less bright region is at lower potential. The potential distribution is shown at several distances ( $z$ ) from target indicating that most of the structuring occurs close to the target ( $z = 10$  mm or less). This can even better be seen in a presentation looking from the side (Fig. 9).

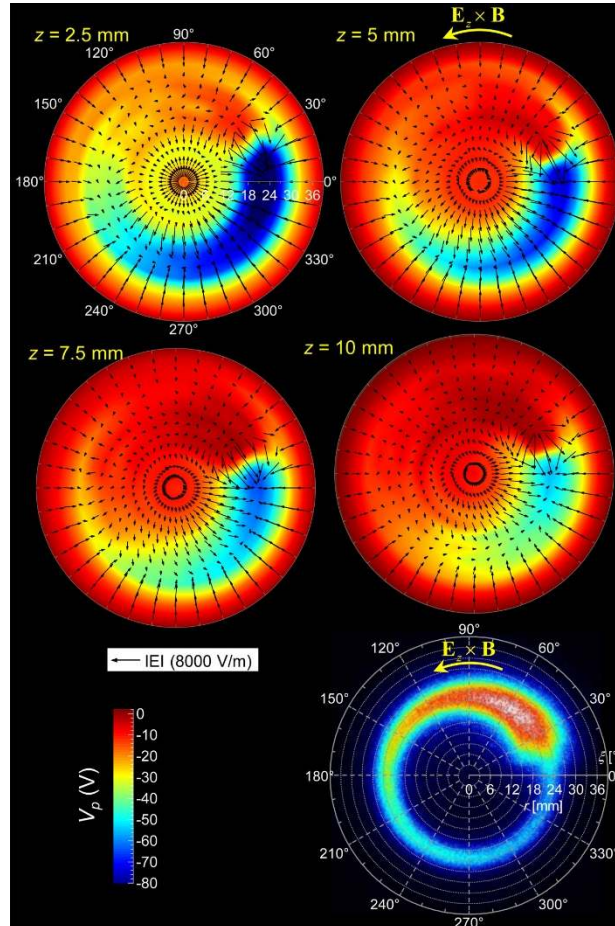


FIG. 8. Top four subfigures: Plasma potential of a 7.5 cm (3") magnetron operating in dcMS mode, measured with an emissive probe at different distances  $z$  from the target surface; subfigure in lower right corner: corresponding light intensity, recorded with a fast-shutter, intensified CCD-camera, shows the emitted light intensity from one spoke in false color (100 mA, Nb target, in 0.27 Pa argon; from Fig. 5 of ref.<sup>32</sup>, with permission from AIP Publishing).

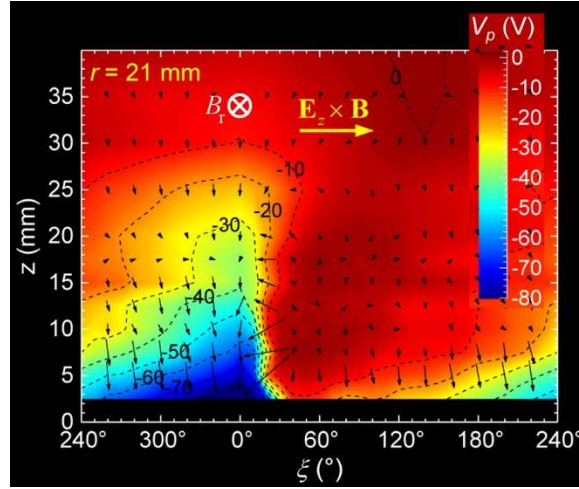


FIG. 9. Side view of the spatial distribution of the plasma potential (relative to ground) as measured over the racetrack, at a radius of 21 mm from the target center; same conditions as in Fig. 8. One can clearly discern the sharp potential jump associated with the edge of the spoke (from Fig. 6 of ref.<sup>32</sup>, with permission from AIP Publishing).

A well-defined space charge double layer separates the regions of low and high potential. Drifting electrons pass the double layer coming from low and going to high potential, thereby gaining the energy that allows them to enhance ionization and excitation after the potential jump. Before the jump, the potential is lowest, and electrons have the smallest energy, which appears as a dark region (the terms “before” and “after” should be understood with reference to the motion of drifting electrons). While electron heating and ionization according to the Thornton paradigm is well established, heating of electrons in the presheath and in spokes is still subject to research and not yet widely accepted.

Besides local variation of the potential and electron energy, the discharge has an effect on the gas density, which is reduced by a combination of several effects jointly known as gas rarefaction.<sup>46</sup> For one, the volume of the sputtering chamber acts like a large reservoir, which keeps the total pressure approximately constant. According to the ideal gas law

$$p = n k T \quad (28)$$

the gas pressure  $p$  is the product of the gas density  $n = N/V$  and gas temperature  $T$  (here,  $k$  is the Boltzmann constant, and  $N/V$  is the number of gas atoms in the volume  $V$ ). Hence we have  $n = p/kT \approx \text{const} / kT$  implying that any rise in the local gas temperature will cause an inversely

proportional reduction in the local gas density. Heating of the gas by the hot target surface and by the discharge itself will lead to a reduction of gas density. Gas density reduction is further amplified by the “sputter wind”,<sup>47</sup> the flow of energetic particles from the target, i.e. by sputtered atoms and reflected ions (which are neutralized upon contact with the target). While gas rarefaction can have a very significant influence on discharge, it is not the primary driver for spokes. This is evident from the fact that spokes are observed even with extremely weak discharges with power as low as 3 Watt.<sup>25</sup>

#### IV. REACTIVE MAGNETRON SPUTTERING

The majority of films and coatings needed for applications are compound films (the terms “film” and “coating” are used here interchangeably; the conventional difference is that films are thin ( $< 1 \mu\text{m}$ ) and coatings are thick ( $> 1 \mu\text{m}$ )). Compound films offer a much wider range of electrical, optical, mechanical, chemical and derived properties than just metal films. The range of properties can be further broadened by depositing multilayers and nanocomposites. In this section we consider the consequences when a reactive gas is added to the process gas.

Besides reacting with newly-deposited atoms on the substrate surface, reactive gas atoms also react with the surface atoms of the target, thereby greatly changing the sputtering yield and the yield of secondary electrons, which in turn affects practically all discharge parameters. One speaks of “poisoning” the target when a compound layer forms on the target.

The formation of the compound layer can be related to several mechanisms, which are associated with the reactivity of the target material and the different types and energies of particles arriving at the target surface.<sup>48,49</sup> First, low energy molecular or atomic (neutral) species of the reactive gas are adsorbed and chemically bonded (chemisorbed<sup>50</sup>), leading to a thin compound layer on the target surface. This is especially important for target materials having a high chemical affinity to the reactive gas, such as aluminum to oxygen. Second, ions arriving at the target are energetic due to acceleration in the presheath and sheath; they can lead to recoil-implantation of chemisorbed atoms. Many of the gas ions are noble gases, yet they can contribute to the formation of a relatively thick compound layer by this mechanism.<sup>51</sup> Next, reactive gas ions can be directly implanted.<sup>49,52</sup> At the high kinetic energy, which corresponds up to the discharge voltage times the ion charge, reactive gas ions can react with the target metal when coming to rest below the surface. Finally, since the target surface is hot, diffusion of reactive gas species to greater depth can contribute to the formation of a compound layer much thicker than the range of implanted ions, something well studied in the context of ion nitriding.<sup>53</sup> However, the target as a whole is usually water-cooled, preventing diffusion to be important for most of the target body. Real-time in situ target analysis using the  $^{14}\text{N}(d,\alpha)^{12}\text{C}$  nuclear reaction did not give evidence for the diffusion in the titanium-nitrogen case.<sup>48</sup> Though in practically all cases, the reactive gas forms a compound layer that is much thicker than a monolayer. The thickness of the compound layer can be significantly less in the racetrack area because we have the competing processes of compound formation (by chemisorption and ion implantation) and removal (by sputtering).<sup>54</sup>

Since the chemical bond strengths of compounds are generally much stronger than the bonds of metal atoms, the sputter yield is always reduced when poisoning occurs. A lower sputter yield (a ratio, a dimensionless number) leads to a lower deposition rate (often expressed in nm/min). This is of great concern in terms of the economics of the deposition process because yield and rate reductions can be



very significant. Therefore, it is desirable to add just enough reactive gas such as to obtain a compound film on the substrate but be able to sputter away the thin compound layer on the target, thereby maintaining a metal surface on the target. It is very difficult to remain in the non-poisoned (metal) target mode due to system feedbacks. This is best explained looking at the total pressure – reactive gas flow relation (Fig. 10 top). When the reactive gas (e.g. oxygen) flow is still very low, ions arriving at the target sputter away the few surface atoms that have reacted with oxygen, and the surface stays metallic. Metal atoms arriving at the substrate can react but the film may be sub-stoichiometric since the process is still starved of oxygen. It is important to understand that such system has two pumps for the reactive gas: one is the physical pump of the vacuum system, such as a turbomolecular pump, and the other “pump” is the growing film because it removes reactive gas from the volume. Now, increasing the reactive gas flow will lead to more compound formation on the target. Eventually, the removal of compound material from the target cannot keep up with the formation. That causes the flux of metal from the target to be greatly diminished, which turns down the second “pump”, the uptake of reactive gas by the growing film. As a result, the oxygen partial pressure and the total pressure increase abruptly until flow and pumping again balance, and one sees again a proportional flow-pressure relation. Reversing the flow change direction brings us back to the metal mode, however, only after the compound layer on the target is removed. As a result one sees a hysteresis (i.e. the curves depend on the direction of change). When hystereses such as those in Fig. 10 are produced, a certain rate of change is applied or a certain time is used to let the system find its working point. When a rate is applied, the specifics of a hysteresis will depend on the rate of change.<sup>55</sup>

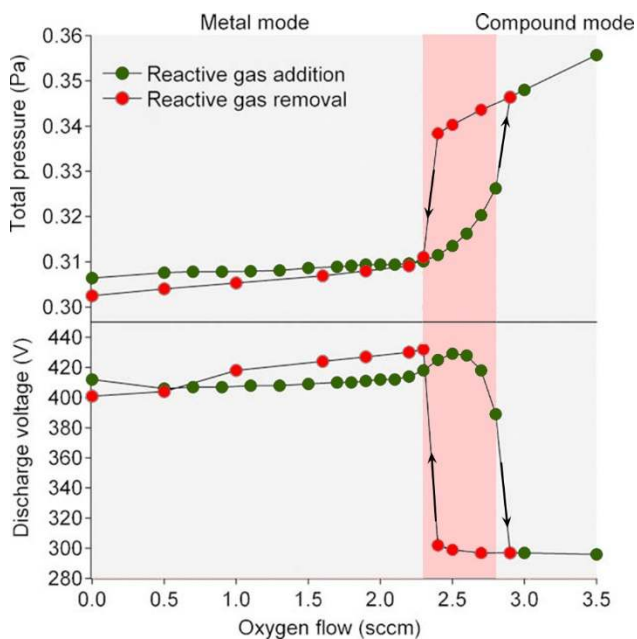


FIG. 10. DC magnetron sputtering of an aluminum target in an Ar/O<sub>2</sub> gas mixture with increasing (green points) and decreasing oxygen flow (red points); Top: total pressure; Bottom: discharge voltage under constant current conditions (Reprint of Fig. 5.16 from ref.<sup>56</sup>, with permission from Elsevier).

All kinds of hystereses can be found in reactive sputtering, for example, a deposition rate-flow hysteresis can be plotted, or a voltage-flow hysteresis (Fig. 10 bottom). The latter is strongly related to another

yield effect, the yield of secondary electrons,  $Y_{SE}$ . Since the secondary electron emission changes, one “driver” or “engine” of the discharge changes too. This affects the current-voltage relation, the plasma density and composition, gas rarefaction, and other parameters. Depla and coworkers<sup>57</sup> studied the change of the effective secondary emission coefficient for a number of target materials in nitrogen- and oxygen-containing process gases (Figs. 11 and 12, respectively). Contrary to statements sometimes found in the literature, poisoning of the target does not always lead to an increase in the secondary electron yield. In the case of oxygen reacting with aluminum, we see indeed a significant increase, the higher current of secondary electrons leads to greater ionization, which increases the current. In a constant current or constant power setting, the voltage would be reduced to maintain the set current or power, which is shown in Fig. 10 (bottom).

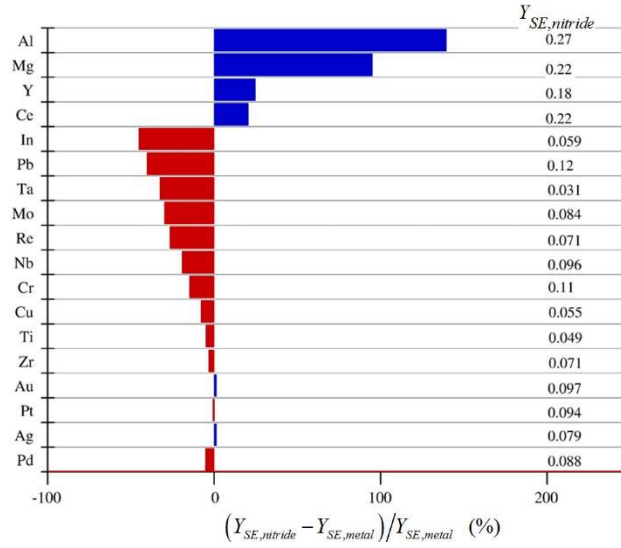


FIG. 11. Relative change of the effective emission coefficient by nitride compound formation on the target surface.  $Y_{SE,metal}$  and  $Y_{SE,nitride}$  designate the secondary electron yield of the metal and of the nitride, respectively (Reprint of Fig. 9 from ref.<sup>57</sup>, with permission from Elsevier).

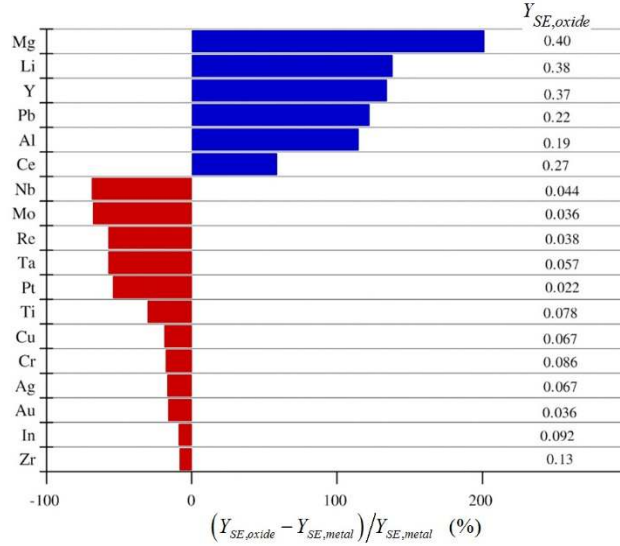


FIG. 12. Relative change of the effective emission coefficient by oxide compound formation on the target surface.  $Y_{SE,metal}$  and  $Y_{SE,oxide}$  designate the secondary electron yield of the metal and of the oxide, respectively (Reprint of Fig. 10 from ref.<sup>57</sup>, with permission from Elsevier).

For target-gas combinations that show a strong change of secondary electron emission yield, the target voltage change can be used to control the working point by establishing a feedback to the control of the reactive gas flow supply. Ideally one wants to operate in the metal mode on the target side, while producing a stoichiometric compound film on the substrate. This requires operation in the transition region between metal mode and poisoned mode. This is difficult as the reactive partial pressure must be precisely controlled and quickly adjusted to avoid a sudden switch to the poisoned mode. Much effort has been spent to develop fast feedback systems for reactive deposition, see, for example the review by Sproul et al.<sup>58</sup>

Considering steady-state conditions, the fraction  $\Theta_1$  of target coverage by a compound film (fraction of poisoning) and corresponding fraction  $\Theta_2$  on the opposing collecting surface (substrate and neighboring walls) has been modeled using a system of steady-state balance equations by Berg and coworkers.<sup>59</sup> What is now generally known as the “Berg model,” illustrated by Fig. 13, has become the basis for many later modeling approaches to determine particle flux ratios, to describe the formation of various hystereses,<sup>55</sup> and to predict compound stoichiometry.<sup>60,61</sup> The Berg model has also been the inspiration to modeling of ion and atom fluxes in non-reactive HiPIMS by Christie<sup>62</sup> and in R-HiPIMS by Kozák and Vlček,<sup>63</sup> topics to be discussed later.

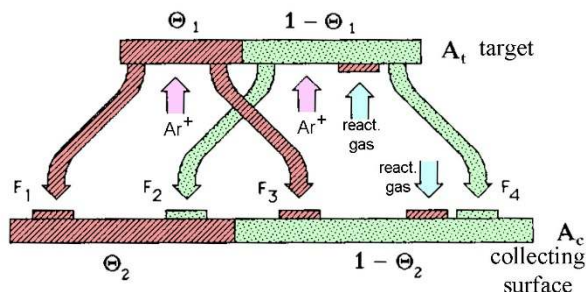


FIG. 13. Schematic illustration of the system of steady-state balance equation introducing the fraction of compound film  $\Theta_1$  and  $\Theta_2$  on the target and the opposing collecting surface, respectively (Reprinted Fig. 2 from ref.<sup>59</sup>, with permission from the American Vacuum Society).

The deposition of insulating compound films (such as  $\text{Al}_2\text{O}_3$ ) represents an additional challenge. Not only one has to deal with target poisoning but also with the “disappearing anode” problem. Namely, in the course of the deposition process, the anode gets coated with an insulating film: it “disappears” electrically. The common solution to this problem is *dual magnetron sputtering*, using two magnetrons, and use their targets alternately as anode and cathode.<sup>64,65</sup> When a target is the anode (positive polarity) it will be coated by a very thin insulating film, which is sputtered away when that target serves as the cathode (negative polarity). The change of polarity is fast, usually in the range of several 10 kHz with sine-wave current-voltage shapes. Power supplies for dual magnetron sputtering are commercially available.

An alternative approach to the disappearing anode problem is using hidden (shielded) anodes, or more than two anodes, where one is the real anode at a given time, and the other is at negative polarity to be sputter-cleaned. This is known as dual anode sputtering.<sup>66</sup> Contamination of the growing film by sputtering one of the anodes is minimal since one sputters the just-formed film, and/or one could use the same metal at the target, and one can use clever methods of controlling the amount of anode sputtering.<sup>67</sup>

Some reactive gases, such as oxygen and fluorine, tend to readily form negative ions. This is of concern since the same electric field that accelerates positive ions *to* the target accelerates negative ions *away* from the target.<sup>68</sup> Energetic negative ions can bombard the growing film and cause sputtering and ion damage.<sup>69,70</sup> Ion damage refers to defects in the crystalline structure that have a detrimental influence on properties such as a desired high visible transmittance and low electrical resistance expected in transparent conducting oxides. Most damaging are negative ions formed at the target surface since they travel through the entire sheath and presheath and thereby gain most energy. Therefore, avoiding the poisoned target state is important not only from a deposition rate point of view also to avoid ion damage and non-uniformities in growing films.

## V. PULSED REACTIVE MAGNETRON SPUTTERING

So far we have discussed that poisoning of the target reduces the deposition rate and (undesired) bombardment of the film by high energy particles. Yet another issue is arcing on the target,<sup>71</sup> which occurs with much greater propensity when reactive gas is present. Arcing means that the magnetron switches to an entirely different mode of an electrical discharge, the cathodic arc discharge,<sup>72</sup> characterized by a sudden increase in current, decrease in target voltage (from the typical few 100 V to less than 40 V), the appearance of small cathode spots on the target, and the ejection of microscopic target debris, also known as droplets or macroparticles. When incorporated in a film or coating, defects can be even greater than the original macroparticle due to nodule growth.<sup>73</sup> The macroparticle can be removed (e.g. by buffing) and yet the remaining defect can be the location of enhanced corrosion,<sup>74</sup> wear,<sup>75</sup> and other undesirable effects.<sup>76</sup> Therefore, in practically all cases, macroparticles are detrimental and one wants to avoid arcing.

Among the measures to suppress arcing is to operate the magnetron in pulsed mode, which comes in two versions. One is the already-mentioned dual magnetron mode. The other was introduced in the early 1990s<sup>77</sup> and is known as the “pulsed dc” mode, where the applied voltage is switched on and off at a medium frequency in the range 10 – 350 kHz. The upper limit has no specific physics reason but is set by the upper frequency of the widely used power supply Pinnacle® Plus by Advanced Energy. Pulsed sputtering is used to reduce the propensity to arcing because the arc onset is usually delayed relative to the application of a voltage. Charge accumulation on insulating or poorly conducting films is thought to be compensated by the opposite charge when the applied voltage is switched off or reversed for a brief moment. Less charge-up implies less electric surface field, while a high electric field is the precondition for the ignition of an arc spot.<sup>72</sup> This is nicely illustrated in a study of the arcing rate as a function of pulse repetition rate (and thereby pulse length  $\tau_{on} = 1/f - \tau_{rev}$ ) and duration of polarity reversal  $\tau_{rev}$  (Fig. 14). It was found that arcing is greatly reduced if the frequency is higher than a threshold. In the example of sputtering Al in an Ar/O<sub>2</sub> mixture, the threshold was about 40 kHz and is reduced down to 10 kHz when polarity reversal was employed (Fig. 14).

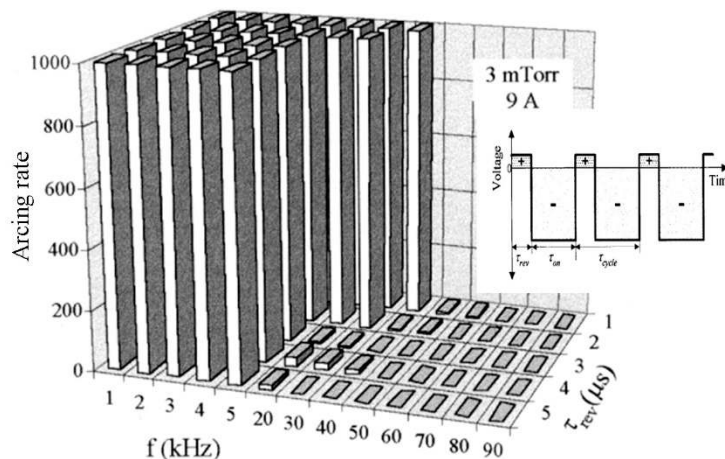


Fig. 14. Arcing rate as a function of pulse repetition rate and duration of polarity reversal for the reactive deposition of alumina, here using 30 sccm O<sub>2</sub> and 10 sccm Ar, current 9 A, with a racetrack length of about 50 cm (Reprint of Fig. 3 from ref.<sup>78</sup>, with permission from the Society of Vacuum Coaters).

When the voltage is applied in pulses, all parameters become dynamic, i.e. they change in time. Looking at the sheath and presheath, as illustrated in Fig. 6, one needs to realize that they are established in the pulse-on time and collapse in the off time, which is shown, in a simplified manner, in Fig. 15. Due to the collapse of the sheath, electrons from the plasma can reach the target and neutralize any positive charge should it be there. Polarity reversal promotes this process but is not needed to accomplish this.

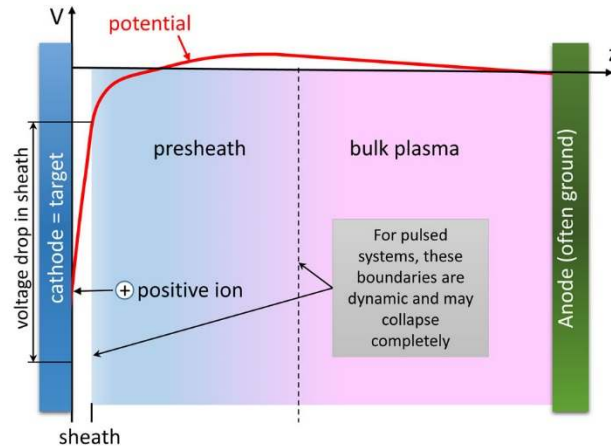


Fig. 15 Simplified sheath-presheath potential distribution, not to scale, over the racetrack, indicating that the sheath has the highest voltage drop (highest electric field) which will collapse in the pulse off time.

In the section on reactive magnetron sputtering, two system pumps were introduced: the physical pump and the coating that pumps (getters/chemisorbs/incorporates) reactive gas. In the case of pulsed sputtering, the second (coating) pump is pulsed to. Additionally, the degree of poisoning may see periodic changes, too. However, the relatively low power densities and short pulses used in pulsed-dc magnetron sputtering hardly lead to variations: the pulsing is too fast. This point should be revisited when considering R-HiPIMS, where pauses between pulses are much longer.

## VI. HIGH POWER IMPULSE MAGNETRON SPUTTERING (HiPIMS)

### A. The magnetron as a plasma source

Having good adhesion and the right film properties via a suitable, controllable, and reproducible interface and microstructure is important for all applications. The number of process parameters for sputtering is limited and includes primarily substrate temperature and gas pressure.<sup>21</sup> While it is known that ion assistance to film growth can greatly alter the microstructure and associated film properties, sputtered atoms are generally neutral (as opposed to ionized) and therefore cannot be influenced by electric and magnetic fields. A first step to utilizing the magnetron plasma for film growth assistance was made by unbalancing the magnetron<sup>22</sup> as mentioned before. The ions in this approach were ions of the processing gas, usually argon, and of the reactive gas, if present,<sup>79</sup> but not ions of the target material.

High power impulse magnetron sputtering (HiPIMS) was conceived to also produce *ions of film-forming target material*. When film-forming ions are available, the substrate-film interface and the film interface microstructure can be more efficiently influenced by substrate biasing, and magnetic fields can be used to better transport fluxes to the substrate. Ionization of the target atoms is accomplished by applying the discharge power in pulses such that the current is allowed to rise much above the average, often about 2 orders of magnitude above what the magnetron manufacturer specifies for the dcMS mode of operation.

Some basic concepts of HiPIMS can be traced back to the 1970s (e.g. self-sputtering<sup>80</sup>) but the field took off only after a seminal paper by Kouznetsov and co-workers<sup>81</sup> who used a conventional planar magnetron to demonstrate a high degree of ionization of the target material (copper in this case) by supplying very high current pulses (Fig. 16).

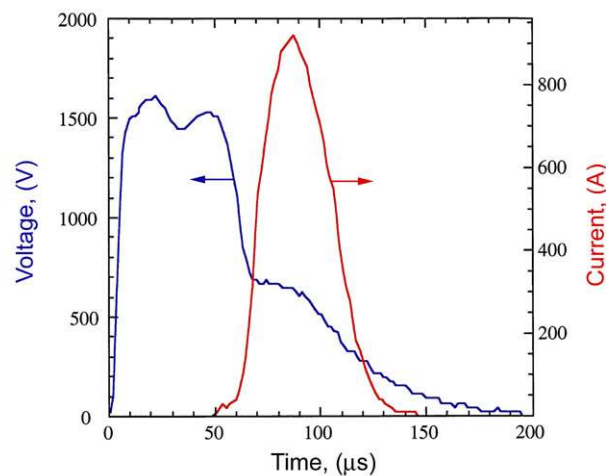


FIG. 16. Current and voltage curves for HiPIMS using a 6" (15 cm diameter) copper target. Note the high peak power, the product of voltage and current, when the current peaks. This discharge is not an arc since the voltage at the high peak current is about 600 V, a typical magnetron value (Reprint of Fig. 1 from ref.<sup>81</sup>, with permission from Elsevier).

The high peak power, which can reach and exceed 1 MW in larger systems, implies that the duty cycle of pulsing should be low to allow the target to cool. Too high average power can destroy the magnetron by demagnetizing the permanent magnets and/or melting of the target and other components. Very high pulse power is sometimes called impulse power, hence the name high power impulse magnetron sputtering (HiPIMS). However, HiPIMS is also known under other names, such as High Power Pulsed Magnetron Sputtering (HPPMS). In recent years, most workers in the field use the acronym HiPIMS or HiPIMS.

During the high power phase, the density of the plasma increases significantly, of the order  $10^{20} \text{ m}^{-3}$ , and locally (in spokes) even to higher values. Atoms traveling through such dense plasma can have a short mean free path for ionization, resulting in ionization of sputtered atoms, which then in turn participate in the sputtering process (self-sputtering).

## B. Self-sputtering and gas recycling

When using a constant pulsed voltage supply, the return of ions leads to an increase in current, which can lead to a runaway situation. Considering for a moment high yield materials such as copper one can find a very distinct jump, a runaway of the discharge to a new, much higher level of current and power (Fig. 17).

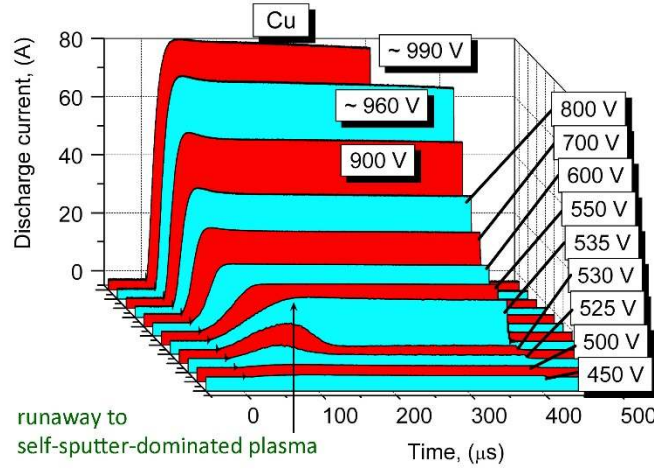


FIG. 17. 400  $\mu$ s of (almost) constant voltage pulses applied to a 5 cm (2") magnetron with a copper target, leading to a distinct jump of power when the voltage reaches 535 V (Reprint of Fig. 1 from ref.<sup>82</sup>, with permission from AIP Publishing).

Visually, the discharge changes color and suddenly becomes much brighter when self-sputtering kicks in. If we designate with  $\alpha$  the likelihood that a sputtered atoms becomes ionized, and with  $\beta$  the probability that the newly formed ion returns to the target, the jump to higher power occurs when

$$\Pi = \alpha\beta Y_{ss} > 1 . \quad (29)$$

The more atoms are sputtered, the more are available for ionization, and the more can return and cause further sputtering, as illustrated by Fig. 17. This and the following figures are simplified schematics for a set of rate equations needed to model the evolution of fluxes of the different types of particles involved.



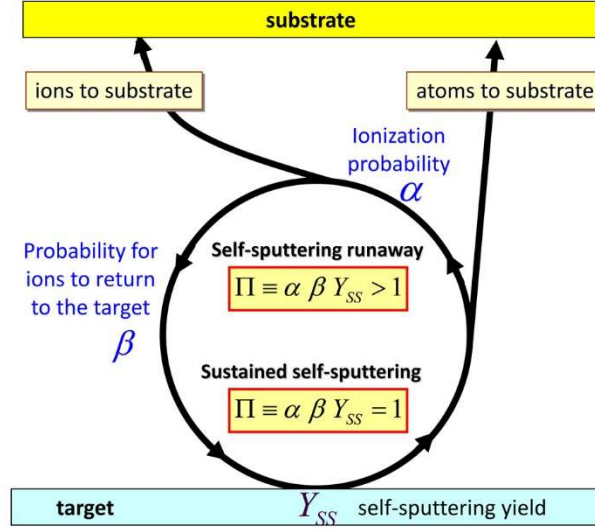


Fig. 18. Ionization of sputtered atoms provides a pathway for ions to return and sputter the target (self-sputtering). For high-yield targets like copper, self-sputtering can run away until runaway processes are balanced by loss fluxes to the substrate: the system can reach sustained self-sputtering (Reprint of Fig. 5 from ref.<sup>14</sup>, with permission from Elsevier).

Since  $\alpha < 1$  and  $\beta < 1$ , Eq.(29) can only be fulfilled if  $Y_{ss} > 1$ , which is the case for some high yield materials such as Cu, Ag, Bi, Zn, provided the ion energy is at least several 100 eV.

The relation (29) is not fulfilled for many other target materials, yet one can find a distinct runaway at sufficiently high applied voltage for practically all conducting targets.<sup>83</sup> (As a side note: due the impedance changes within each pulse, one speaks of current-voltage-time characteristics,<sup>83</sup> as opposed to the current-voltage characteristics for conventional stationary discharges.<sup>45</sup>) The solution to this initially puzzling observation is considering the fluxes of *all* gas atoms and ions, not only the fluxes of sputtered atoms. For non-reactive HiPIMS, considered in this section, one needs to account for the fluxes of noble gas, argon in most cases. Argon ions, arriving at the target with several 100 eV, are implanted below the surface, where they come to rest but do not bond (Fig. 1). The fate of implanted ions depends on their chemical nature: condensable (film-forming) ions will become part of the solid, while noble gas atoms may aggregate to form clusters or nanobubbles, and ultimately diffuse to the target surface. They outgas with characteristic energy  $E_{gas} \approx 3kT_{surf}/2$  corresponding to the temperature of the target surface,  $T_{surf}$ . Therefore, Fig. 18 is a simplified approximation neglecting gas outgassing, ionization and possibly repeated use of gas atoms. Fig. 19 shows a more complete treatment including the gas fluxes.

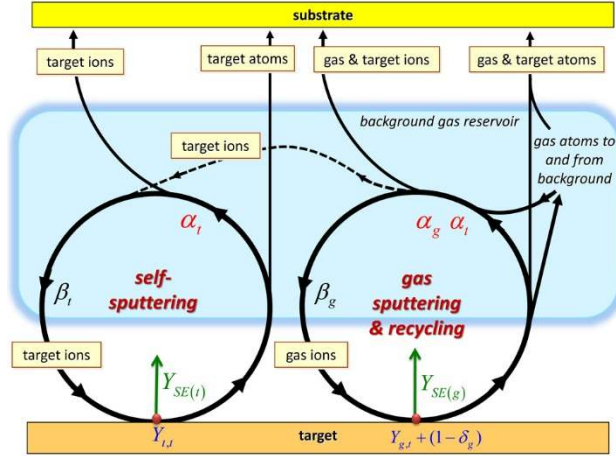


FIG. 19. Illustration of fluxes including self-sputtering, sputtering by gas, and repeated use (“recycling”) of gas atoms. Figures like that illustrate a system of nonlinear rate equations (Reprint of Fig. 1 from ref.<sup>84</sup>, with permission of the IOP Publishing Ltd).

Even in extreme cases of very low sputter yield, such as with a graphite target, one can find a very sudden onset of runaway, as shown in Fig. 20. The current can reach high values that cannot be explained by self-sputtering and also not by a supply of ions from the background gas. This suggests that gas (argon) is not merely used but actually trapped in a repetitive cycle as indicated on the right hand side of Fig. 18.

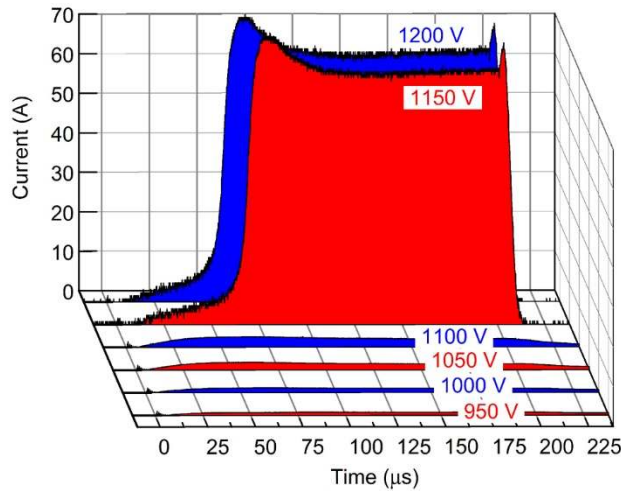


FIG. 20. Runaway to a high current level based on argon gas atoms and ions trapped in a recycling circle as shown in Fig. 19; the target was graphite. The indicated voltage is applied to the target, and the pulses are terminated at 200  $\mu$ s (Reprint of Fig. 2 from ref.<sup>84</sup>, with permission of the IOP Publishing Ltd).

Figs. 18 and 20 illustrate that all targets, regardless of their self-sputter yield, can run away to high power. This can be used to distinguish HiPIMS from conventional sputtering. In conventional sputtering, the combined effect of self-sputtering and gas recycling can be neglected. In HiPIMS, the

discharge current is dominated by the combined effect of self-sputtering and gas recycling. Since the rate equations for self-sputtering and gas recycling are nonlinear, as illustrated by feedback loops such as shown in Fig. 19, the transition from conventional sputtering to HiPIMS is most often rapid and the current is at distinctly different levels. The relative contribution to the discharge current from self-sputtering versus gas recycling strongly depends on the self-sputter yield. For most targets, having intermediate self-sputter yields, both self-sputtering and gas recycling are important.

The transition from conventional sputtering to HiPIMS is sometimes erratic or even slowly oscillating when taking the effect of gas rarefaction into account.<sup>14</sup> The role of gas rarefaction to runaway can also be seen in the example of Nb, a target material of moderate sputter yield. At the beginning of a HiPIMS experiment, the target is at room temperature and the gas density is given by the preset pressure. On a time scale from seconds to minutes, the target surface gets hot and the near-target gas density is reduced according to the ideal gas law (28), delaying or even preventing runaway conditions (Fig. 21).

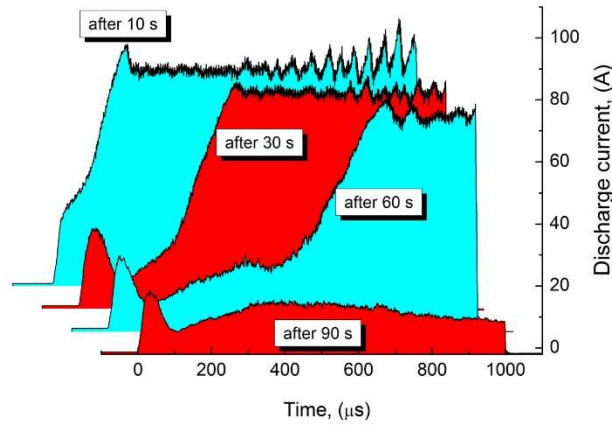


FIG. 21: Influence of rarefaction on runaway of the discharge current to a high level (Nb target, 5 cm diameter, applied voltage 520 V). The parameter is the time from the beginning of the pulsing experiment, affecting target temperature and near-target gas density (Reprint of Fig. 7 from ref.<sup>14</sup>, with permission from Elsevier).

### C. Ionization in a global ionization region versus in localized ionization zones (spokes)

To model the transition to HiPIMS and the relative role of the various fluxes and densities of species, a time-dependent plasma-chemical model can be selected which is based on sets of rate equations applied to specific regions of the discharge. This conceptual approach, originally developed for a pulsed plasma-chemical reactor,<sup>85</sup> is generally simpler than other simulation methods such as particle-in-cell (PIC) or fluid models and requires less computational resources. In the case of a magnetron, one selects three regions: the sheath, the ionization region, and the bulk plasma between the ionization region and the anode (Fig. 22). The focus of calculations is on the ionization region using sheath and bulk plasma as boundaries. The processes inside the ionization region are time-dependent but volume-averaged, i.e. processes associated with spokes and flares are smeared out. This is one of the fundamental limitations of the approach, which still is surprisingly useful in describing and predicting the overall discharge

behavior.<sup>86,87</sup> Since this Tutorial is about R-HiPIMS, we shall return to the ionization region model in the context of R-HiPIMS.

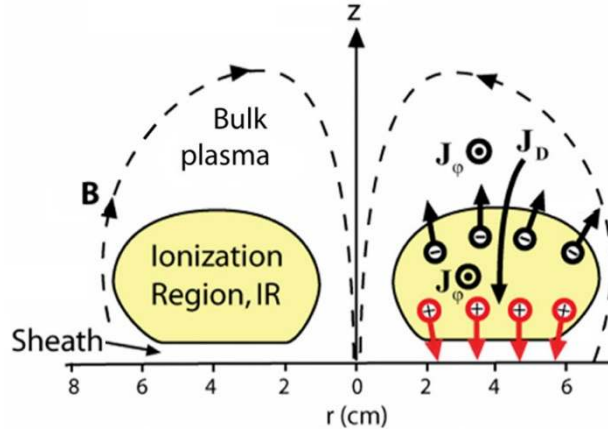


FIG. 22. Illustration of the ionization region model, where the discharge parts are segmented in sheath, ionization region, and bulk plasma. The system of rate equations is solved in a volume-averaged manner to deliver sets of consistent densities and fluxes, giving direct physical insight into the relative role of each process (Reprint of Fig. 2 from ref.<sup>88</sup>, with permission of the IOP Publishing Ltd).

While the ionization region model volume-averages over the ionization region, the ionization processes are not uniformly distributed along the racetrack. Similarly to localized ionization zones or “spokes” observed in dcMS, also HiPIMS ionization exhibits spokes in almost all cases (Fig. 23), with spokes moving in the  $\mathbf{E} \times \mathbf{B}$  direction.<sup>37,38,39,40</sup> There are exceptions, namely when the discharge operates at very high power: spokes smooth out along the racetrack.<sup>89,90</sup> It should be stressed that spokes have a phase velocity, not a group velocity, meaning that regions of most intense ionization processes move but not the plasma. Spokes in HiPIMS appear occasionally in a periodic, self-organized pattern (like Fig. 23, left) but typically change into irregular patterns of different brightness, like shown in Fig. 23, right).

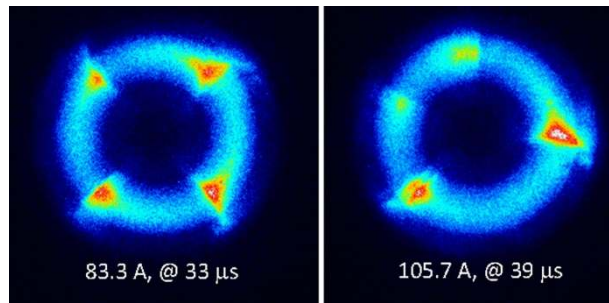


FIG. 23. High speed images, of 10 ns exposure time, of a HiPIMS plasma with a 7.5 cm (3”) Al target, sputtered in 0.27 Pa Ar; the emitted light intensity is displayed in false color and seen as a measure for the rate of excitation and ionization collisions; left: 33 μs into the pulse at 83.3 A discharge current, right: 39 μs into the pulse at 105.7 A current (Reprint of part of Fig. 1 from ref.<sup>91</sup>, with permission of AIP Publishing).

The underlying mechanism for spoke motion are still subject to research. Since the directions of spoke motion in dcMS and HiPIMS are opposite, one can assume that at least two opposing processes are at work. In dcMS, rarefaction by ionization can be neglected because there are always sufficient gas neutrals present that can be ionized by drifting, sufficiently energetic electrons. As mentioned in the section on dcMS, the potential jump at a spoke energizes electrons, thereby promoting locally enhanced excitation and ionization. The spoke edge moves into the direction where electrons come from, i.e. the  $-\mathbf{E} \times \mathbf{B}$  direction, because that is the direction newly formed ions are displaced by the local electric field, and hence the potential jump is shifted in the  $-\mathbf{E} \times \mathbf{B}$  direction. In HiPIMS, in contrast, neutral gas rarefaction by ionization is significant. The newly formed ions are “evacuated” by the local electric field, thus both neutral and ion densities are reduced at the location of most intense ionization. Drifting electrons have to drift further in the  $\mathbf{E} \times \mathbf{B}$  direction, through the “evacuated” location, to find neutrals to be ionized, and thus the region of most intense ionization is shifted in the  $\mathbf{E} \times \mathbf{B}$  direction. This qualitative picture remains to be simulated, quantified and confirmed (or disproved) by future research. Interestingly, but not surprisingly, spokes can reverse their direction of motion in the transition region between conventional pulsed-dcMS and HiPIMS.<sup>41,92</sup>

Spectroscopic imaging is used to distinguish light coming from different species in the plasma; if combined with fast cameras one can see the evolution of the species distribution.<sup>93,94</sup> Figure 24 is an example where the HiPIMS plasma was observed from the side but only in the light of the 436 nm transition of singly charged argon ions.<sup>95</sup> One can clearly see the edge of the spoke and the plasma flare that escapes from the spoke. Flares (or striations) have been seen in high speed imaging<sup>96</sup> and also recorded with a streak camera.<sup>27</sup> A torus-like plasma appears detached from the target, which is true for emission in the light of argon but not in the light of the metal. The latter is concentrated just a few mm from the target.<sup>95</sup>

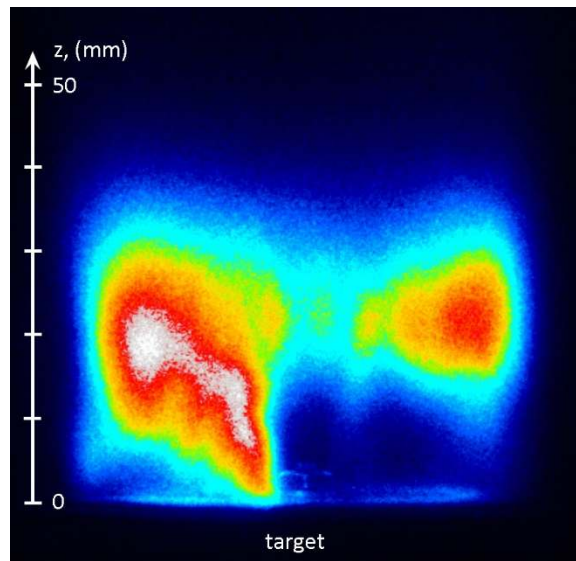


FIG. 24. Example of a 150 ns spectroscopic image showing a spoke and plasma flare in the light of Ar II 436 nm; 7.5 cm Al target sputtered in argon; the current at the time of the image was 100 A (Reprint of a part of Fig. 2 from ref.<sup>95</sup>, with permission from AIP Publishing).

#### D. Effect of the magnetic field and process gas

The strength and the degree of balance of the magnetic field are of great importance to HiPIMS, perhaps even more than for dcMS. First, magnetization of electrons affects the probability of ionization of background gas, sputtered atoms, and recycled gas, all key elements to obtain the HiPIMS-characteristic dense plasma. Second, via its effect on electrons, the magnetic field affects what fraction of the ions remains in the target area, and what fraction escapes, or is guided, to the substrate, allowing us to utilize the beneficial effects of ion assistance to film growth. Therefore, one would expect that much research effort has been spent to develop HiPIMS-optimized magnetrons. Some but not many studies are actually devoted to this subject. Generally, a stronger magnetic field leads to higher ionization but also to a greater return of ions to the target: one finds greater self-sputtering and gas recycling but lower deposition rate. Greater unbalance helps to guide the plasma to the substrate (using an additional coil<sup>97</sup> or a permanent ring magnet<sup>98</sup>) but increased plasma losses may delay the transition to HiPIMS characterized by self-sputtering and gas recycling. Based on those statements, a HiPIMS magnetron does not have to have a very strong but rather an unbalanced magnetic field, while the discharge can be driven to the HiPIMS mode by higher applied voltage.

In HiPIMS, as a side effect of spoke formation, ion fluxes “sideways” can be slightly enhanced, as angle-dependent particle flux studies have revealed.<sup>99,100</sup> Generally it is desirable to put fluxes in the direction normal to the target surface, where the substrate is usually positioned. This can be promoted by adding a magnetic solenoid field which is superimposed on the magnetron’s permanent magnet field,<sup>97,101</sup> or by changing the permanent magnet structure to obtain a stronger magnetic imbalance.<sup>102</sup> The effective magnetic field can be reduced using exchangeable spacers between target and magnets in order to increase the ion flux to the substrate and enhance the deposition rate.<sup>103</sup> The magnet structure itself can be optimized to improve target utilization and also to enhance the ion flux to the substrate, greatly mitigating the typical reduction of deposition rate.<sup>104</sup>

Gas density is another very important factor for the transport of ions to the substrate. In this context, one can speak of high and low gas density depending whether or not the flux of ions is greatly impeded by collisions with gas atoms or molecules. The gas density on the pathway to the substrate is determined, at least initially, by the process gas pressure according to Eq. (28),  $n_g = p_g / kT_g$ , where the initial gas temperature can be set to about 300 K. The mean free path for ions with respect to collisions with gas atoms is given by the general formula

$$\lambda_i = \sum_g (\sigma_{ig} n_g)^{-1} \quad (30)$$

where  $\sigma_{ig}$  is the cross section for interaction of ions of type  $i$  with gas atoms or molecules of type  $g$ , and  $n_g$  is the density of particles of type  $g$ . As was mentioned in the dcMS section, rarefaction is significant even in dcMS. One should expect even greater effects in HiPIMS, albeit in a dynamic sense because rarefaction is driven during the pulse, while gas is refilled in the time between pulses. As shown in Fig. 25, a background pressure of about 1 Pa separates what can be considered regions of “low” and “high” pressures. This pressure value is for orientation only, as the effect of collisions will greatly depend on the mass ratio of sputtered atoms and gas atoms: lighter target ions are more affected than heavier due to momentum transfer in the collisions.

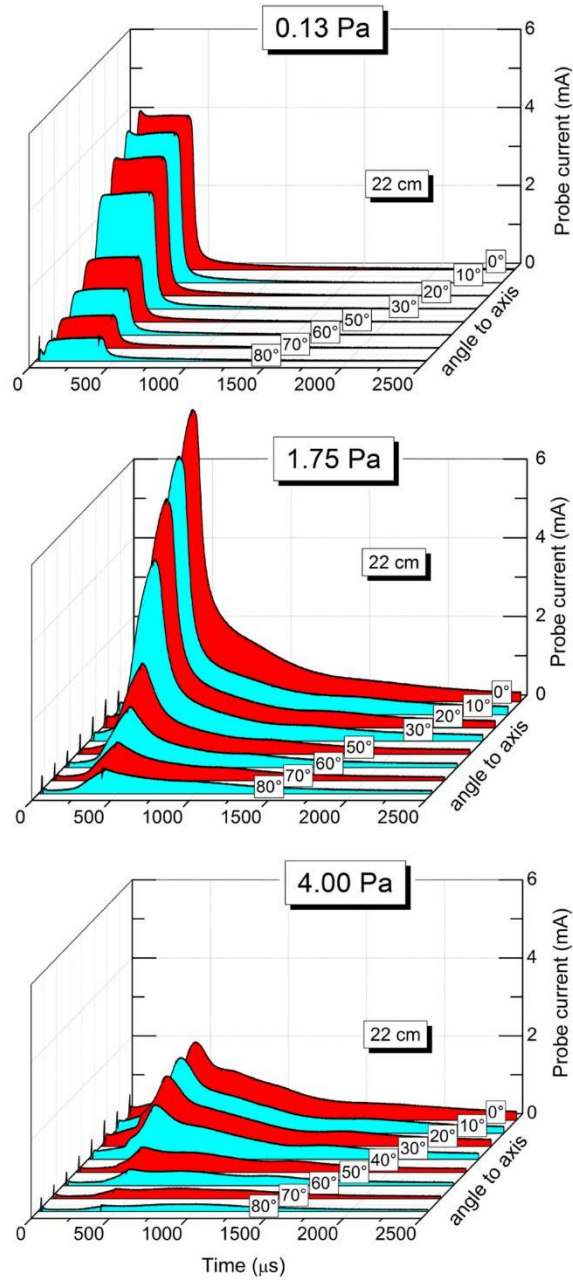


FIG. 25. Probe ion saturation currents were measured by 9 probes, all having 22 cm distance to the target center, at angles from 0° to 80° to the normal of the target surface; Cu target, argon pressure as indicated, 1000 V at target for 400  $\mu$ s, 34 A steady-state current after about 50  $\mu$ s into the pulse. The effect of gas pressure on the transport of ions to the substrate: Top: at low pressure, ions move fast and the time-of-flight to a distance of 22 cm is small compared to the pulse length of 400  $\mu$ s; Center: at a pressure exceeding 1 Pa, most ions arrive at 22 cm only after the pulse is over, and the long tail shows that ions having different (lower) velocity arrive late; Bottom: at high pressure, ions arrive very late with respect to the HiPIMS pulse, the ion current is greatly reduced (Reprint of part of Fig. 3 from ref.<sup>105</sup>, with permission of AIP Publishing).



Gas rarefaction in HiPIMS has one additional component besides gas heating and sputter wind, namely rarefaction by ionization. Gas neutrals are removed by becoming ions, and ions quickly leave the region because they respond to the local electric field. Gas rarefaction for short-pulse HiPIMS (20  $\mu$ s) has been quantified by laser-induced fluorescence (LIF), a direct, non-perturbing method for measuring density.<sup>106</sup> It was shown that the characteristic time to establish rarefaction is 10  $\mu$ s, and it takes about 100  $\mu$ s for the background gas to refill the rarefied volume. Not coincidentally, the refill time matches the estimate  $t_{\text{refill}} \approx s/v_{\text{sound}}$ , where  $s$  is the characteristic size of the rarefied region and  $v_{\text{sound}}$  is the sound velocity. It should be noted that the work<sup>106</sup> is an example for short-pulse HiPIMS, where each pulse is terminated well before the current could reach a new steady-state. This has the advantage that the arcing issue is less of a problem (recall the previously mentioned pulse duration experiment by Belkind<sup>78</sup>), however, it is also more difficult to utilize the full benefit of HiPIMS as the transition to a metal-dominated plasma occurs only later in each HiPIMS pulse.

## VII. REACTIVE HIGH POWER IMPULSE MAGNETRON SPUTTERING (R-HiPIMS)

### A. Physics of R-HiPIMS

We finally arrive at the last, yet central topic of this tutorial: R-HiPIMS. Having all the “ingredients” discussed before, most features of R-HiPIMS can be understood in terms of previously discussed features such as the magnetron plasma evolution during each pulse, finding a suitable partial pressure of the reactive gas, pulse repetition rate, pulse duration, etc.

Pioneering work towards R-HiPIMS (reported by Ehasarian and workers in 2002,<sup>107</sup> and in greater detail in 2006<sup>108</sup>) was done in conjunction with interface engineering based on the metal ion etch concept, originally known as arc-bond-sputtering,<sup>109</sup> prior to the deposition of a compound film. In a first step, HiPIMS was done in a non-reactive mode with the substrate biased to -1200 V, in order to remove contaminants by sputtering and to produce a mixed-metal interface by shallow ion implantation. This was followed by R-dcMS to deposit a compound film at much lower substrate bias. Strictly speaking, none of the two steps was R-HiPIMS but this work suggested going the next step, namely to also use HiPIMS for the reactive sputter deposition step. Indeed, as reported as early as in 2003, CrN was deposited by HiPIMS, and a number of improved mechanical films properties have been measured as compared to dcMS and arc-deposited films.<sup>110</sup> Since then, more than 100 papers have been published specifically on R-HiPIMS deposition (and more than 1000 papers on HiPIMS in general). Table 1 in Section VII D compiles some R-HIPMS studies which most often target improvements to specific coating systems. Instead of looking at the chronological development, these studies are organized by material systems. In the following, however, we focus on the peculiarities of R-HIPMS plasma physics and chemistry.

We have previously considered that HiPIMS can be defined by the relative role of self-sputtering and gas recycling, which greatly depends on the yield of sputtering, which in turn depends on the surface binding energy. By introducing reactive gas and forming a compound film on the target, the sputter yield is always reduced because the bond strength of compounds is greater than the bond strength of the metal target. Therefore, it is clear that poisoning the target reduces the role of self-sputtering and increases the role of gas recycling.<sup>84,111</sup>



This can be seen in the current-voltage-time characteristics, which in R-HiPIMS<sup>112</sup> are distinctly different from the current-voltage-time characteristics of HiPIMS.<sup>83</sup> As the target is more poisoned at decreasing pulse repetition rates (and constant pulse duration), the current shape changes from flat to rising (Fig. 26).

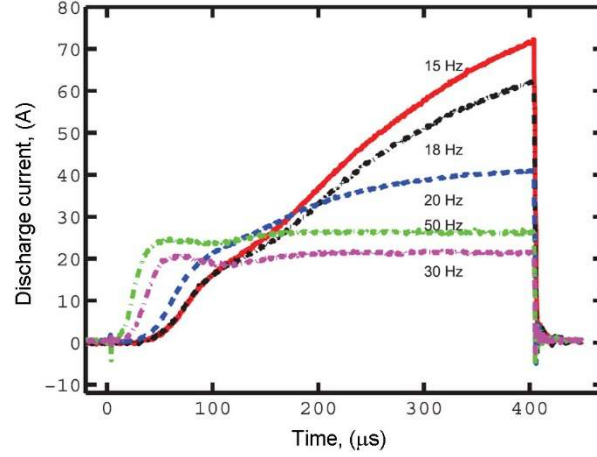


FIG. 26. Discharge current waveforms for a Ti-Ar/O<sub>2</sub> R-HiPIMS system, operated at a constant voltage of 600 V for 400 μs, at a pressure of 0.6 Pa with 30 sccm Ar and 2 sccm O<sub>2</sub> flow. Reducing the repetition rate, at constant pulse duration, shifts the target toward a more poisoned state, with very significant changes for the current (Reprinted data from Fig. 1 of ref.<sup>113</sup>, with permission from the American Vacuum Society).

Gudmundsson and coworkers<sup>111</sup> quantified this shift to increased gas recycling using an ionization region (IR) model for the Ti – Ar/O<sub>2</sub> R-HiPIMS system. They generalized the previous IR model by including the rate equations for plasma-chemical reactions involving the reactive gas. Rate equations have the general structure<sup>111</sup>

$$\frac{dn_{\text{species}}}{dt} = \sum R_{\text{species, process}} \quad (31)$$

where the left hand side is the rate of density change for the type of particle species under consideration, and the right hand side sums all production and loss rates  $R_{\text{species, process}}$  for particles of the “species” type, including also terms that describes the influx and loss of particles from the volume by drift and diffusion. As with the non-reactive IR model, all processes in the reactive IR model are volume-averaged. Earlier in this tutorial, a rate equation was already introduced, namely Eq.(25) for the density of ions. For binary collisions, such as the electron impact ionization,  $\text{Ar} + e^- \rightarrow \text{Ar}^+ + 2e^-$ , the rate is proportional to the densities of the two species involved (e.g. the argon gas density  $n_{\text{Ar}}$ , and the electron density  $n_e$ ) multiplied by a rate coefficient such as written in Eq. (26). As one can see from Eq. (26), rate coefficients are related to collision cross sections and the energy distribution function(s). In case of collisions with electrons one considers the kinetic energy of electrons since the other collision partner has relatively little kinetic energy. In a plasma-chemical model, one has to write rate equations

for each species. Each type of collision is treated like a chemical reaction. Metastable atoms or, more general, species in excited states should be handled as a separate species, if needed.

It becomes clear that many simplifications and assumptions need to be made to make the problem tractable. In particular, one has to make assumptions to arrive at readily useable rate coefficient since the coupling to actual energy distribution functions can only be made in much more comprehensive numerical models. In equilibrium, electrons have a Maxwellian energy distribution function. Due to energetic secondary electrons from the target, it is clear that a Maxwellian distribution is not applicable but one can use an approximation considering two groups of electrons: the “cold” electrons of the plasma, which have energies of a few eV, and the energetic or “hot” electrons, whose energy may be as high as the corresponding voltage drop in the sheath, i.e. several 100 eV. The assumption of two Maxwell distributions allows us to solve the integral for the rate coefficients. The density of low energy electrons can be approximated by the quasi-neutral condition, Eq. (18), and the density of hot electrons, averaged of the IR volume, is determined by the energy density of hot electrons divided by the corresponding temperature term  $kT_{e,hot}$ .<sup>111</sup>

The rate coefficients are usually expressed in an analytical form with the (hot) electron temperature as a variable. For example, Gudmundsson lists 4 types of plasma-chemical reactions and their rate coefficient for electron-argon collisions, involving the argon ground state and the metastable state of argon, and 22 plasma-chemical reactions for electron-oxygen collisions. The number is so high since many processes involve molecules at different excited states as well as positive and negative oxygen ions. Furthermore, there are 11 types of oxygen-oxygen reactions, and 5 types of argon-oxygen collisions. The system of rate equations is completed by 2 types of electron-titanium collisions, 2 types of argon-titanium collisions, and 2 types of oxygen-titanium collisions. At first, it seems that there are too many free fit parameters that would prevent researchers to find a reasonable and consistent set of values. Luckily, it turns out that when fitting experiments, some parameters must be kept in a very narrow range to reproduce experimental curves. Once those parameters are locked, such as the return probability of ions to the target, the recapture probability of secondary electrons by the target, and the potential drop across the ionization region, the other parameters follow. They give great insight into plasma composition of the IR volume and flux ratios from and to that volume, including the currents carried by different types of ions going from the IR to the target (Fig. 27).

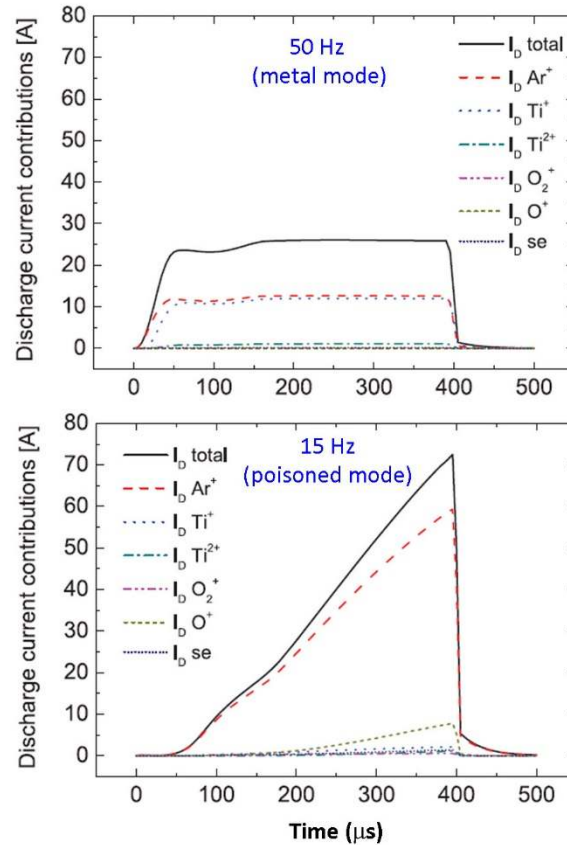


FIG. 27. Example of an ionization region model output: the evolution of ion currents to the target for high pulse repetition rate (target is in metal mode, top figure) and low repetition rate (target is poisoned, bottom figure) (Reprint of Fig. 7 from ref.<sup>111</sup>, with permission of IOP Publishing Ltd).

Reactive magnetron sputtering was associated with poisoning of the target and appearance of hystereses in several parameter pairs such as deposition rate versus partial pressure of the reactive gas. In an early publication in 2008, Wallin and coworkers<sup>114</sup> reported that the hysteresis vanishes when R-HiPIMS is done under certain conditions. As was pointed out by others,<sup>115</sup> hystereses may be reduced but do not disappear completely; they generally exhibit the same features as in dcMS. The effect greatly depends on the relation of the two pumps described in the reactive sputtering section. In a small research system, as used by Wallin *et al.*,<sup>114</sup> the physical pump dominates over the getter effect by the “film pump”, which is not the case in large industrial systems.

In any case, it is interesting to consider why the hystereses are reduced or even vanish. Wallin *et al.*<sup>114</sup> argue that the sputtering rate during pulses is greater than in dcMS, and the formation of a compound layer between HiPIMS pulses is reduced due to gas rarefaction, which also includes rarefaction of the reactive gas. A study by Kubart and coworkers<sup>116</sup> using a Ti-Ar/O<sub>2</sub> R-HiPIMS system supported this interpretation. Using the Monte Carlo code TRIDYN<sup>117</sup> for an Al-Ar/O<sub>2</sub> system, a range of pulse configurations were simulated for different oxygen partial pressures.<sup>118</sup> The results indicate that the target effects alone are not sufficient to explain the observed shift of hysteresis and its frequency dependence, rather rarefaction and refill and other effects need to be included in the model.

Considering a Nb-Ar/O<sub>2</sub> R-dcMS and R-HiPIMS system, Hála and coworkers<sup>119</sup> confirmed that the hystereses are greatly reduced, allowing them to deposited TiO<sub>2</sub> in a controlled manner with high deposition rate, which should be normalized to the average power to the system (Fig. 28).

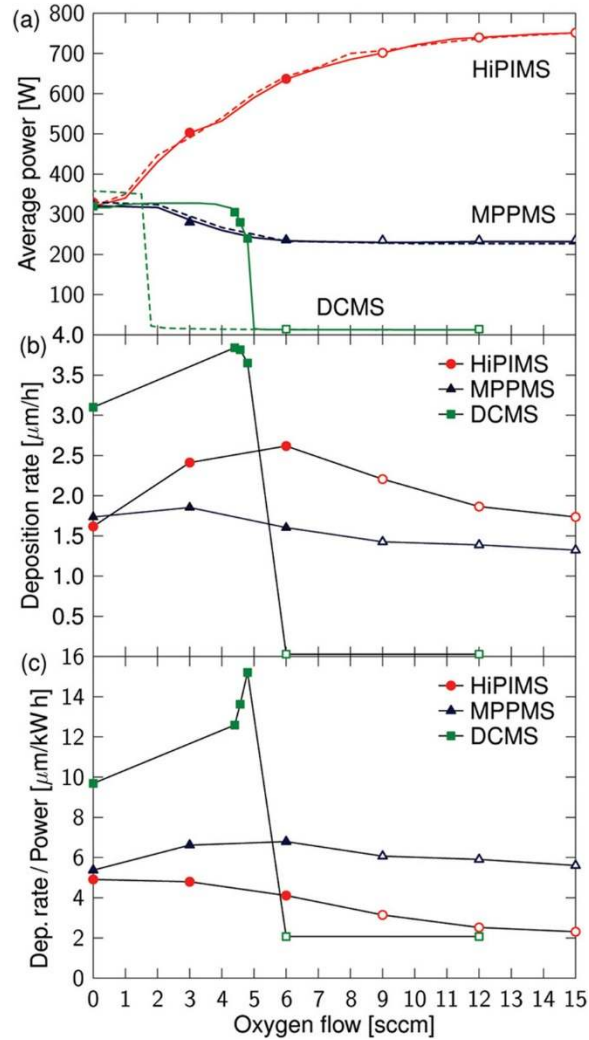


FIG. 28 (a) Average discharge power; (b) deposition rate; (c) power-normalized deposition rate for the Nb-Ar/O<sub>2</sub> system using dcMS, HiPIMS and MPPMS to deposit NbO<sub>x</sub> films, as a function of oxygen flow rate. The solid and dashed lines in subfigure (a) stand for experiments with increasing and decreasing oxygen flows, respectively. Fall and open markers indicate absorbing and transparent coatings, respectively (Reprint of Fig. 3 from ref.<sup>119</sup>, with permission of the IOP Publishing Ltd).

From Fig. 28 we see that the deposition rate for HiPIMS and MPPMS (modulated pulsed power magnetron sputtering, see section VII B) is notably lower than the dcMS value, however, once in the poisoned mode, the deposition rate is greater than that of dcMS. In the transition regime, at 6 sccm O<sub>2</sub> flow, the R-dcMS film is transparent while the R-HiPIMS and R-MPPMS films are still metallic.

Comparing R-dcMS and R-HiPIMS, one of the many differences is in the kinds of particles coming to the target. In the former case, the ion flux is primarily composed of noble gas ions, whereas in R-HiPIMS we

have a mixture of noble gas, reactive gas, and metal ions. This clearly will affect the chemical composition and compound formation of the target surface and sub-surface. A parametric model along the “Berg model,” using fractional coverages of the target and substrate with compound layers can be used to approximately determine the system’s behavior. For example, Kozák and Vlček<sup>63</sup> predicted and optimized R-HiPIMS deposition of  $\text{ZrO}_2$  in this way.

The evolving plasma composition in front of the target is experimentally best investigated by non-perturbing methods such as emission spectroscopic, or using optical interrogation by absorption spectroscopy or laser-induced fluorescence. Hála used a spectroscopic imaging technique with fast cameras and spectrally selective filters to distinguish light from metal and gases, and from atoms versus ions.<sup>94,120</sup> The camera’s time resolution was slower than the characteristic time of spoke motion, and therefore spokes were not visible while the overall development could be well documented. Series of images (such as those shown in Fig. 29) give semi-quantitative insights. For example one can see increased ionization of the reactive gas as the discharge develops in each pulse: the emitted light intensity switches from light emitted by neutral gas atoms to light coming from ionized gas, which is especially concentrated in the very near-target region. In the poisoned mode, when operating in oxygen, the discharge goes to high current but not to a mode dominated by metal self-sputtering.<sup>94</sup> A metal-dominated phase does not exist under those conditions. Emission from gas plasma species remained dominant, which we now understand as mode dominated by gas recycling. For example, sputtering Cr in  $\text{Ar}/\text{N}_2$  mixture and lead to a Cr-dominated plasma late in each HiPIMS pulse, while in  $\text{Ar}/\text{O}_2$  mixtures sputter-removal of the poisoned layer was found insufficient, shifting the plasma to oxygen but not metal-dominated plasma.<sup>94</sup>

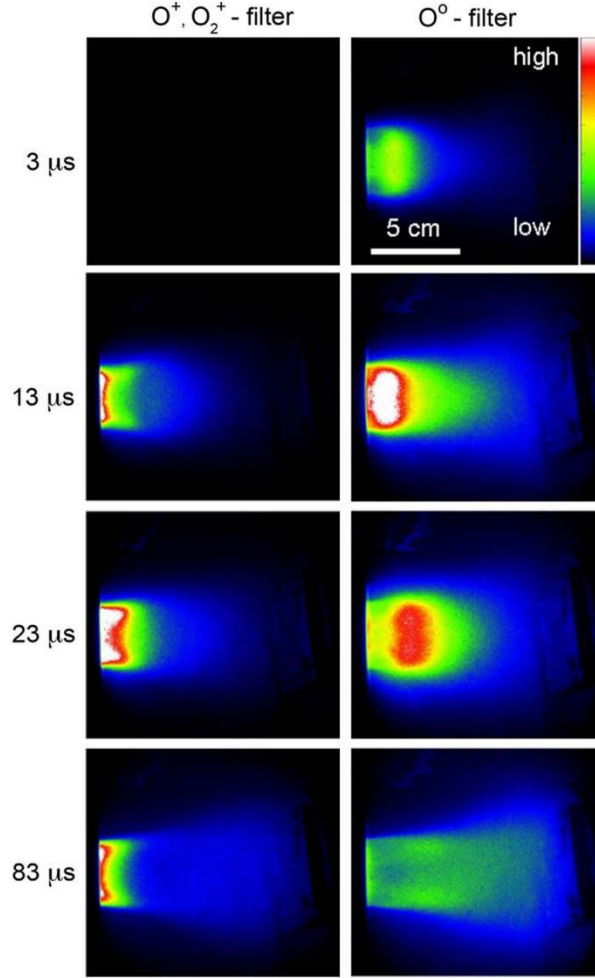


FIG. 29. High-speed camera images taken during 200- $\mu$ s R-HiPIMS pulses for a Cr target (left of each image) sputtered in 1.7 Pa  $O_2$ ; images are taken through spectral filters passing light from ionized oxygen (left column) and neutral oxygen atoms (right column) (Reprint of Fig. 2 from ref.<sup>94</sup>, with permission from IEEE).

Optical techniques also reveal dissociative electron attachment to a metastable oxygen molecule,



producing a negative oxygen ion and an (excited) oxygen atom. This happens with low energy electrons especially just after the HiPIMS pulse has ended.<sup>121</sup> Experiments with an additional solenoid, described later, provided evidence for the role of atomic oxygen in the afterglow for the poisoning state of the target.<sup>122</sup> Oxygen atoms are highly reactive and contribute to a more rapid compound film formation on the target in R-HiPIMS compared to R-dcMS.

There are factors, such as transport of radicals, electron-ion recombination, etc., that also occur. Fig. 27 suggested that films sputter-deposited on a substrate with 6 sccm  $O_2$  are stoichiometric (transparent) compound films in R-dcMS, whereas the R-HiPIMS films are sub-stoichiometric. One needs to consider

atomic ion and radical transport to both target and substrate to understand the sometimes conflicting reports.

Similarly complicated is the effect of the type of noble gas on poisoning because not only the mass is changed when exchanging the usual argon gas with another noble gas (He, Ne, Kr, Xe) but also the secondary electron yield, the ionization energy, momentum transfer in collisions, etc. Focusing on the gas effect on the power-normalized deposition rate, and looking at the Ti-noble gas/O<sub>2</sub> system, it was found that R-HiPIMS with krypton has the least rate reduction,<sup>123</sup> Fig. 30, suggesting that krypton is preferable. However krypton is notably more expensive than argon, and likely argon remains the noble gas of choice. The ionization and metastable energies are higher as we go to lower-mass noble gases, which implies higher secondary electron yield, see Eq. (13), and an enhanced role of energy transfer from metastable states. As a side note, these noble gas effects can be utilized to improve deposited hard amorphous carbon films by HiPIMS, and hydrogenated diamond-like carbon (DLC) films by admixing neon in a HiPIMS Ar/C<sub>2</sub>H<sub>2</sub> discharge.<sup>124</sup>

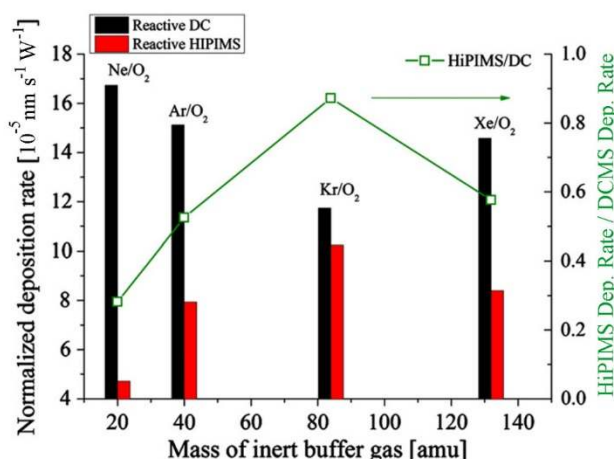


FIG. 30. Power-normalized deposition rates for dcMS (black bars, left column) and HiPIMS (red bars, right column) for different inert gases mixed with oxygen, with their ratio shown as open squares related to the right hand axis; the xenon result might have been an outlier since the experiment with Xe was done at half the average power of the other three experiments (Reprint of Fig. 7 from ref.<sup>123</sup>, with permission from Elsevier).

Secondary electron emission is much more dynamic in R-HiPIMS than in other forms of MS for several reasons, namely, both the target surface composition is dynamic, and the incoming flux of ions is dynamic, too. Here we not only refer to intensities of particle fluxes but most importantly to the composition of the incoming ion flux that changes during each pulse.

Let's parse those effects for clarity. The arrival of reactive gas leads to compound formation (poisoning). In R-HiPIMS, a fraction of the reactive gas is ionized and thus arrives at the target with high energy leading subplantation (shallow ion implantation). In contrast to noble gas ions, not all implanted reactive gas atoms will diffuse back to the surface but a fraction will chemically react and thereby become part of the target. In other words, "poisoning" of target occurs on and below the surface.

Besides reactive gas, noble gas ions and metal gas ions arrive too, all being subplanted and all contributing to sputtering. Arrival, retention and removal of compound-forming reactive gas atoms are competing processes. The resulting target surface composition affects both sputter yield and the yield of secondary electrons. The fluxes of atoms and electrons from the target affect the near-target ionization rate, and hence the ion fluxes that bombard the target just microseconds later, as was illustrated in Fig. 19. The difference to the previous discussion, the one made about Fig. 19 in the section on non-reactive HiPIMS, is the involvement of the reactive gas, a gas that can change the target and can be “recycled” on its own. Therefore, a generalization is in order, as schematically shown in Fig. 31.

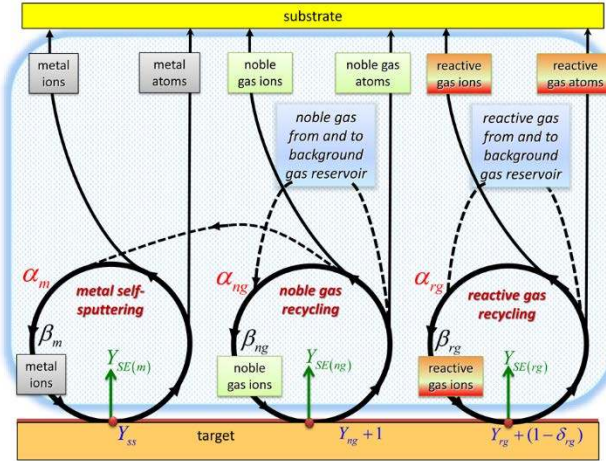


FIG. 31. A busy yet simplified schematic of fluxes in R-HiPIMS: each type of ions can arrive at the target, cause sputtering and secondary electron emission, the yields of which depend on the type of ion and the chemistry of the surface; noble gas atoms return from the target with a yield close to 1, and reactive gas atoms with a yield  $1 - \delta_{rg}$ ,  $\alpha$  is the probability for ionization, and  $\beta$  the probability of an ion to return to the target. While each species can have its own circle, these paths are not independent: for example, the dash line from noble gas to the metal species circle indicates one relationship, namely the role noble gas plays to initiate the metal circle. All relationships are dynamic, time dependent, and the surface state depends on partial pressures and ion fluxes.

Coming back to the “two pump” picture, which applies to all reactive sputtering system, including R-HiPIMS and consider an educational case of slow periodic oscillations observed in R-HiPIMS under constant voltage conditions (HiPIMS supply is based on switched capacitor bank charged to that voltage) and constant reactive gas supply, constant pulse duration and constant repetition rate. Upon introduction of the reactive gas with a partial pressure that puts the system in the transition region, the target will “poison,” which is followed by a very significant increase in current and power, see Figs. 26 and 27. This can then lead to a removal of the compound layer and return of the target to the metal state, characterized by lower current and power. One can observe spontaneous, repetitive switching between the metal and poisoned state on a time scale of seconds or minutes.<sup>125</sup> To stabilize the system one would need to control the partial pressure and/or the pulsing parameters.



With the two pump picture and the power dependence of the target state, one can realize that tuning the target state with the pulsing parameters is a key opportunity of R-HiPIMS compared to R-dcMS. The partial pressure of the reactive gas is critical for the state of the target; it can be adjusted by the supply, i.e. the reactive gas flow rate on the one hand, and by the removal, i.e. the acting of the two pumps, on the other hand. The target state is also dependent on the fluxes of ions coming to the target surface, and thus on the power density. R-HiPIMS offers the elegant opportunity to tune the target state not only by balancing gas supply and pumping but by regulating the power density through pulsing parameters including pulse length, repetition rate, and patterning in bursts. Many of the examples in this tutorial build on this effect.

The relationships indicated in Fig. 31 also depend on the magnetic field, which was in general terms discussed in the sections on magnetrons and HiPIMS. When reactive gas is present, additional effects appear which are related to the magnetization and drift of electrons affecting the dissociation of reactive gas molecules. Radicals (atoms with unpaired valence electrons) are formed that are highly reactive. A stronger magnetic field promotes more dissociation and ionization reactions, which not necessarily translates into a greater ion flux to the substrate, as discussed before. The transport of R-HiPIMS plasma can be facilitated by using a magnetic solenoid field such that the magnetic field lines connect the region of plasma production near the target with the substrate region. Given that a radial electric field is setup in such configuration one speaks of a plasma lens (Fig. 32).

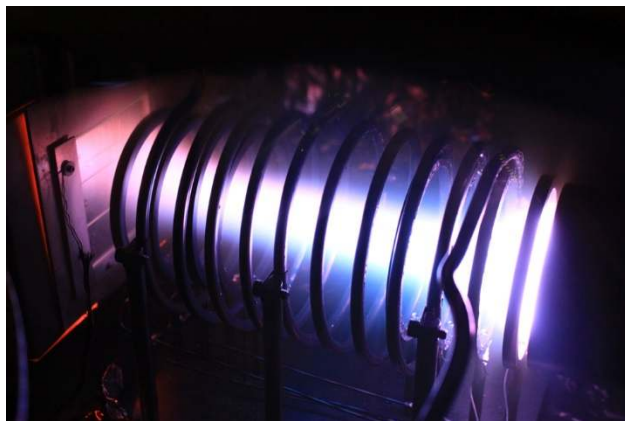


FIG. 32 Plasma lens used in R-HiPIMS of an Al-doped Zn target in an argon-oxygen gas mixture; the 7.5 cm (3") magnetron is on the right, the solenoid is operating at 400 A coil current, and the heated substrate holder is on the left (Reprint of Fig. 1 from ref.<sup>126</sup>, with permission of IEEE).

The plasma lens shown in Fig. 32 has a dual purpose: to focus the flow of low energy positive ions to the substrate, and to de-focus the flow of energetic, damaging negative ions, deflecting them from the designated growth region, in order to obtain high-quality aluminum-doped zinc oxide (AZO), a transparent conducting oxide.<sup>126-128</sup> Experiments aiming to deposit high quality FTO (fluoride-doped tin oxide) in an Ar/O<sub>2</sub>/CF<sub>4</sub> gas mixture indicated suppression but not elimination of negative ions by the plasma lens.<sup>69</sup>

In a next step, one may consider making use of the plasma evolution in each R-HiPIMS pulse by applying synchronized pulsed magnetic fields and/or pulsed bias voltages with suitable delays relative to the

plasma pulse. The general idea of synchronizing pulsed plasma with pulsed solenoids and pulsed bias was already practiced with pulsed arcs in the 1990s.<sup>129,130</sup> Pulsing the magnetic field can be used to enhance or suppress the flux of ions to the substrate for portions of each HiPIMS pulse.<sup>122</sup> Additionally, it was found that not only the plasma flow to the substrate was changed but also the fluxes to the target, which can be used to control the poisoning state of the target.<sup>122</sup>

Substrate bias can be tailored at times when a certain plasma composition has arrived in front of the substrate (“ion-species-selective bias”<sup>131</sup>). This concept can readily be applied to HiPIMS with great benefit to the coating, namely the bias can be applied when the HiPIMS plasma is metal-rich. An elegant study using the  $\text{Ti}_{1-x}\text{Al}_x\text{N}$  system was designed such that bias could be applied either throughout the entire pulse or limited to a time when the plasma is  $\text{Al}^+$ -rich.<sup>132</sup> Since we focus on the R-HiPIMS process here it should suffice to report that selective metal ion bombardment lead to dense, competitive growth columnar structure with strong 111 orientation, no measureable trapped Ar concentration; low stress of 0.9 GPa was assigned to the elimination of phase separation and minimal renucleation during growth.<sup>132</sup>

The ion energy distribution function (IEDF) for different species in R-HiPIMS are quite different depending where and how ions are generated, and at what time in the HiPIMS pulse one measures such distributions. For film growth, the time-integrated energies are relevant, and indeed those are the most studied since additional time-resolution requires additional equipment and effort. Fig. 33 shows a typical set of IEDF for the Cr-Ar/ $\text{N}_2$  system. The IEDF for chromium and atomic nitrogen ions are very similar, having a long energy tail, while the distributions for argon and molecular nitrogen are much less energetic.

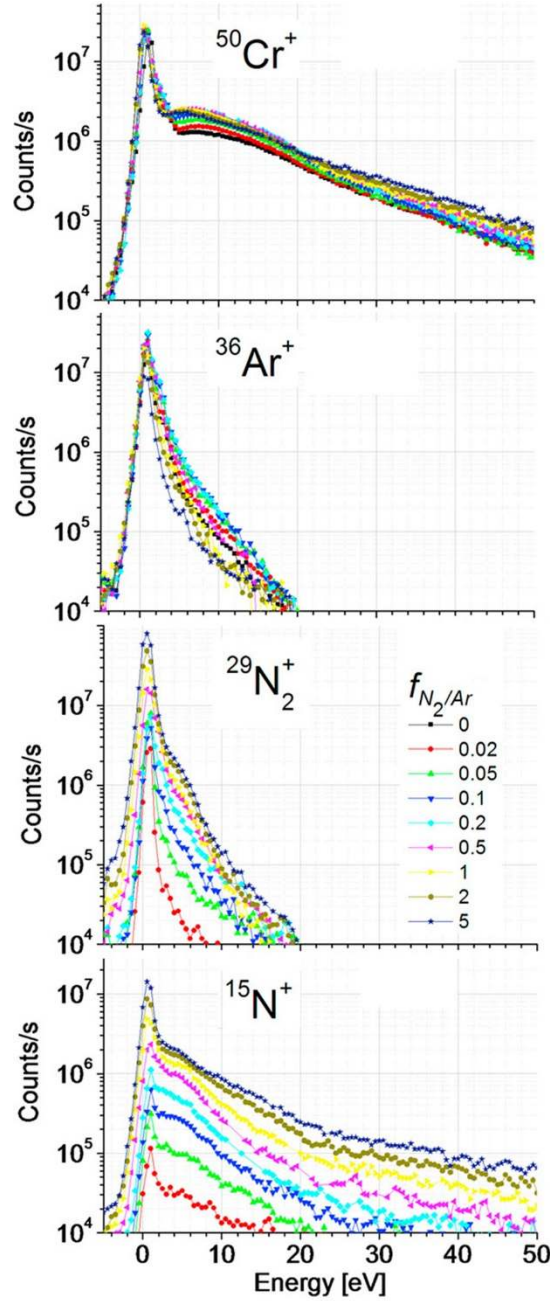


FIG. 33. Time-averaged IEDFs for:  $\text{Cr}^+$ ,  $\text{Ar}^+$ ,  $\text{N}_2^+$ , and  $\text{N}^+$  ions, measured at a total pressure of 0.4 Pa and different  $\text{N}_2/\text{Ar}$  flow ratios (Reprint of Fig. 6 from ref.<sup>133</sup>, with permission of Elsevier).

With information from spectroscopic imaging, e.g. Figs. 24 and 29, one can derive that  $\text{Cr}^+$  and  $\text{N}^+$  ions were produced close to the target, while  $\text{Ar}^+$  and  $\text{N}_2^+$  appear at larger distances. This suggests that at least a part of the ion acceleration must be due to a mechanism that cannot be described by the *average* potential distribution (as indicated in Fig. 15) because that would mean acceleration towards the target, not toward the substrate or detector. This, in turn, points to the importance of localized collective processes, such as spokes and flares, allowing ions to reach high energies facilitated by local,

time-dependent electric fields. Such interpretation is consistent with other observations that indicated higher energy for double and higher charged ions, and asymmetry in the ion energy distributions relative to the  $\mathbf{E} \times \mathbf{B}$  direction<sup>100,134</sup> (Fig. 34). The peak at low energy is likely due to the plasma in the decay phase, after the HiPIMS pulse power is switched off.

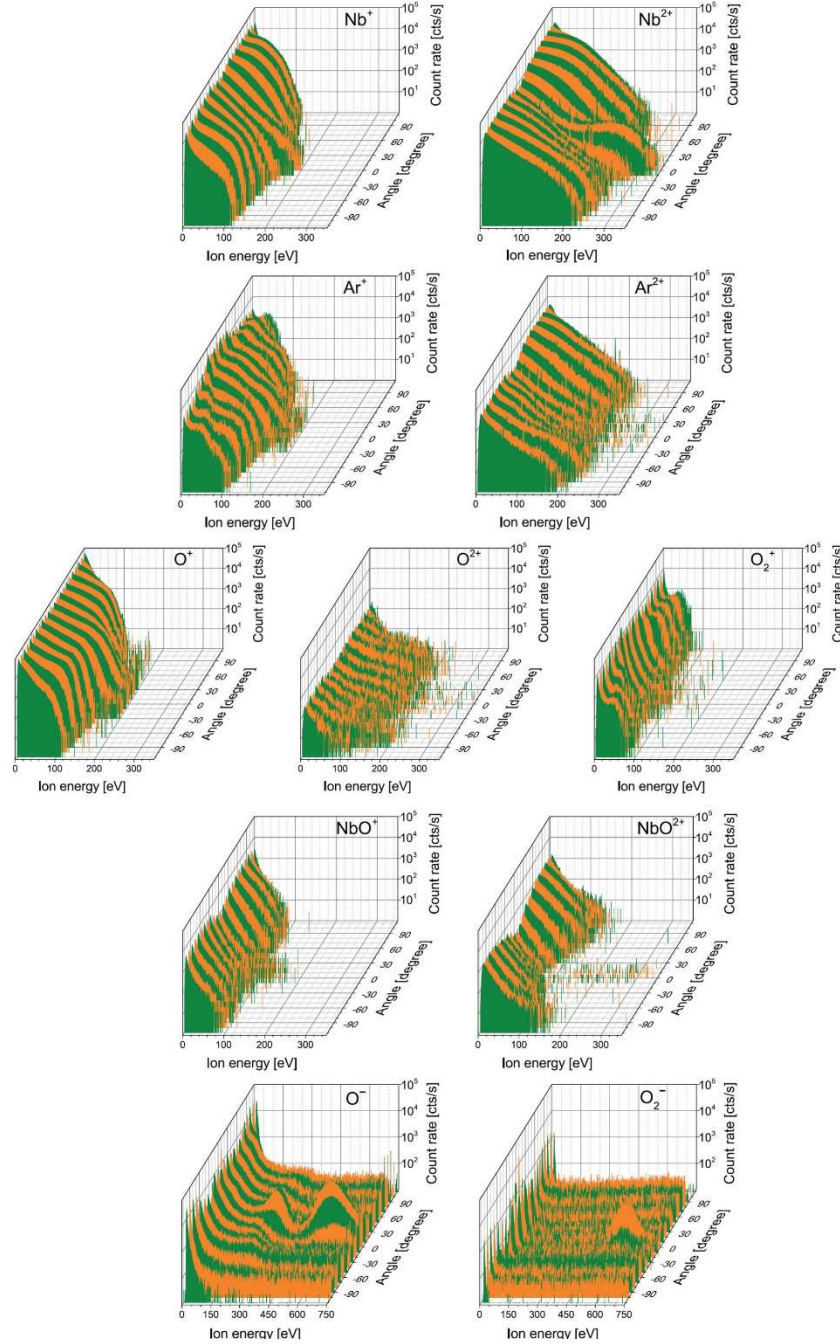


FIG. 34 IEDF for the Nb-Ar/O<sub>2</sub> R-HIPIMS system; as measured with an EPQ300 mass and energy analyzer, as a function of angle, where 0° refers to the target surface normal; 7.5 cm Nb target, 200  $\mu$ s pulses, 100 Hz, peak current 110 A; while most ions are positive and single charged, the R-HIPIMS plasma also

contains double charged, molecular, and negative ions, as indicated in these subfigures (Reprinted from Figs. 4-8 from ref.<sup>134</sup>, with permission from IOP Publishing Ltd).

## B. Hybrid and extended technologies

There are several main approaches to modify and extend HiPIMS, and especially R-HiPIMS:

- (i) to group one or more pulses making use of the previous pulse's plasma and effect on the target state (burst HiPIMS),
- (ii) to superimpose pulses with dcMS or pulsed-dcMS on the same target, i.e. to also use the time between pulses,
- (iii) to combine a HiPIMS magnetron with another magnetron, which most often is run in dcMS or pulsed-DC mode to mitigate the reduced deposition rate of HiPIMS, and also to enable new effects on the microstructure of the coated films,
- (iv) to use more than one HiPIMS magnetron in dual magnetron configuration to address the “disappearing anode” problem, and/or to increase the area that is coated without the need to further increase the peak power.

Not all of these approaches can be discussed here, but some points deserve to be highlighted. An important variation to HiPIMS and R-HiPIMS is an approach where a long pulse (a “macro-pulse”) is chopped in many  $\mu\text{s}$ -long sub-pulses (“micro-pulses”) – known as modulated pulsed power (MPP) magnetron sputtering (MPPMS). In each macro-pulse, at least two power levels of micro-pulsing are employed: the degree of ionization in the plasma is controlled by the average power in those segments of micro-pulses. Typically, each macro-pulse starts with a lower power level, followed by a higher power level (Fig. 35). The power level is adjusted via the duration and frequency of micropulses, as opposed to setting the applied voltage in conventional HiPIMS or R-HiPIMS.

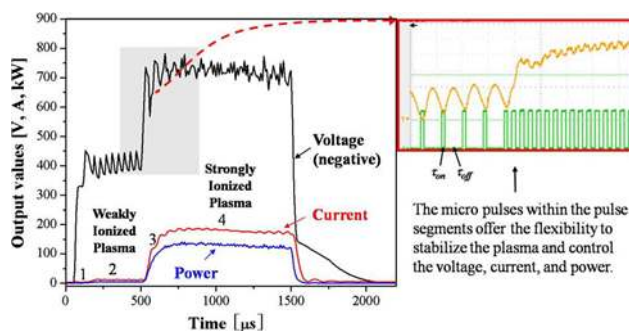


FIG. 35 Voltage, current, and power for a typical MPP approach: the right inset shows that the frequency of “micropulses” is used to control the average power in each segment of the “macropulse” (Reprint of Fig. 1 from ref.<sup>135</sup>, with permission by Elsevier).

The general philosophy of MPPMS is that the degree of ionization does not have to be very high in order to utilize the beneficial effects of ion-assistance to film growth, rather, in order to make HiPIMS

technology more competitive, it is necessary to avoid significant reductions of deposition rate usually found in HiPIMS and R-HiPIMS. MPPMS shows less of such reduction as demonstrated for example for the non-reactive Cr-Ar system,<sup>136</sup> and for the reactive Cr-Ar/N<sub>2</sub> system to deposit CrN and Cr<sub>2</sub>N films.<sup>137</sup>

A similar but somewhat simpler approach is Deep Oscillation Magnetron Sputtering (DOMS) where a macro-pulse is composed of a burst of micro-pulses. This has been used to tailor the phases of TiO<sub>2</sub>, ref.<sup>138</sup>, and of Cr<sub>2</sub>O<sub>3</sub>, ref.<sup>139</sup> MPPMS and DOMS are often considered as processes placed between pulsed-dcMS and HiPIMS, as schematically shown in Fig. 36.

This schematic is for orientation only and has at least two shortcomings. First, MPPMS and DOMS have at least two duty cycles, namely a duty cycle of micro-pulses and a duty cycle of macro-pulses. Since this diagram is about power, “the” duty cycle could be understood as the product of both duty cycles.

Another comment is needed to explain the *nominal* peak power density. *Nominal* refers to a normalization of power on the *entire* target area. Often, peak power density is given without the word “nominal” — a practice wide-spread in the literature but somewhat flawed since only a part of the target area is actually utilized. A more useful definition is to normalize to the target area actually used, i.e. the racetrack area. This is also somewhat arbitrary since the width of the racetrack area depends on magnetic field configuration, power and pressure, yet it is much more meaningful than using the entire target area. Alternatively, rarely used, but more reasonable, would be to normalize power by the length of the racetrack (as done in the caption of Fig. 14). Using racetrack area or length, one can more easily compare magnetrons of different target and racetrack shapes.

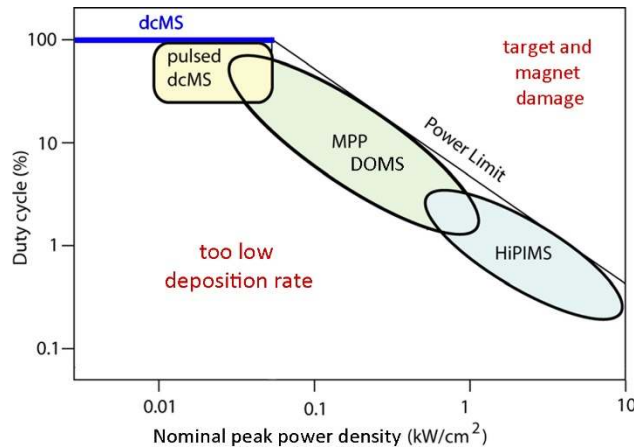


FIG. 36. Schematic showing various forms of magnetron sputtering in a duty-cycle – nominal peak power density diagram (Reprinted Fig. 1 from ref.<sup>140</sup>, with permission from AIP Publishing)

In some studies, several HiPIMS pulses were bundled to create bursts of HiPIMS pulses (burst-HiPIMS,<sup>141</sup> or chopped-HiPIMS<sup>142</sup>), to increase the degree of ionization of sputtered atoms as well as to mitigate the reduction of the deposition rate.

The most common approach to the low deposition rate issue is to combine one or more HiPIMS magnetron(s) with dcMS, thereby preserving most of the deposition rate while also having ion-assistance to film growth.<sup>132,143,144</sup> Multi-magnetron setups are often designed in a *closed field*

*configuration* where the combined magnetic fields are set up to reduce plasma losses to the chamber wall.<sup>145-147</sup>

### C. Arc handling and process control

R-HiPIMS has certainly much greater challenges in terms of process control than non-reactive HiPIMS. This refers to finding the desirable working point on the current-voltage-time characteristics as affected by the partial pressure of the reactive gas, and influenced by a host of factors such as target area, power density, magnetic field strength and topology (balanced versus unbalanced,<sup>148</sup> presence of other magnetrons to produce a closed field structure,<sup>145,147</sup> guiding solenoid,<sup>122</sup> etc.).

Most importantly is to have a power supply featuring fast arc detection and arc handling capabilities.<sup>149</sup> Today, advanced HiPIMS supplies, featuring arc suppression, are offered by several vendors. This has removed a major barrier to the broad application of HiPIMS and R-HiPIMS technologies. In conventional power supplies, and early HiPIMS supplies, a sudden increase in current beyond a preset current threshold is used as the criterion for the detection of arcing. As we scale to larger targets and systems, HiPIMS supplies could be fooled to detect “arcs” since the HiPIMS process involves high peak currents (for industrial systems up to 1 kA, or even higher). This is especially true when the target poisons, see Figs. 26 and 27, yet the discharge is not an arc. Sensing both discharge voltage and current, i.e., discharge impedance  $Z(t) = V(t)/I(t)$ , allows modern systems to detect and respond to arcs on a time scale not much longer than 1  $\mu$ s. Due to inductive energy stored in cables, the cable length between supply and magnetron should be minimized. Some suppliers use strategies of minimizing the energy delivered to the magnetron should an arc occur, including mounting the supply next to the magnetron, but a discussion of those details is beyond the scope here.

As explained before, it is desirable to have a high rate process of depositing compound films with the correct stoichiometric composition. This requires developing a process preferably with the target not in the fully poisoned state. In the following, just a few approaches are described how to control an R-HiPIMS process.

First it should be noted that each target has its history, which affects arcing and process stability. Many researchers and practitioners therefore use a system with a shutter in front of the magnetron and condition the target to a desired surface state before starting the coating process by letting the target run behind the shutter in a noble gas or prescribed gas mixture. This can take many minutes. One often monitors the arc rate as a measure of target condition.

The *pulse length* in R-HiPIMS has been identified as one (of many) important parameters determining the poisoning state of target. By increasing the pulse length it was shown<sup>150</sup> that one can achieve a gradual, smooth transition from a poisoned target to a quasi-metallic target. Appropriate selection of the pulse length may even eliminate the need for active regulation, as demonstrated for the deposition of amorphous HfO<sub>2</sub> by R-HiPIMS.<sup>150</sup> In this experiment, the pulse repetition rate was kept constant at 100 pulses per second, with increasing average power at longer pulse lengths. One can also approach the control from the *duty cycle* point of view: one can find a gradual transition from a poisoned target state at low duty cycle to a quasi-metallic state at high duty cycle. Also here, appropriate selection of duty cycle was shown to increase the deposition rate without the need for active regulation of oxygen flow.<sup>151</sup>



Similar conclusions were drawn in a different set of experiments aiming to deposit optically transparent, high refractive index  $\text{Nb}_2\text{O}_5$  films using R-HiPIMS and R-MPPMS.<sup>119</sup> The hysteresis-free system allowed researchers to use simple flow control to find the desired working point without the need for fast and sophisticated feedback loops. However, as mentioned before, this conclusion may not be applicable to large, industry-size systems due to the relative greater role of the film as a pump.

A different but related approach was recently introduced<sup>152</sup> based on the observation that poisoning the target changes the current wave form (see Figs. 26 and 27). By real-time monitoring of the waveform one can provide the input data for a feedback loop that automatically regulates the pulse *frequency*, and thereby the duty cycle and average sputtering power, to maintain a constant peak discharge current. In contrast to previous approaches, the flow of reactive gas is kept constant. Here, the “film pump” or reactive gas *consumption* is regulated via the discharge power, rather than by the *supply* flow of reactive gas. Fig. 37 illustrates the equivalence of regulation via reactive gas flow and pulse frequency (i.e. duty cycle or average power). The figure also shows that this is demonstrated for short-pulse HiPIMS, and it remains to be investigated and utilized, if possible, for longer pulses.

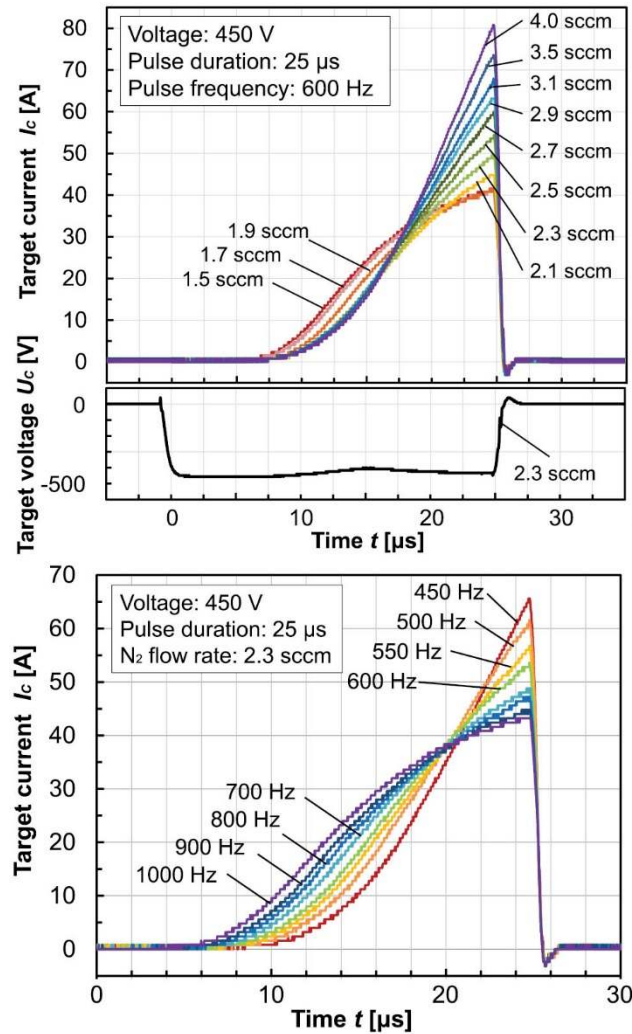




FIG. 37. Equivalence of reactive gas flow and pulse frequency (i.e. affecting average power, duty cycle and reactive gas consumption), regulation of the poisoning state of the target. This offers process control for short-pulse R-HiPIMS via the pulse frequency (consumption) at constant reactive gas flow (Reprint of Figs. 1 and 3 from ref.<sup>152</sup>, with permission from IOP Publishing Ltd).

This concept of frequency control of the degree of poisoning has been applied to control the nitrogen content in zinc oxynitride film.<sup>153</sup> This is an elegant way to tune the optical bandgap of such films.

Process control can be done with any variable or signal that clearly and monotonously depend on the poisoning state of the target. Often optical emissions spectroscopy is used, looking at the intensity of suitable spectral lines,<sup>154,155</sup> or a signal from an ion-collecting probe could be used.<sup>156</sup> For more details the reader is referred to a recent review<sup>157</sup> of HiPIMS and R-HiPIMS plasma diagnostics.

Using parametric modeling, Kozák and Vlček<sup>63</sup> quantified how the compound layer on the target could be reduced yet a stoichiometric compound layer on the substrate is maintained. The direction of injecting the reactive gas flow was recognized as a critical detail and thus explored experimentally (Fig. 38).

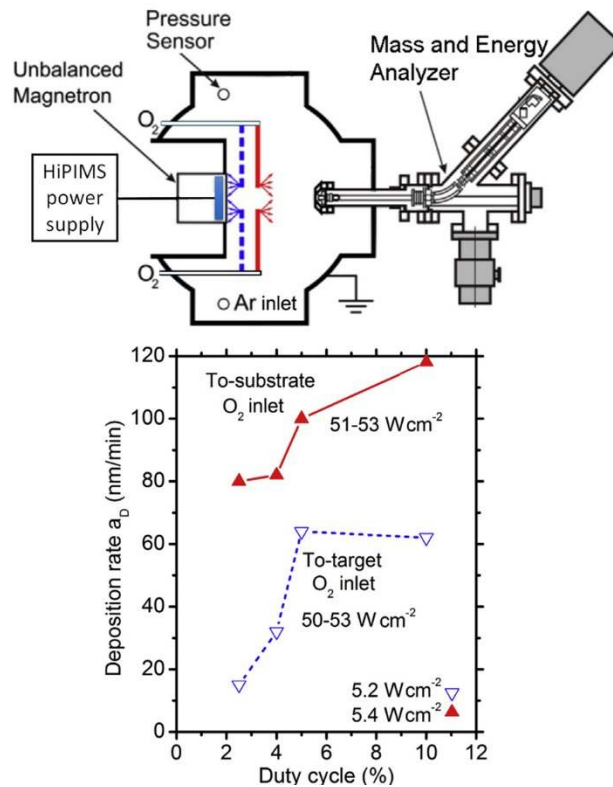


FIG. 38. Effect of the direction of  $O_2$ -flow injection: injection towards the substrate (in red) leads to reduced target poisoning compared to injection toward the target (in blue), followed by a distinctly different deposition rate; the experiment included flux measurements, and therefore a mass and energy analyzer is shown at the location of the substrate (Reprint of Figs. 1 and 5 from ref.<sup>158</sup>, with permission from Elsevier).

#### D. A table compiling some studies of R-HiPIMS

Many effects are material-specific since not just kinetic but material-specific thermodynamic driving forces determine the microstructure and properties of thin films and coatings. Therefore, it makes sense to structure discoveries in R-HiPIMS in table form (Table 1). In many cases, R-HiPIMS is compared with other forms of magnetron sputtering. Researchers generally found a reduction of the deposition rate when the target was poisoned, which is well known from conventional reactive magnetron sputtering, a densification of films caused by ion bombardment, the formation of amorphous or polycrystalline films depending on the material involved and on whether low or high substrate temperature was used, and the possibility to influence phase and texture of polycrystalline film. Some material systems, such as metastable TiAlN are of special importance and therefore have been reviewed elsewhere.<sup>159</sup> Here only selected works and very brief summaries are provided.

**Table 1.** Some studies of R-HiPIMS grouped by coating material systems

Material system	Focus of the Study, Comments	Ref.
Binary transition metal nitrides		
TiN	R-HiPIMS delivers fluxes of target material that is 50% ionized; sufficiently energetic that process gas is dissociated and ionized to a degree that more atomic than molecular ions arrive at substrate.	160
TiN	R-HiPIMS is combined with unbalanced MS (UBMS) in order to get ion assistance with the high rate that UBMS delivers; R-HiPIMS with bias up to -75 V can change the microstructure and texture from strong (111) to random to (200).	161
TiN	Demonstration of fully dense, non-faceted 111-textured TiN by R-HiPIMS grown in the absence of substrate heating and bias	162
TiN	A study of morphology for $T$ from 45°C to 600°C: R-HiPIMS films are smoother than dcMS films; [200] grain size increases with $T$ , whereas the size of the [111] grains decreases to a minimum at 400°C; [200] grains are smaller than [111] grains for all $T$ and smaller for R-HiPIMS compared to R-dcMS.	163
TiN	R-HiPIMS and R-dcMS study of the effect of the incident angle on film microstructure and properties; the finding is that the R-HiPIMS films are less angle-dependent in all aspects (density, morphology, grain size, etc.) than the R-dcMS films.	164
ultrathin TiN	Deposition on MgO(111) substrates using a metal versus ceramic mask resulted in epitaxial versus textured films, respectively. This result is interpreted as due to charge-up of the ceramic holder followed by stronger ion bombardment from the HiPIMS plasma.	165
CrN	Compared HiPIMS and UBMS: Compound formation and removal at the target surface was dynamic and hysteresis was narrowed in HiPIMS.	147

CrN	Early demonstration of high quality CrN by HiPIMS including interface engineering utilizing the high degree of ionization of sputtered Cr.	107,110
CrN <sub>x</sub>	CrN <sub>x</sub> ( $0 \leq x \leq 0.91$ ) by R-HiPIMS and dcMS at the same average power; R-HiPIMS deposition rate was less than dcMS rate, though rate reduction by target poisoning was similar. Film microstructure distinctly different: R-HiPIMS led to a disruption of the grain growth and renucleation, column-free films with nano-sized grains; superior nanoindentation properties	166
CrN <sub>x</sub>	A study of microstructure and composition of CrN <sub>x</sub> ( $0 \leq x \leq 1$ ) films with process parameters N <sub>2</sub> /Ar gas ratio, substrate bias, pulsing frequency, and energy per pulse. Results include finding column-less films with bias-depending CrN and hexagonal $\beta$ -Cr <sub>2</sub> N phases.	167
CrN	Deposition by the MPPMS approach, and a study of bias effects. With increasingly negative substrate bias: grain refinement and an increase in hardness; increase in the Cr/N ratio; preferred (311) texture appears in the range from -50 V to -100 V; the residual compressive stress had a maximum at -100 V; formation of hexagonal Cr <sub>2</sub> N at -150 V, decrease of wear resistance when bias exceeded -150 V.	168
CrN	Using DOMS, study of lattice parameter, preferred orientation; change from columnar growth to a featureless films upon increasing peak power at 0.3 and 0.7 Pa; hardness increased from 21–22 GPa to 28–29 GPa.	169
CrN	Adding Kr to Ar gas: at constant power, the current rise is impeded, as explained by a reduced efficiency of Kr to generate secondary electrons	170
CrN <sub>x</sub>	Use optical emission intensity of Cr I 358 nm to establish a feedback to N <sub>2</sub> flow, highest hardness (29 GPa) and elastic modulus (357 GPa) when operating at a controlled point in the transition region	155
CrN and Cr <sub>2</sub> N	Using R-MPPMS, very thick Cr <sub>2</sub> N and CrN coatings (up to 55 $\mu$ m) were deposited on AISI 440C steel and cemented carbide substrates in a closed field UBMS system. High deposition rates of 15 and 10 $\mu$ m/h have been achieved.	137
ZrN	Demonstrate dense, smooth films by HiPIMS in combination with UBMS, a study of parameters incl. bias leads to optimization of hardness, scratch and corrosion resistances.	171,172
ZrN	Al/TiN/ZrN/ZrO <sub>2</sub> /p-Si metal-insulator-semiconductor structures; epitaxial crystallization of a high-k ZrO <sub>2</sub> thin-film was induced by R-dcMS or R-HiPIMS, with subsequent deposition of a ZrN capping layer; the R-HiPIMS-deposited ZrN samples had more favorable physicochemical and capacitance-voltage characteristics	173
Fe-N	R-HiPIMS deposited Fe-N thin films show improved soft magnetic properties (compared to dcMS films) and likely to possess globular nanocrystalline microstructure; results interpreted in light of strong rarefaction of R-HiPIMS	174
TaN <sub>x</sub>	Using R-MPPMS, and varying the N <sub>2</sub> to Ar flow ratios, the focus was on synthesizing and characterizing the films obtained. Films grown at 0.25 N <sub>2</sub> /Ar flow ratio exhibit the highest corrosion resistance, lowest porosity, characterized by a columnar-free microstructure.	175

AlN	Process comparison of reactive pulsed-dcMS and R-HiPIMS; a partially poisoned aluminum target will lead to the deposition of stoichiometric hcp-AlN thin films via HiPIMS, having a higher hardness (18 GPa) compared to the pulsed-dcMS film (8 GPa).	176
AlN	Using a Design-of-Experiment approach (a.k.a. Taguchi method), process parameters were systematically varied to find that the substrate bias is most influential on hardness (max. 25 GPa), and the duty cycle on transmittance (max. 83%).	177
AlN	Comparison of R-dcMS and R-HiPIMS: XRD always showed oriented films with rocking curves of 1° FWHM, Raman spectroscopy revealed higher residual stress relaxation in the AlN epilayers grown by R-HiPIMS.	178
AlN	Using DOMS, highly <0001> c-axis orientated films were deposited on (100) Si without substrate heating; increase in the nominal peak current density to 0.53 A cm <sup>-2</sup> improved the <0001> orientation; further current increase had a limited effect on texture development.	179
GaN	Interesting since sputtering was done with a liquid Ga target, however, the peak current was less than 1 A, and peak power less than 1 kW, hardly qualifying to be HiPIMS, as claimed by authors. GaN films on sapphire consisted predominantly of compressively stressed domains surrounded by disk-shaped, almost fully relaxed domains.	180
SiN <sub>x</sub>	A study of the effects of different N <sub>2</sub> /Ar flow ratios between 0 and 0.3, pulse frequencies, target power settings, and substrate temperatures on the discharge and the N-content of the films. The species present during R-HiPIMS increase films density, residual stresses, and hardness.	181
Ternary transition metal nitrides, nanocomposites, and nitride multilayers		
TiAlN	A study of properties as a function of increasing bias, finding that Al-content in TiAlN coatings decreased due to selective re-sputtering, and the preferred orientation altered from (111) to (200).	182
Ti <sub>1-x</sub> Al <sub>x</sub> N	Using hybrid R-HiPIMS/dcMS co-sputtering, the study looked at non-obvious differences of aluminum versus titanium ion bombardment: HiPIMS with an Al target (mostly Al <sup>+</sup> bombardment) resulted in alloys with 0.55 ≤ x ≤ 0.60 exhibiting high hardness (30 GPa) and low stress (0.2-0.7 GPa tensile), whereas HiPIMS with a Ti target (mostly Ti <sup>2+</sup> ion bombardment) lead to a cubic (Ti,Al)N and hexagonal AlN two-phase material of low hardness (18-19 GPa), and high compressive stress (up to 2.7 GPa).	183,184
Ti <sub>1-x</sub> Al <sub>x</sub> N with x = 0.61	A model system to probe the effects of metal versus rare-gas ion irradiation, R-HiPIMS for Al, dcMS for Ti in Ar/N <sub>2</sub> ; results show favorable properties when phasing the bias to the metal-rich time within each R-HiPIMS pulse	132
Al <sub>x</sub> Cr <sub>1-x</sub> N (x=0.72-0.75)	A systematic study of the microstructure and mechanical properties as a function of duty cycle and pulse frequency; found great influence of	185

	peak power (plasma and ion density): microstructure changed from coarse to fine columnar, with renucleation of grains between columns.	
TiAlN	A study of the oxidation resistance of R-HiPIMS-deposited hard TiAlN films; findings include: film's top layer is either composed of mixed TiAlO after oxidation at 800 K or of segregated TiO <sub>2</sub> and Al <sub>2</sub> O <sub>3</sub> when oxidized at 293 K	186
(Cr,Al)N	Influence of R-HiPIMS pulse length and the argon/krypton ratio on the deposition process and on (Cr,Al)N coating properties: short pulse lengths and high peak currents lead to an increase of hardness from 25 GPa to 32 GPa, while the R-dcMS coating has hardness of 18 GPa.	187
CrSiN	With a Si content > 6.7 at.%, a nanocomposite structure formed with 5-8 nm Cr(Si)N nanocrystallites embedded in an amorphous Si <sub>3</sub> N <sub>4</sub> matrix. Solid solution strengthening and phase separation are believed to be responsible for the enhanced mechanical properties; maximum hardness = 38 GPa; H/E = 0.096 and H <sup>3</sup> /E* <sup>2</sup> = 0.31 GPa for coatings with Si 6.7 at.%. Well suitable for wear resistant applications, and also exhibiting improved corrosion resistance as compared to AISI 304 stainless steel samples tested in 3.5 wt.% NaCl aqueous solution.	188
ZrNbN	Study of influence of pulse parameters on microstructure and mechanical properties; found a cubic $\delta$ -(Zr,Nb)N mixed crystal phase and a hexagonal $\beta$ -Nb <sub>2</sub> N phase having a nanoscale (4-7 nm) multilayer structure, which is attributed to sequential passing of the substrate through Zr and Nb sputtering zones during deposition.	189
TiAlSiN nanocomposite	Study of the effect of substrate bias: there was a bias feedback on the discharge, leading to higher peak currents; increased bias shifted the preferred orientation from (220) to (200), decreased surface roughness from 14.1 nm to 7.4 nm and the grain size from 10.5 nm to 7.4 nm, changed microstructure from columnar to equiaxial, grain refinement, and increase of hardness from 30 GPa to 42 GPa.	190
(Ti,Al,Si)N nanocomposites	R-HiPIMS had deposition rate up to 1.6 times higher on areas positioned orthogonal to the target compared to R-dcMS coatings; hardness up to 36 GPa for Si content of 9.6 at%.	191
CrAlSiN nanocomposite	An example of combining R-HiPIMS and R-dcMS; synthesized (Cr,Al)N crystallites embedded in an amorphous Si <sub>3</sub> N <sub>4</sub> matrix; Cr <sub>0.23</sub> Al <sub>0.14</sub> Si <sub>0.07</sub> N had highest hardness of 29.4 GPa and much better oxidation resistance (up to 1000°C) compared to CrN	144
Ti <sub>2</sub> AlN (MAX phase after annealing)	Amorphous films were formed at room temperature and at 300°C, which changed into MAX-phase films after vacuum-annealing at 800°C for 1 h.	192
TiAlCN/VCN nanoscale multilayer	Use of a combined R-HiPIMS-UBMS in an industrial batch coater; interface was engineered using vanadium ions from the HiPIMS source, and coating was done in CH <sub>4</sub> -N <sub>2</sub> -Ar mixture, resulting in superior cutting tool performance;	161,193
CrN/TiN multilayer	Using DOMS approach, in combination with pulsed-dcMS, to obtain a multilayer with of high hardness and superior corrosion resistance.	194-196
CrN/NbN multilayer	A study of corrosion protection of 9 wt% Cr steels by 4 $\mu$ m thick CrN/NbN coating having a nano-layer structure with bi-layer thickness	197

	of 2.9 nm; demonstrated excellent tribological properties and oxidation resistance in dry air up to a temperature of 850°C, and tested oxidation at 650°C in 100% steam atmosphere.	
Transition metal oxides		
TiO <sub>2</sub>	Study shows an enhancement of the ionization and dissociation rates of oxygen molecules with increasing peak current, the authors conclude that higher peak current drives a transition from metallic to poisoned regime (while later studies showed the opposite causality, see Fig. 35).	198
TiO <sub>2</sub>	Low temperature deposition of photocatalytically active TiO <sub>2</sub> on 100 µm thick polyethylene terephthalate (PET); rutile to anatase phase ratio is affected by R-HiPIMS parameters.	199
TiO <sub>2</sub>	Films on glass and on floating stainless steel are anatase, while rutile on grounded stainless steel, even at room temperature, showing the effect of ion and electron fluxes; R-HiPIMS enables high refractive index at room temperature.	200
TiO <sub>2</sub>	Using R-HiPIMS ion energies promotes the formation of the rutile phase (high refractive index) for optical applications.	201
TiO <sub>2</sub>	Study of the effect of type of inert gas: mixtures of X/O <sub>2</sub> (where X = Ne, Ar, Kr or Xe) → the power-normalized deposition rates increased with the mass of the inert gas, which has been attributed to a decreased return effect as a result of an increased average absolute target potential during the pulse on-phase.	123
TiO <sub>2</sub>	Using an inverted cylindrical magnetron, researchers find the trend from anatase to rutile is confirmed, showing the role of ionized species for growth; high-resolution TEM shows increase in amorphous domains; the film has a globular structure composed of rutile nano-crystallites embedded in an amorphous matrix.	202
TiO <sub>2</sub>	Study of the plasma impedance and ion flux with a planar ion flux probe showed almost-hysteresis-free transition, suggesting that probe signal could be used for reactive process control.	156
TiO <sub>2</sub>	DOMS version of R-HiPIMS: results in anatase at low power (peak current), gradually shifting to rutile as peak current was increased up to 200 A.	138
TiO <sub>2</sub>	Not a study of films or coatings but observation of spontaneous, repetitive switching between metal and poisoned mode at constant gas flow and constant duty cycle conditions, but variable power depending on the target state	125
RuO <sub>2</sub>	Compare non-reactive to reactive deposition using Ru target: O <sub>2</sub> fraction in the gas mixture strongly affects the pre-ionization phase by electron attachment to O <sub>2</sub> as well as the high current discharge development; transition was found to be free of hysteresis.	154,203
VO <sub>2</sub>	Deposition of dense, stoichiometric, crystalline films of thermochromic VO <sub>2</sub> at lower substrate temperatures (300°C) compared to other approaches.	204

VO <sub>2</sub>	R-HiPIMS films were denser than rfMS films due to ion bombardment, they retained thermochromic properties at least 3 times longer than the RF-sputtered films when aged in a humid environment.	205
VO <sub>2</sub>	A study of the effect of pulsed bias on polycrystalline VO <sub>2</sub> films: phase transition temperature was found to be reduced from 54°C to 31.5°C when negative bias was increased from -50 V to -250 V, films had reduced crystalline size and a change of the preferred crystalline orientation.	206
Al <sub>2</sub> O <sub>3</sub>	Perhaps the first exploratory R-HiPIMS study for the difficult Al-Ar-O <sub>2</sub> system; here reactive gas flow control applied, delivering usable results after target conditioning and when arc suppression is enabled; deposition rate is found much lower than in R-dcMC	207
Al <sub>2</sub> O <sub>3</sub>	An early, much-cited report on the absence of hysteresis in R-HiPIMS; using a small (50 mm diameter) target, high rate deposition of Al <sub>2</sub> O <sub>3</sub> is shown	114
Ta <sub>2</sub> O <sub>5</sub>	A high index optical material; R-HiPIMS showed low surface roughness (~0.2 nm), low residual stress (~ - 50 MPa), high refractive index (2.22 at 550 nm wavelength, comparable with fully dense, thermally-grown films), and high hardness (~7.8 GPa).	208
CrO <sub>x</sub>	Study is focused on emission spectroscopy of R-HiPIMS: in contrast to non-reactive HiPIMS, and R-HiPIMS with nitrogen, there is no metal dominated phase, which can be attributed to the strong compound layer formation.	94
Cr <sub>2</sub> O <sub>3</sub>	DOMS approach to affect the phase: strong crystallinity with (110) preferential orientation, resulting in improved mechanical properties (hardness 35 GPa) and wear resistance (coefficient of dry friction of 0.37, and wear rate of $5.7 \times 10^{-7} \text{ mm}^3 \text{ N}^{-1} \text{ m}^{-1}$ ) compared to dcMS and pulsed-dcMS.	139
ZrO <sub>x</sub>	An early demonstration that R-HiPIMS leads to a stabilization of the deposition process in the transition zone and a suppression of the hysteresis due to higher effective compound erosion rate compared to R-dcMS. Transparent films are obtained at deposition rates up to two times higher than those by R-dcMS.	209
ZrO <sub>x</sub>	A study aiming to increase the bandgap (achieved up to 5.93 eV) and lowering leakage current density (down to 70 nA/cm <sup>2</sup> for 20 nm thick films) by changing the pulse off-time (title of paper), however, duty cycle and peak power were also changed.	210
ZrO <sub>2</sub>	An optimized location of the oxygen gas inlets in front of the target pointing toward the substrate enabled a reduction of arcing and a high deposition rate (120 nm/min) at an averaged target power density of 52 W/cm <sup>2</sup> . At substrate temperature < 120°C, films had high hardness of 16 GPa, a refractive index of 2.19 and a low extinction coefficient of $2 \times 10^{-3}$ at 550 nm. These conditions were related to highest positive ion flux and lowest O <sup>-</sup> flux.	158
Yttria-stabilized zirconia (YSZ)	Zirconia (ZrO <sub>2</sub> ) stabilized by yttria (Y <sub>2</sub> O <sub>3</sub> ) is produced in an industrial batch coater; two metal targets of 50 cm × 8.8 cm, Zr:Y with 86:14 at.%,	211,212

	facing each other; HiPIMS resulted in dense coatings on porous substrates as needed for solid oxide fuel cells.	
NbO <sub>x</sub>	A study of angle-dependent ion fluxes from a HiPIMS magnetron shows asymmetry with respect to the <b>ExB</b> direction, affecting film deposition rate and stoichiometry.	134
Nb <sub>2</sub> O <sub>5</sub>	A study involving R-dcMC, R-HiPIMS, and R-MPPMS, showing that target surface oxides can be effectively sputter-eroded using HiPIMS and MPPMS in O <sub>2</sub> /Ar gas mixtures, thereby a partially oxide-free target is obtained even at high oxygen flow rates, delivering stoichiometric oxide at high deposition rate	119
Fe <sub>2</sub> O <sub>3</sub>	An example of R-HiPIMS with a ferromagnetic target (thickness reduced to 1.8 mm in order to have it magnetically saturated); low-temperature deposition on polycarbonate is possible; annealed films are hematite (hexagonal $\alpha$ -Fe <sub>2</sub> O <sub>3</sub> ) to be used for water splitting in a photoelectrochemical cell	213
ZnO	Comparison of R-HiPIMS and bipolar pulsed magnetron sputtering; R-HiPIMS films are smoother and denser, which is advantageous in Ag-based low-emissivity multilayer stacks	214
a-HfO <sub>2</sub>	Study of the role of pulse length in target poisoning: a smooth transition can be achieved from a poisoned target (short pulses) to a quasi-metallic target (long pulses).	150
a-HfO <sub>2</sub>	Study of the role of duty cycle in target poisoning: a smooth transition can be achieved from poisoned target condition (low duty cycle) to a quasi-metallic target condition (high duty cycle).	151
a-HfO <sub>2</sub>	Use of a pulsed solenoid magnetic field to enhance the deposition rate and affect the poisoning state of the target.	122
HfO <sub>2</sub>	Using a strongly unbalanced magnetron, demonstrated high-rate R-HiPIMS of hard and optically transparent HfO <sub>2</sub> films	215
WO <sub>3</sub>	R-HiPIMS process is assisted by thermal evaporation of the target oxide layer, leading to a deposition rate higher than the corresponding R-dcMS rate	216
WO <sub>3</sub>	R-HiPIMS and other deposition methods to produce crystalline films where the grain orientation can be tuned to optimize photo-electro-chemically activity, e.g. for photocatalytical decomposition and water splitting	217
Transparent Conducting Oxide (TCO)		
SnO <sub>2</sub> :In (ITO)	ITO (indium-tin-oxide) films, deposited at a power-normalized rate of 5.5 nm/(min kW), on unheated float glass and annealed at 650 °C for 10 min, to obtain resistivity < 300 $\mu\Omega$ cm and transmittance > 80%; good chemical and mechanical properties allow the use for low-emissivity coatings on weather-exposed surfaces like automobile windshields.	218
InGaZnO (IGZO)	Ceramic target (In:Ga:Zn:O target having 1:1:1:4 atomic ratio) sputtered in Ar/O <sub>2</sub> to obtain amorphous IGZO thin film on quartz glass at about 40°C–50°C; good TCO properties demonstrated for O <sub>2</sub> /Ar flow ratio > 10%.	219



ZnO:Al (AZO)	Adding a plasma lens between magnetron and substrate to (a) guide plasma to substrate, (b) enhance ionization of gas, (c) attempt to deflect negative ions; AZO deposited at 200°C had 85% transmission and resistivity in the high $10^{-4} \Omega \text{ cm}$ range.	126
ZnO:Al (AZO)	Favorable properties obtained even at low substrate temperature: high transmission, and high conductivity, the authors relate this to controlled operation in the transition mode.	220
ZnO:Al (AZO)	Combining R-dcMS at large oxygen partial pressure with R-HiPIMS to optimize the electrical and optical properties on large surface areas.	221
Oxide multilayers		
SiO <sub>2</sub> /Ta <sub>2</sub> O <sub>5</sub> multilayer	Alternating low-index (SiO <sub>2</sub> ) and high-index (Ta <sub>2</sub> O <sub>5</sub> ) films to produce Bragg reflectors and Fabry-Perot interference filters; pulse optimization to obtain arc-free discharges for R-HiPIMS conditions. Films by R-HiPIMS have higher refractive index, lower surface roughness, denser microstructure, leading to better optical and mechanical properties compared to rfMS-sputtered films.	222
Oxynitrides		
(Cr,Al)N/(Cr,Al)ON	Cr-based oxy-nitride coatings for processing tools for plastics, fabricated by a hybrid of R-dcMS and R-HiPIMS	223
SiO <sub>x</sub> N <sub>y</sub> , with x=0.2-1.3 and y=0.2-0.7	R-HiPIMS on pure Si target in Ar/N <sub>2</sub> O, high average powers result in silicon-rich films, while lower target powers yield SiO <sub>2</sub> -like material due to target poisoning; nitrogen percentage in the films can be controlled by the percentage of N <sub>2</sub> O in the gas; refractive indices at 633 nm ranged between those of SiO <sub>2</sub> and Si <sub>3</sub> N <sub>4</sub> .	224
ZnO <sub>x</sub> N <sub>x</sub>	Short-pulse R-HiPIMS of Zn-Ar/N <sub>2</sub> /O <sub>2</sub> system, with small amounts of O <sub>2</sub> . Variation of the pulse frequency facilitated the fine control of nitrogen content using the smooth transitions between poisoned and metal mode; crystalline films with N-content from 0 to 6.2 at.% and optical band gap from 3.34 to 1.67 eV demonstrated.	153
Hydrides		
δ-ZrH <sub>2</sub>	Comparison of R-dcMS and R-HiPIMS: thorough characterization shows many differences, such as glasslike microstructure for the R-HiPIMS films, columnar for R-dcMS; phase-pure δ-ZrH <sub>2</sub> films by R-HiPIMS exhibit up to 50 times lower wear rate compared to those containing a secondary Zr phase.	225
Chalcopyrite		
Copper indium gallium diselenide (CIGS)	An unusual study where poisoning of the CIG target is controlled by the vapor of selenium (Se) in argon; films lead to about 3% more efficient solar cells compared to R-dcMS films; R-HiPIMS scaling demonstrated with cylindrical magnetrons with an average power up to 7.8 kW.	226
Carbon-containing films		
CF <sub>x</sub>	A large (440 cm <sup>2</sup> ) graphite target sputtered at 400 mPa in mixed Ar/CF <sub>4</sub> and Ar/C <sub>4</sub> F <sub>8</sub> atmospheres, resulting in amorphous carbon fluoride (CF <sub>x</sub> ) films synthesized at 110°C; R-HiPIMS parameters are suitable to control film properties including functionalization of the surface.	227

CN <sub>x</sub>	Deposition of carbon nitride using R-dcMS and R-HiPIMS with different inert gas mixtures (N <sub>2</sub> /Ne, N <sub>2</sub> /Ar, and N <sub>2</sub> /Kr): R-HiPIMS yields approximately ten times higher flux ratios of ions originating from the target to process gas ions than R-dcMS. Films were amorphous or fullerene-like with only a moderate influence by the noble gas type.	228
Hydrogenated DLC	Thick DLC:H thin films by admixing Ne in a R-HiPIMS based Ar/C <sub>2</sub> H <sub>2</sub> discharge; obtained low compressive stresses (0.5 GPa), high hardness (25 GPa), low H-content (11%), and density in the order of 2.2 g/cm <sup>3</sup> . Low hydrogen content indicates H-removal by ion bombardment, affecting other mechanical properties.	124
DLC:Ti	HiPIMS with Ar/C <sub>2</sub> H <sub>2</sub> gas leads to a pulsed CVD approach to deposit Ti-doped, conducting diamond-like carbon (DLC) films; doping done by Ti-sputtering.	229

## VIII. SUPPLEMENTARY MATERIAL

The supplementary material contains the Yamamura and Tawara sputter yield formula and two tables. Table S1 lists parameters for the Yamamura and Tawara formula.<sup>7</sup> Table S2 provides fit parameters to be used in Eq. (4) for given combinations of ion and target materials.

## REFERENCES

- <sup>1</sup> W. R. Grove, "On some anomalous cases of electrical decomposition," *Phil. Mag., Series 4*, **5**, 203 (1853).
- <sup>2</sup> *Sputtering by Particle Bombardment; Vol.*, edited by R. Behrisch and W. Eckstein (Springer, Berlin, 2007).
- <sup>3</sup> M. W. Thompson, "Physical mechanisms of sputtering," *Phys. Rep.* **69**, 335 (1981).
- <sup>4</sup> *Reactive Sputter Deposition; Vol.*, edited by D. Depla and S. Mahieu (Springer, Heidelberg, 2008).
- <sup>5</sup> J. F. Ziegler, J. P. Biersack, and U. Littmark, *The Stopping and Range of Ions in Solids* (Pergamon Press, New York, 1985).
- <sup>6</sup> J. F. Ziegler and J. Biersack, "Monte Carlo code SRIM2013, downloadable from <http://srim.org/>," (2013).
- <sup>7</sup> Y. Yamamura and H. Tawara, "Energy dependence of ion-induced sputtering yields from monatomic solids at normal incidence," *Atomic Data and Nuclear Data Tables* **62**, 149 (1996).
- <sup>8</sup> P. Sigmund, "Theory of sputtering. I. Sputtering yield of amorphous and polycrystalline targets," *Phys. Rev.* **184**, 383 (1969).
- <sup>9</sup> J. Bohdansky, *Nucl. Instrum. Meth. Phys. Res. B* **2**, 587 (1984).
- <sup>10</sup> M. W. Thompson, "The energy spectrum of ejected atoms during the high energy sputtering of gold," *Phil. Mag.* **18**, 377 (1968).
- <sup>11</sup> V. V. Serikov and K. Nanbu, "The analysis of background gas heating in direct current sputtering discharges via particle simulation," *J. Appl. Phys.* **82**, 5948 (1997).
- <sup>12</sup> Y. Kudriavtsev, A. Villegas, A. Godines, and R. Asomoza, "Calculation of the surface binding energy for ion sputtered particles," *Appl. Surf. Sci.* **239**, 273 (2005).
- <sup>13</sup> G. Betz and W. Husinsky, "Modelling of cluster emission from metal surfaces under ion impact," *Phil. Trans. Royal Soc. A: Math. Phys. Eng. Sci.* **362**, 177 (2004).
- <sup>14</sup> A. Anders, "Discharge physics of high power impulse magnetron sputtering," *Surf. Coat. Technol.* **205**, S1 (2011).
- <sup>15</sup> F. F. Chen, *Plasma Physics and Controlled Fusion* (Plenum Press, New York, 1984).
- <sup>16</sup> J. W. Bradley, S. Thompson, and Y. A. Gonzalvo, "Measurement of the plasma potential in a magnetron discharge and the prediction of the electron drift speeds," *Plasma Sources Sci. Technol.* **10**, 490 (2001).
- <sup>17</sup> A. Rauch and A. Anders, "Estimating electron drift velocities in magnetron discharges," *Vacuum* **89**, 53 (2013).

- 18 O. Chapurin and A. Smolyakov, "On the electron drift velocity in plasma devices with  $E \times B$  drift," J. Appl. Phys. **119**, 243306 (2016).
- 19 Q. H. Fan, L. Q. Zhou, and J. J. Gracio, "A cross-corner effect in a rectangular sputtering magnetron," J. Phys. D: Appl. Phys. **36**, 244 (2003).
- 20 J. A. Thornton, "Magnetron sputtering: basic physics and application to cylindrical magnetrons," J. Vac. Sci. Technol. **15**, 171 (1978).
- 21 J. A. Thornton, "Influence of apparatus geometry and deposition conditions on the structure and topography of thick sputtered coatings," J. Vac. Sci. Technol. **11**, 666 (1974).
- 22 B. Window and N. Savvides, "Unbalanced DC magnetrons as sources of high ion fluxes," J. Vacuum Sci. Technol. A **4**, 453 (1986).
- 23 B. Window and N. Savvides, "Charged particle fluxes from planar magnetron sputtering sources," J. Vac. Sci. Technol. A **4**, 196 (1986).
- 24 A. Anders, "A structure zone diagram including plasma-based deposition and ion etching," Thin Solid Films **518**, 4087 (2010).
- 25 A. Anders, P. Ni, and J. Andersson, "Drifting ionization zone in sputtering magnetron discharges at very low currents," IEEE Trans. Plasma Sci. **42**, 2578 (2014).
- 26 J.-P. Boeuf and B. Chaudhury, "Rotating instability in low-temperature magnetized plasmas," Phys. Rev. Lett. **111**, 155005 (2013).
- 27 P. A. Ni, C. Hornschoch, M. Panjan, and A. Anders, "Plasma flares in high power impulse magnetron sputtering," Appl. Phys. Lett. **101**, 224102 (2012).
- 28 J. P. Boeuf, "Tutorial: Physics and modeling of Hall thrusters," J. Appl. Phys. **121**, 011101 (2017).
- 29 B. Szapiro and J. J. Rocca, "Electron emission from glow-discharge cathode materials due to neon and argon ion bombardment," J. Appl. Phys. **65**, 3713 (1989).
- 30 H. Eder, W. Messerschmidt, H. Winter, and F. Aumayr, "Electron emission from clean gold bombardment by slow  $Au^{q+}$  ( $q=1-3$ ) ions," J. Appl. Phys. **87**, 8198 (2000).
- 31 R. A. Baragiola, E. V. Alonso, J. Ferron, and A. Oliva-Florio, "Ion-induced electron emission from clean metals," Surf. Sci. **90**, 240 (1979).
- 32 M. Panjan and A. Anders, "Plasma potential of a moving ionization zone in DC magnetron sputtering," J. Appl. Phys. **121**, in print AIP ID: 021705jap (2017).
- 33 C. Huo, D. Lundin, M. A. Raadu, A. Anders, J. T. Gudmundsson, and N. Brenning, "On sheath energization and Ohmic heating in sputtering magnetrons," Plasma Sources Sci. Technol. **22**, 045005 (2013).

- <sup>34</sup> A. Anders, "Localized heating of electrons in ionization zones: Going beyond the Penning-Thornton paradigm in magnetron sputtering," Appl. Phys. Lett. **105**, 244104 (2014).
- <sup>35</sup> N. Brenning, J. T. Gudmundsson, D. Lundin, T. Minea, M. A. Raadu, and U. Helmersson, "The role of Ohmic heating in dc magnetron sputtering," Plasma Sources Sci. Technol. **25**, 065024 (2016).
- <sup>36</sup> G. Janes and R. Lowder, "Anomalous electron diffusion and ion acceleration in a low-density plasma," Phys. Fluids **9**, 1115 (1966).
- <sup>37</sup> A. Kozyrev, N. Sochugov, K. Oskomov, A. Zakharov, and A. Odivanova, "Optical studies of plasma inhomogeneities in a high-current pulsed magnetron discharge," Plasma Physics Reports **37**, 621 (2011).
- <sup>38</sup> A. Anders, P. Ni, and A. Rauch, "Drifting localization of ionization runaway: Unraveling the nature of anomalous transport in high power impulse magnetron sputtering," J. Appl. Phys. **111**, 053304 (2012).
- <sup>39</sup> A. P. Ehasarian, A. Hecimovic, T. de los Arcos, R. New, V. Schulz-von der Gathen, M. Böke, and J. Winter, "High power impulse magnetron sputtering discharges: instabilities and plasma self-organization," Appl. Phys. Lett. **100**, 114101 (2012).
- <sup>40</sup> A. Hecimovic, V. Schulz-von der Gathen, M. Böke, A. von Keudell, and J. Winter, "Spoke transitions in HiPIMS discharges," Plasma Sources Sci. Technol. **24**, 045005 (2015).
- <sup>41</sup> A. Hecimovic, C. Maszl, V. Schulz-von der Gathen, M. Böke, and A. von Keudell, "Spoke rotation reversal in magnetron discharges of aluminium, chromium and titanium," Plasma Sources Sci. Technol. **25**, 035001 (2016).
- <sup>42</sup> M. Panjan, S. Loquai, J. E. Klemberg-Sapieha, and L. Martinu, "Non-uniform plasma distribution in dc magnetron sputtering: origin, shape and structuring of spokes," Plasma Sources Sci. Technol. **24**, 065010 (2015).
- <sup>43</sup> A. V. Phelps, "Compilation of electron cross sections, available from [http://jila.colorado.edu/~avp/collision\\_data/electronneutral/ELECTRON.TXT](http://jila.colorado.edu/~avp/collision_data/electronneutral/ELECTRON.TXT)," (2005).
- <sup>44</sup> L. M. Biberman, V. S. Vorobev, and I. T. Yakubov, *Kinetics of Nonequilibrium Low-Temperature Plasma (in Russ.)* (Nauka, Moscow, 1982).
- <sup>45</sup> Y. P. Raizer, *Gas Discharge Physics* (Springer, Berlin, 1991).
- <sup>46</sup> S. M. Rossnagel, "Gas density reduction effects in magnetrons," J. Vac. Sci. Technol. A **6**, 19 (1988).
- <sup>47</sup> W. D. Hoffman, "A sputtering wind," J. Vac. Sci. Technol. A **3**, 561 (1985).

- 48 D. Güttler, B. Abendroth, R. Grötzschel, W. Möller, and D. Depla, "Mechanisms of target poisoning during magnetron sputtering as investigated by real-time in situ analysis and collisional computer simulation," *Appl. Phys. Lett.* **85**, 6134 (2004).
- 49 D. Depla and R. De Gryse, "Target poisoning during reactive magnetron sputtering: Part I: the influence of ion implantation," *Surf. Coat. Technol.* **183**, 184 (2004).
- 50 D. Depla and R. De Gryse, "Target poisoning during reactive magnetron sputtering: Part II: the influence of chemisorption and gettering," *Surf. Coat. Technol.* **183**, 190 (2004).
- 51 D. Depla, S. Mahieu, and R. D. Gryse, in *Reactive Sputter Deposition*, edited by D. Depla and S. Mahieu (2008), p. 153.
- 52 D. Depla, S. Heirwegh, S. Mahieu, and R. D. Gryse, "Towards a more complete model for reactive magnetron sputtering," *J. Phys. D: Appl. Phys.* **40**, 1957 (2007).
- 53 W. Möller, S. Parascandola, T. Telbizova, R. Günzel, and E. Richter, "Surface processes and diffusion mechanisms of ion nitriding of stainless steel and aluminum," *Surf. Coat. Technol.* **136**, 73 (2001).
- 54 D. Güttler, R. Grötzschel, and W. Möller, "Lateral variation of target poisoning during reactive magnetron sputtering," *Appl. Phys. Lett.* **90**, 263502 (2007).
- 55 T. Kubart, O. Kappertz, T. Nyberg, and S. Berg, "Dynamic behaviour of the reactive sputtering process," *Thin Solid Films* **515**, 421 (2006).
- 56 D. Depla, S. Mahieu, and J. E. Greene, in *Handbook of Deposition Technologies for Films and Coatings*, 3rd. ed., edited by P. M. Martin (William Andrew, 2010), p. 253.
- 57 D. Depla, S. Mahieu, and R. De Gryse, "Magnetron sputter deposition: Linking discharge voltage with target properties," *Thin Solid Films* **517**, 2825 (2009).
- 58 W. D. Sproul, D. J. Christie, and D. C. Carter, "Control of reactive sputtering processes," *Thin Solid Films* **491**, 1 (2005).
- 59 S. Berg, H. O. Blom, T. Larsson, and C. Nender, "Modeling of reactive sputtering of compound materials," *J. Vac. Sci. Technol. A* **5**, 202 (1987).
- 60 F. G. Cougnon, K. Strijckmans, R. Schelfhout, and D. Depla, "Hysteresis behavior during facing target magnetron sputtering," *Surf. Coat. Technol.* **294**, 215 (2016).
- 61 K. Strijckmans, W. P. Leroy, R. De Gryse, and D. Depla, "Modeling reactive magnetron sputtering: Fixing the parameter set," *Surf. Coat. Technol.* **206**, 3666 (2012).
- 62 D. J. Christie, "Target material pathways model for high power pulsed magnetron sputtering," *J. Vac. Sci. Technol. A* **23**, 330 (2005).

- 63 T. Kozák and J. Vlček, "A parametric model for reactive high-power impulse magnetron sputtering of films," J. Phys. D: Appl. Phys. **49**, 055202 (2016).
- 64 J. Musil and P. Baroch, "Discharge in dual magnetron sputtering system," IEEE Trans. Plasma Sci. **33**, 338 (2005).
- 65 V. Kirchhoff, T. Kopte, T. Winkler, M. Schulze, and P. Wiedemuth, "Dual magnetron sputtering (DMS) system with sine-wave power supply for large-area coating," Surf. Coat. Technol. **98**, 828 (1998).
- 66 A. Belkind, Z. Zhao, G. Carter, McDonough, G. Roche, and R. Scholl, "Reactive sputtering using a dual-anode magnetron system," 44th Annual Technical Conference Proceedings, Philadelphia, 2001 (Society of Vacuum Coaters).
- 67 G. Teschner, F. Milde, and J. Strümpfel, "Dual anode magnetron sputtering," 50th Annual Technical Conference Proceedings, 2007 (Society of Vacuum Coaters).
- 68 S. Mráz and J. M. Schneider, "Energy distribution of  $O^-$  ions during reactive magnetron sputtering," Appl. Phys. Lett. **89**, 051502 (2006).
- 69 T. Jäger, Y. E. Romanyuk, A. N. Tiwari, and A. Anders, "Controlling ion fluxes during reactive sputter-deposition of  $SnO_2:F$ ," J. Appl. Phys. **116**, 033301 (2014).
- 70 T. Welzel and K. Ellmer, "Negative oxygen ion formation in reactive magnetron sputtering processes for transparent conductive oxides," J. Vac. Sci. Technol. A **30**, 061306 (2012).
- 71 A. Anders, "Physics of arcing, and implications to sputter deposition," Thin Solid Films **502**, 22 (2006).
- 72 A. Anders, *Cathodic Arcs: From Fractal Spots to Energetic Condensation* (Springer, New York, 2008).
- 73 D. Drescher, J. Koskinen, H.-J. Scheibe, and A. Mensch, "A model for particle growth in arc deposited amorphous carbon films," Diamond Rel. Mat. **7**, 1375 (1998).
- 74 A. Gilewicz, P. Chmielewska, D. Murzynski, E. Dobruchowska, and B. Warcholinski, "Corrosion resistance of CrN and CrCN/CrN coatings deposited using cathodic arc evaporation in Ringer's and Hank's solutions," Surf. Coat. Technol. **299**, 7 (2016).
- 75 H. W. Wang, M. M. Stack, S. B. Lyon, P. Hovsepian, and W. D. Munz, "Wear associated with growth defects in combined cathodic arc/unbalanced magnetron sputtered CrN/NbN superlattice coatings during erosion in alkaline slurry," Surf. Coat. Technol. **135**, 82 (2000).
- 76 P. Panjan, P. Gselman, D. Kek-Merl, M. Čekada, M. Panjan, G. Dražić, T. Bončina, and F. Zupanič, "Growth defect density in PVD hard coatings prepared by different deposition techniques," Surf. Coat. Technol. **237**, 349 (2013).

- 77 S. Schiller, K. Goedicke, J. Reschke, V. Kirchhoff, S. Schneider, and F. Milde, "Pulsed magnetron sputter technology " Surf. Coat. Technol. **61**, 331 (1993).
- 78 A. Belkind, A. Freilich, and R. Scholl, "Electrical dynamics of pulsed plasmas," 41st Annual Tech. Conf. Society of Vacuum Coaters, Boston, 1998 (Society of Vacuum Coaters), p. 321.
- 79 A. Hemberg, S. Konstantinidis, F. Renaux, J. P. Dauchot, and R. Snyders, "Ion flux-film structure relationship during magnetron sputtering of WO<sub>3</sub>," Eur. Phys. J. Appl. Phys. **56**, 24016 (2011).
- 80 N. Hosokawa, T. Tsukada, and T. Misumi, "Self-sputtering phenomena in high-rate coaxial cylindrical magnetron sputtering," J. Vac. Sci. Technol. **14**, 143 (1977).
- 81 V. Kouznetsov, K. Macak, J. M. Schneider, U. Helmersson, and I. Petrov, "A novel pulsed magnetron sputter technique utilizing very high target power densities," Surf. Coat. Technol. **122**, 290 (1999).
- 82 A. Anders, J. Andersson, and A. Ehasarian, "Erratum: ``High power impulse magnetron sputtering: Current-voltage-time characteristics indicate the onset of sustained self-sputtering" [J. Appl. Phys. **102**, 113303 (2007)]," J. Appl. Phys. **103**, 039901 (2008).
- 83 A. Anders, J. Andersson, and A. Ehasarian, "High power impulse magnetron sputtering: Current-voltage-time characteristics indicate the onset of sustained self-sputtering," J. Appl. Phys. **102**, 113303 (2007).
- 84 A. Anders, J. Čapek, M. Hála, and L. Martinu, "The 'recycling trap': A generalized explanation of discharge runaway in high power impulse magnetron sputtering," J. Phys. D: Appl. Phys. **45**, 012003 (2012).
- 85 S. Ashida, C. Lee, and M. A. Lieberman, "Spatially averaged (global) model of time modulated high density argon plasmas," J. Vac. Sci. Technol. A **13**, 2498 (1995).
- 86 C. Huo, D. Lundin, M. A. Raadu, A. Anders, J. T. Gudmundsson, and N. Brenning, "On the road to self-sputtering in high power impulse magnetron sputtering: particle balance and discharge characteristics," Plasma Sources Sci. Technol. **23**, 025017 (2014).
- 87 M. A. Raadu, I. Axnäs, J. T. Gudmundsson, C. Huo, and N. Brenning, "An ionization region model for high-power impulse magnetron sputtering discharges," Plasma Sources Sci. Technol. **20**, 065007 (2011).
- 88 C. Huo, M. A. Raadu, D. Lundin, J. T. Gudmundsson, A. Anders, and N. Brenning, "Gas rarefaction and the time evolution of long high-power impulse magnetron sputtering pulses," Plasma Sources Sci. Technol. **21**, 045004 (2012).
- 89 J. Andersson, P. Ni, and A. Anders, "Smoothing of discharge inhomogeneities at high currents in gasless high power impulse magnetron sputtering," IEEE Trans. Plasma Sci. **42**, 2856 (2014).



- <sup>90</sup> A. von Keudell, A. Hecimovic, and C. Maszl, "Control of high power pulsed magnetron discharge by monitoring the current voltage characteristics," *Contrib. Plasma Phys.* **56**, 918 (2016).
- <sup>91</sup> A. Anders, "Self-organization and self-limitation in high power impulse magnetron sputtering," *Appl. Phys. Lett.* **100**, 224104 (2012).
- <sup>92</sup> Y. Yang, J. Liu, L. Liu, and A. Anders, "Propagation direction reversal of ionization zones in the transition between high and low current magnetron sputtering," *Appl. Phys. Lett.* **105**, 254101 (2014).
- <sup>93</sup> M. Hála, O. Zabeida, B. Baloukas, J. E. Klemberg-Sapieha, and L. Martinu, "Time- and species-resolved plasma imaging as a new diagnostic approach for HiPIMS discharge characterization," *IEEE Trans. Plasma Sci.* **38**, 3035 (2010).
- <sup>94</sup> M. Hála, O. Zabeida, J. E. Klemberg-Sapieha, and L. Martinu, "Dynamics of HiPIMS discharge operated in oxygen," *IEEE Trans. Plasma Sci.* **39**, 2582 (2011).
- <sup>95</sup> J. Andersson, P. Ni, and A. Anders, "Spectroscopic imaging of self-organization in high power impulse magnetron sputtering plasmas," *Appl. Phys. Lett.* **103**, 054104 (2013).
- <sup>96</sup> A. Ehasarian, in *Plasma Surface Engineering Research and its Practical Applications*, edited by R. Wei (Research Signpost, Kerala, India, 2008), p. 35.
- <sup>97</sup> J. Bohlmark, M. Ostbye, M. Lattemann, H. Ljungcrantz, T. Rosell, and U. Helmersson, "Guiding the deposition flux in an ionized magnetron discharge," *Thin Solid Films* **515**, 1928 (2006).
- <sup>98</sup> I.-L. Velicu, V. Tiron, C. Porosnicu, I. Burducea, N. Lupu, G. Stoian, G. Popa, and D. Munteanu, "Enhanced properties of tungsten thin films deposited with a novel HiPIMS approach," *Appl. Surf. Sci.* **accepted**, DOI 10.1016/j.apsusc.2017.01.067 (2017).
- <sup>99</sup> Y. Yang, K. Tanaka, J. Liu, and A. Anders, "Ion energies in high power impulse magnetron sputtering with and without localized ionization zones," *Appl. Phys. Lett.* **106**, 124102 (2015).
- <sup>100</sup> M. Panjan, R. Franz, and A. Anders, "Azimuthally asymmetric particle fluxes in sputtering magnetrons, and their amplification by ionization zones in high power impulse magnetron sputtering," *Plasma Sources Sci. Technol.* **23**, 025007 (2014).
- <sup>101</sup> C. Li, X. Tian, C. Gong, and J. Xu, "The improvement of high power impulse magnetron sputtering performance by an external unbalanced magnetic field," *Vacuum* **133**, 98 (2016).
- <sup>102</sup> J. Vlček, P. Kudláček, K. Burcalová, and J. Musil, "High-power pulsed sputtering using a magnetron with enhanced plasma confinement," *J. Vac. Sci. Technol. A* **25**, 42 (2007).

- <sup>103</sup> J. Čapek, M. Hála, O. Zabeida, J. E. Klemberg-Sapieha, and L. Martinu, "Steady state discharge optimization in high-power impulse magnetron sputtering through the control of the magnetic field," *J. Appl. Phys.* **111**, 023301 (2012).
- <sup>104</sup> P. Raman, I. A. Shchelkanov, J. McLain, and D. N. Ruzic, "High power pulsed magnetron sputtering: A method to increase deposition rate," *J. Vac. Sci. Technol. A* **33**, 031304 (2015).
- <sup>105</sup> D. Horwat and A. Anders, "Compression and strong rarefaction in high power impulse magnetron sputtering discharges," *J. Appl. Phys.* **108**, 123306 (2010).
- <sup>106</sup> M. Palmucci, N. Britun, S. Konstantinidis, and R. Snyders, "Rarefaction windows in a high-power impulse magnetron sputtering plasma," *J. Appl. Phys.* **114**, 113302 (2013).
- <sup>107</sup> A. P. Ehasarian, W.-D. Münz, L. Hultman, and U. Helmersson, "CrN deposition by reactive high power density pulsed magnetron sputtering," 45th Ann. Techn. Conf. Proc., 2002 (Society of Vacuum Coaters), p. 328.
- <sup>108</sup> M. Lattemann, A. P. Ehasarian, J. Bohlmark, P. A. O. Persson, and U. Helmersson, "Investigation of high power impulse magnetron sputtering pretreated interfaces for adhesion enhancement of hard coatings on steel," *Surf. Coat. Technol.* **200**, 6495 (2006).
- <sup>109</sup> W.-D. Münz, D. Schulze, and F. J. M. Hauzer, "A new method for hard coatings - ABS (arc bond sputtering)," *Surf. Coat. Technol.* **50**, 169 (1992).
- <sup>110</sup> A. P. Ehasarian, W. D. Munz, L. Hultman, U. Helmersson, and I. Petrov, "High power pulsed magnetron sputtered CrNx films," *Surf. Coat. Technol.* **163-164**, 267 (2003).
- <sup>111</sup> J. T. Gudmundsson, D. Lundin, N. Brenning, M. A. Raadu, C. Huo, and T. M. Minea, "An ionization region model of the reactive Ar/O<sub>2</sub> high power impulse magnetron sputtering discharge," *Plasma Sources Sci. Technol.* **25**, 065004 (2016).
- <sup>112</sup> F. Magnus, O. B. Sveinsson, S. Olafsson, and J. T. Gudmundsson, "Current-voltage-time characteristics of the reactive Ar/N<sub>2</sub> high power impulse magnetron sputtering discharge," *J. Appl. Phys.* **110**, 083306 (2011).
- <sup>113</sup> F. Magnus, T. K. Tryggvason, S. Olafsson, and J. T. Gudmundsson, "Current-voltage-time characteristics of the reactive Ar/O<sub>2</sub> high power impulse magnetron sputtering discharge," *J. Vac. Sci. Technol. A* **30**, 050601 (2012).
- <sup>114</sup> E. Wallin and U. Helmersson, "Hysteresis-free reactive high power impulse magnetron sputtering," *Thin Solid Films* **516**, 6398 (2008).
- <sup>115</sup> M. Audronis and V. Bellido-Gonzalez, "Hysteresis behaviour of reactive high power impulse magnetron sputtering," *Thin Solid Films* **518**, 1962 (2010).

- <sup>116</sup> T. Kubart, M. Aiempanakit, J. Andersson, T. Nyberg, S. Berg, and U. Helmersson, "Studies of hysteresis effect in reactive HiPIMS deposition of oxides," *Surf. Coat. Technol.* **205, Supplement 2**, S303 (2011).
- <sup>117</sup> W. Möller, W. Eckstein, and J. P. Biersack, "TRIDYN-binary collision simulation of atomic collisions and dynamic composition changes in solids," *Comp. Phys. Comm.* **51**, 355 (1988).
- <sup>118</sup> T. Kubart and J. Andersson, "Modelling of target effects in reactive HiPIMS," *IOP Conf. Series: Materials Science and Engineering* **39**, 012008 (2012).
- <sup>119</sup> M. Hála, J. Čapek, O. Zabeida, J. E. Klemberg-Sapieha, and L. Martinu, "Hysteresis-free deposition of niobium oxide films by HiPIMS using different pulse management strategies," *J. Phys. D: Appl. Phys.* **45**, 055204 (2012).
- <sup>120</sup> M. Hala, N. Viau, O. Zabeida, J. E. Klemberg-Sapieha, and L. Martinu, "Dynamics of reactive high-power impulse magnetron sputtering discharge studied by time- and space-resolved optical emission spectroscopy and fast imaging," *J. Appl. Phys.* **107**, 043305 (2010).
- <sup>121</sup> S. Loquai, O. Zabeida, J. E. Klemberg-Sapieha, and L. Martinu, "Flash post-discharge emission in a reactive HiPIMS process," *Appl. Phys. Lett.* **109**, 114101 (2016).
- <sup>122</sup> R. Ganesan, B. Treverrow, P. Denniss, D. G. McCulloch, D. R. McKenzie, and M. M. M. Bilek, "Pulsed external magnetic fields increase the deposition rate in reactive HiPIMS while preserving stoichiometry: An application to amorphous  $\text{HfO}_2$ ," *J. Appl. Phys.* **120**, 103301 (2016).
- <sup>123</sup> M. Bowes and J. W. Bradley, "Inert gas effects on the deposition rate of  $\text{TiO}_2$  during reactive HiPIMS," *Surf. Coat. Technol.* **250**, 2 (2014).
- <sup>124</sup> A. Aijaz, S. Lourcing, D. Lundin, T. Kubart, J. Jensen, K. Sarakinos, and U. Helmersson, "Synthesis of hydrogenated diamondlike carbon thin films using neon–acetylene based high power impulse magnetron sputtering discharges," *J. Vac. Sci. Technol. A* **34**, 061504 (2016).
- <sup>125</sup> S. Shayestehaminzadeh, U. B. Arnalds, R. L. Magnusson, and S. Olafsson, "Observation of a periodic runaway in the reactive Ar/O<sub>2</sub> high power impulse magnetron sputtering discharge," *AIP Advances* **5**, 117240 (2015).
- <sup>126</sup> A. Anders and J. Brown, "A plasma lens for magnetron sputtering," *IEEE Trans. Plasma Sci.* **39**, 2528 (2011).
- <sup>127</sup> A. Anders, US Patent No. 8,574,410 B2, 2013.
- <sup>128</sup> A. Anders, US Patent No. 9,455,057 B2, 2016.
- <sup>129</sup> A. Anders, "Metal plasma immersion ion implantation and deposition: a review," *Surf. Coat. Technol.* **93**, 158 (1997).

- <sup>130</sup> I. G. Brown, X. Godechot, and K. M. Yu, "Novel metal ion surface modification technique," Appl. Phys. Lett. **58**, 1392 (1991).
- <sup>131</sup> A. Anders, N. Pasaja, and S. Sansongsiri, "Filtered cathodic arc deposition with ion-species-selective bias," Rev. Sci. Instrum. **78**, 063901 (2007).
- <sup>132</sup> G. Greczynski, J. Lu, J. Jensen, I. Petrov, J. E. Greene, S. Bolz, W. Kolker, C. Schiffers, O. Lemmer, and L. Hultman, "Metal versus rare-gas ion irradiation during  $\text{Ti}_{1-x}\text{Al}_x\text{N}$  film growth by hybrid high power pulsed magnetron/dc magnetron co-sputtering using synchronized pulsed substrate bias," J. Vac. Sci. Technol. A **30**, 061504 (2012).
- <sup>133</sup> G. Greczynski and L. Hultman, "Time and energy resolved ion mass spectroscopy studies of the ion flux during high power pulsed magnetron sputtering of Cr in Ar and Ar/ $\text{N}_2$  atmospheres," Vacuum **84**, 1159 (2010).
- <sup>134</sup> R. Franz, C. Clavero, J. Kolbeck, and A. Anders, "Influence of ionisation zone motion in high power impulse magnetron sputtering on angular ion flux and  $\text{NbO}_x$  film growth," Plasma Sources Sci. Technol. **25**, 015022 (2016).
- <sup>135</sup> J. Lin, J. J. Moore, W. D. Sproul, B. Mishra, J. A. Rees, Z. Wu, R. Chistyakov, and B. Abraham, "Ion energy and mass distributions of the plasma during modulated pulse power magnetron sputtering," Surf. Coat. Technol. **203**, 3676 (2009).
- <sup>136</sup> F. Papa, H. Gerdes, R. Bandorf, A. P. Ehasarian, I. Kolev, G. Braeuer, R. Tietema, and T. Krug, "Deposition rate characteristics for steady state high power impulse magnetron sputtering (HIPIMS) discharges generated with a modulated pulsed power (MPP) generator," Thin Solid Films **520**, 1559 (2011).
- <sup>137</sup> J. Lin, W. D. Sproul, J. J. Moore, S. Lee, and S. Myers, "High rate deposition of thick CrN and  $\text{Cr}_2\text{N}$  coatings using modulated pulse power (MPP) magnetron sputtering," Surf. Coat. Technol. **205**, 3226 (2011).
- <sup>138</sup> J. Lin, B. Wang, W. D. Sproul, Y. Ou, and I. Dahan, "Anatase and rutile  $\text{TiO}_2$  films deposited by arc-free deep oscillation magnetron sputtering," J. Phys. D: Appl. Phys. **46**, 084008 (2013).
- <sup>139</sup> J. Lin and W. D. Sproul, "Structure and properties of  $\text{Cr}_2\text{O}_3$  coatings deposited using DCMS, PDCMS, and DOMS," Surf. Coat. Technol. **276**, 70 (2015).
- <sup>140</sup> J. T. Gudmundsson, N. Brenning, D. Lundin, and U. Helmersson, "High power impulse magnetron sputtering discharge," J. Vac. Sci. Technol. A **30**, 030801 (2012).

- <sup>141</sup> R. Franz, C. Clavero, R. Bolat, R. Mendelsberg, and A. Anders, "Observation of multiple charge states and high ion energies in high-power impulse magnetron sputtering (HiPIMS) and burst HiPIMS using a LaB<sub>6</sub> target," *Plasma Sources Sci. Technol.* **23**, 035001 (2014).
- <sup>142</sup> P. M. Barker, S. Konstantinidis, E. Lewin, N. Britun, and J. Patscheider, "An investigation of c-HiPIMS discharges during titanium deposition," *Surf. Coat. Technol.* **258**, 631 (2014).
- <sup>143</sup> K. Bobzin, T. Brögelmann, N. C. Kruppe, and M. Engels, "Influence of dcMS and HPPMS in a dcMS/HPPMS hybrid process on plasma and coating properties," *Thin Solid Films* **620**, 188 (2016).
- <sup>144</sup> M. S. Kang, T.-g. Wang, J. H. Shin, R. Nowak, and K. H. Kim, "Synthesis and properties of Cr–Al–Si–N films deposited by hybrid coating system with high power impulse magnetron sputtering (HIPIMS) and DC pulse sputtering," *Transactions of Nonferrous Metals Society of China* **22**, **Supplement 3**, s729 (2012).
- <sup>145</sup> W. D. Sproul, P. J. Rudnik, M. E. Graham, and S. L. Rohde, "High rate reactive sputtering in an opposed cathode closed-field unbalanced magnetron sputtering system," *Surf. Coat. Technol.* **43/44**, 270 (1990).
- <sup>146</sup> K. E. Cooke, J. Hamsphire, W. Southall, and D. G. Teer, "The industrial application of pulsed DC bias power supplies in closed field unbalanced magnetron sputter ion plating," *Surf. Coat. Technol.* **177**, 789 (2004).
- <sup>147</sup> Y. P. Purandare, A. P. Ehasarian, and P. Eh Hovsepian, "Target poisoning during CrN deposition by mixed high power impulse magnetron sputtering and unbalanced magnetron sputtering technique," *J. Vac. Sci. Technol. A* **34**, 041502 (2016).
- <sup>148</sup> I. V. Svadkovski, D. A. Golosov, and S. M. Zavatskiy, "Characterisation parameters for unbalanced magnetron sputtering systems," *Vacuum* **68**, 283 (2002).
- <sup>149</sup> D. Carter, H. Walde, and K. Nauman, "Managing arcs in large area sputtering applications," *Thin Solid Films* **520**, 4199 (2012).
- <sup>150</sup> R. Ganesan, B. J. Murdoch, B. Treverrow, A. E. Ross, I. S. Falconer, A. Kondyurin, D. G. McCulloch, J. G. Partridge, D. R. McKenzie, and M. M. M. Bilek, "The role of pulse length in target poisoning during reactive HiPIMS: application to amorphous HfO<sub>2</sub>," *Plasma Sources Sci. Technol.* **24**, 035015 (2015).
- <sup>151</sup> R. Ganesan, B. Treverrow, B. Murdoch, D. Xie, A. E. Ross, J. G. Partridge, I. S. Falconer, D. G. McCulloch, D. R. McKenzie, and M. M. M. Bilek, "Duty cycle control in reactive high-power impulse magnetron sputtering of hafnium and niobium," *J. Phys. D: Appl. Phys.* **49**, 245201 (2016).

- 152 T. Shimizu, M. Villamayor, D. Lundin, and U. Helmersson, "Process stabilization by peak current regulation in reactive high-power impulse magnetron sputtering of hafnium nitride," *J. Phys. D: Appl. Phys.* **49**, 065202 (2016).
- 153 V. Tiron and L. Sirghi, "Tuning the band gap and nitrogen content of ZnOxNy thin films deposited by reactive HiPIMS," *Surf. Coat. Technol.* **282**, 103 (2015).
- 154 D. Benzeggouta, M. C. Hugon, and J. Bretagne, "Study of a HPPMS discharge in Ar/O<sub>2</sub> mixture: II. Plasma optical emission and deposited RuO<sub>x</sub> film properties," *Plasma Sources Sci. Technol.* **18**, 045026 (2009).
- 155 W.-Y. Wu, B.-H. Hsiao, P.-H. Chen, W.-C. Chen, C.-T. Ho, and C.-L. Chang, "CrNx films prepared using feedback-controlled high power impulse magnetron sputter deposition," *J. Vac. Sci. Technol. A* **32**, 02B115 (2014).
- 156 D. Lundin, M. Čada, and Z. Hubička, "Time-resolved ion flux and impedance measurements for process characterization in reactive high-power impulse magnetron sputtering," *J. Vac. Sci. Technol. A* **34**, 041305 (2016).
- 157 N. Britun, T. Minea, S. Konstantinidis, and R. Snyders, "Plasma diagnostics for understanding the plasma–surface interaction in HiPIMS discharges: a review," *J. Phys. D: Appl. Phys.* **47**, 224001 (2014).
- 158 J. Vlček, J. Rezek, J. Houška, T. Kozák, and J. Kohout, "Benefits of the controlled reactive high-power impulse magnetron sputtering of stoichiometric ZrO<sub>2</sub> films," *Vacuum* **114**, 131 (2015).
- 159 G. Greczynski, J. Lu, J. Jensen, S. Bolz, W. Kölker, C. Schiffrers, O. Lemmer, J. E. Greene, and L. Hultman, "A review of metal-ion-flux-controlled growth of metastable TiAlN by HIPIMS/DCMS co-sputtering," *Surf. Coat. Technol.* **257**, 15 (2014).
- 160 A. P. Ehasarian, A. Vetushka, Y. A. Gonzalvo, G. Safran, L. Szekely, and P. B. Barna, "Influence of high power impulse magnetron sputtering plasma ionization on the microstructure of TiN thin films," *J. Appl. Phys.* **109**, 104314 (2011).
- 161 P. E. Hovsepian, A. P. Ehasarian, and I. Petrov, "Structure evolution and properties of TiAlCN/VCN coatings deposited by reactive HIPIMS," *Surface and Coatings Technology* **257**, 38 (2014).
- 162 M. Lattemann, U. Helmersson, and J. E. Greene, "Fully dense, non-faceted 111-textured high power impulse magnetron sputtering TiN films grown in the absence of substrate heating and bias," *Thin Solid Films* **518**, 5978 (2010).

- <sup>163</sup> F. Magnus, A. S. Ingason, O. B. Sveinsson, S. Olafsson, and J. T. Gudmundsson, "Morphology of TiN thin films grown on SiO<sub>2</sub> by reactive high power impulse magnetron sputtering," *Thin Solid Films* **520**, 1621 (2011).
- <sup>164</sup> S. Shayestehaminzadeh, T. K. Tryggvason, L. Karlsson, S. Olafsson, and J. T. Gudmundsson, "The properties of TiN ultra-thin films grown on SiO<sub>2</sub> substrate by reactive high power impulse magnetron sputtering under various growth angles," *Thin Solid Films* **548**, 354 (2013).
- <sup>165</sup> S. Shayestehaminzadeh, E. B. Thorsteinsson, D. Primetzhofer, F. Magnus, and S. Olafsson, "Epitaxial and textured TiN thin films grown on MgO(1 0 0) by reactive HiPIMS: the impact of charging on epitaxial to textured growth crossover," *J. Phys. D: Appl. Phys.* **49**, 455301 (2016).
- <sup>166</sup> G. Greczynski, J. Jensen, and L. Hultman, "CrN<sub>x</sub> films prepared by DC magnetron sputtering and high-power pulsed magnetron sputtering: A comparative study," *IEEE Trans. Plasma Sci.* **38**, 3046 (2010).
- <sup>167</sup> G. Greczynski, J. Jensen, J. Böhlmark, and L. Hultman, "Microstructure control of CrN<sub>x</sub> films during high power impulse magnetron sputtering," *Surf. Coat. Technol.* **205**, 118 (2010).
- <sup>168</sup> J. Lin, W. D. Sproul, J. J. Moore, Z. L. Wu, and S. L. Lee, "Effect of negative substrate bias voltage on the structure and properties of CrN films deposited by modulated pulsed power (MPP) magnetron sputtering," *J. Phys. D: Appl. Phys.* **44**, 425305 (2011).
- <sup>169</sup> F. Ferreira, J. C. Oliveira, and A. Cavaleiro, "CrN thin films deposited by HiPIMS in DOMS mode," *Surf. Coat. Technol.* **291**, 365 (2016).
- <sup>170</sup> K. Bobzin, N. Bagcivan, S. Theiß, J. Trieschmann, R. H. Brugnara, S. Preissing, and A. Hecimovic, "Influence of Ar/Kr ratio and pulse parameters in a Cr-N high power pulse magnetron sputtering process on plasma and coating properties," *J. Vac. Sci. Technol. A* **32**, 021513 (2014).
- <sup>171</sup> Y. P. Purandare, A. P. Ehasarian, and P. E. Hovsepian, "Structure and properties of ZrN coatings deposited by high power impulse magnetron sputtering technology," *J. Vac. Sci. Technol. A* **29**, 011004 (2011).
- <sup>172</sup> Y. Purandare, A. Ehasarian, A. Santana, and P. Hovsepian, "ZrN coatings deposited by high power impulse magnetron sputtering and cathodic arc techniques," *J. Vac. Sci. Technol. A* **32**, 031507 (2014).
- <sup>173</sup> J.-R. Tsai, P.-C. Juan, and P.-J. Chen, "Characteristics of metal-gate metal-insulator-semiconductor capacitor with ZrN capping layer fabricated by high-power impulse magnetron sputtering," *Thin Solid Films* **618**, Part A, 55 (2016).

- <sup>174</sup> A. Tayal, M. Gupta, A. Gupta, V. Ganesan, L. Behera, S. Singh, and S. Basu, "Study of magnetic iron nitride thin films deposited by high power impulse magnetron sputtering," *Surf. Coat. Technol.* **275**, 264 (2015).
- <sup>175</sup> L. Mendizabal, R. Bayón, E. G-Berasategui, J. Barriga, and J. J. Gonzalez, "Effect of N<sub>2</sub> flow rate on the microstructure and electrochemical behavior of TaN<sub>x</sub> films deposited by modulated pulsed power magnetron sputtering," *Thin Solid Films* **610**, 1 (2016).
- <sup>176</sup> A. Guillaumot, F. Lapostolle, C. Dublanche-Tixier, J. C. Oliveira, A. Billard, and C. Langlade, "Reactive deposition of Al-N coatings in Ar/N<sub>2</sub> atmospheres using pulsed-DC or high power impulse magnetron sputtering discharges," *Vacuum* **85**, 120 (2010).
- <sup>177</sup> C.-T. Chang, Y.-C. Yang, J.-W. Lee, and B.-S. Lou, "The influence of deposition parameters on the structure and properties of aluminum nitride coatings deposited by high power impulse magnetron sputtering," *Thin Solid Films* **57**, 161 (2014).
- <sup>178</sup> K. A. Aissa, A. Achour, O. Elmazria, Q. Simon, M. Elhosni, P. Boulet, S. Robert, and M. A. Djouadi, "AlN films deposited by dc magnetron sputtering and high power impulse magnetron sputtering for SAW applications," *Journal of Physics D: Applied Physics* **48**, 145307 (2015).
- <sup>179</sup> J. Lin and R. Chistyakov, "C-axis orientated AlN films deposited using deep oscillation magnetron sputtering," *Appl. Surf. Sci.* **396**, 129 (2017).
- <sup>180</sup> M. Junaid, D. Lundin, J. Palisaitis, C.-L. Hsiao, V. Darakchieva, J. Jensen, P. O. A. Persson, P. Sandstrom, W.-J. Lai, L.-C. Chen, K.-H. Chen, U. Helmersson, L. Hultman, and J. Birch, "Two-domain formation during the epitaxial growth of GaN (0001) on c-plane Al<sub>2</sub>O<sub>3</sub> (0001) by high power impulse magnetron sputtering," *J. Appl. Phys.* **110**, 123519 (2011).
- <sup>181</sup> S. Schmidt, T. Hänninen, C. Goyenola, J. Wissting, J. Jensen, L. Hultman, N. Goebbels, M. Tobler, and H. Högberg, "SiN<sub>x</sub> coatings deposited by reactive high power impulse magnetron sputtering: Process parameters influencing the nitrogen content," *ACS Applied Materials & Interfaces* **8**, 20385–20395 (2016).
- <sup>182</sup> H. Elmkhah, T. F. Zhang, A. Abdollah-zadeh, K. H. Kim, and F. Mahboubi, "Surface characteristics for the TiAlN coatings deposited by high power impulse magnetron sputtering technique at the different bias voltages," *Journal of Alloys and Compounds* **688, Part A**, 820 (2016).
- <sup>183</sup> G. Greczynski, J. Lu, M. Johansson, J. Jensen, I. Petrov, J. E. Greene, and L. Hultman, "Selection of metal ion irradiation for controlling Ti<sub>1-x</sub>Al<sub>x</sub>N alloy growth via hybrid HIPIMS/magnetron co-sputtering," *Vacuum* **86**, 1036 (2012).



- 184 G. Greczynski, J. Lu, M. P. Johansson, J. Jensen, I. Petrov, J. E. Greene, and L. Hultman, "Role of  $Ti^{n+}$  and  $Al^{n+}$  ion irradiation ( $n = 1, 2$ ) during  $Ti_{1-x}Al_xN$  alloy film growth in a hybrid HIPIMS/magnetron mode," *Surf. Coat. Technol.* **206**, 4202 (2012).
- 185 Y.-C. Hsiao, J.-W. Lee, Y.-C. Yang, and B.-S. Lou, "Effects of duty cycle and pulse frequency on the fabrication of AlCrN thin films deposited by high power impulse magnetron sputtering," *Thin Solid Films* **549**, 281 (2013).
- 186 M. Wiesing, T. d. I. Arcos, and G. Grundmeier, "The thermal oxidation of TiAlN high power pulsed magnetron sputtering hard coatings as revealed by combined ion and electron spectroscopy," *Adv. Mater. Interfaces* (**vol. not yet assigned**), 1600861 (2017).
- 187 N. Bagcivan, K. Bobzin, G. Grundmeier, M. Wiesing, O. Ozcan, C. Kunze, and R. H. Brugnara, "Influence of HPPMS pulse length and inert gas mixture on the properties of (Cr,Al)N coatings," *Thin Solid Films* **549**, 192 (2013).
- 188 J. Lin, B. Wang, Y. Ou, W. D. Sproul, I. Dahan, and J. J. Moore, "Structure and properties of CrSiN nanocomposite coatings deposited by hybrid modulated pulsed power and pulsed dc magnetron sputtering," *Surf. Coat. Technol.* **216**, 251 (2013).
- 189 H. Klostermann, F. Fietzke, R. Labitzke, T. Modes, and O. Zywitzki, "Zr-Nb-N hard coatings deposited by high power pulsed sputtering using different pulse modes," *Surf. Coat. Technol.* **204**, 1076 (2009).
- 190 Q. Ma, L. Li, Y. Xu, J. Gu, L. Wang, and Y. Xu, "Effect of bias voltage on TiAlSiN nanocomposite coatings deposited by HiPIMS," *Appl. Surf. Sci.* **392**, 826 (2017).
- 191 K. Bobzin, N. Bagcivan, P. Immich, S. Bolz, H. G. Fuß, and R. Cremer, "Properties of (Ti,Al,Si)N coatings for high demanding metal cutting applications deposited by HPPMS in an industrial coating unit," *Plasma Processes and Polymers* **6**, S124 (2009).
- 192 T. F. Zhang, Q. M. Wang, J. Lee, P. Ke, R. Nowak, and K. H. Kim, "Nanocrystalline thin films synthesized from a  $Ti_2AlN$  compound target by high power impulse magnetron sputtering technique," *Surf. Coat. Technol.* **212**, 199 (2012).
- 193 P. E. Hovsepian, A. P. Ehasarian, A. Deeming, and C. Schimpf, "VMeCN based nanoscale multilayer PVD coatings deposited by the combined high power impulse magnetron sputtering/unbalanced magnetron sputtering technology," *Plasma Processes and Polymers* **4**, S897 (2007).
- 194 Y. X. Ou, J. Lin, S. Tong, W. D. Sproul, and M. K. Lei, "Structure, adhesion and corrosion behavior of CrN/TiN superlattice coatings deposited by the combined deep oscillation magnetron sputtering and pulsed dc magnetron sputtering," *Surf. Coat. Technol.* **293**, 21 (2016).

- <sup>195</sup> Y. X. Ou, J. Lin, H. L. Che, J. J. Moore, W. D. Sproul, and M. K. Lei, "Mechanical and tribological properties of CrN/TiN superlattice coatings deposited by a combination of arc-free deep oscillation magnetron sputtering with pulsed dc magnetron sputtering," *Thin Solid Films* **594, Part A**, 147 (2015).
- <sup>196</sup> Y. X. Ou, J. Lin, S. Tong, H. L. Che, W. D. Sproul, and M. K. Lei, "Wear and corrosion resistance of CrN/TiN superlattice coatings deposited by a combined deep oscillation magnetron sputtering and pulsed dc magnetron sputtering," *Appl. Surf. Sci.* **351**, 332 (2015).
- <sup>197</sup> P. E. Hovsepian, A. P. Ehasarian, Y. P. Purandare, B. Biswas, F. J. Pérez, M. I. Lasanta, M. T. de Miguel, A. Illana, M. Juez-Lorenzo, R. Muelas, and A. Agüero, "Performance of HIPIMS deposited CrN/NbN nanostructured coatings exposed to 650 °C in pure steam environment," *Materials Chemistry and Physics* **179**, 110 (2016).
- <sup>198</sup> C. Nouvellon, M. Michiels, J. P. Dauchot, C. Archambeau, F. Laffineur, E. Silberberg, S. Delvaux, R. Cloots, S. Konstantinidis, and R. Snyders, "Deposition of titanium oxide films by reactive High Power Impulse Magnetron Sputtering (HiPIMS): Influence of the peak current value on the transition from metallic to poisoned regimes," *Surf. Coat. Technol.* **206**, 3542 (2012).
- <sup>199</sup> P. J. Kelly, P. M. Barker, S. Ostovarpour, M. Ratova, G. T. West, I. Iordanova, and J. W. Bradley, "Deposition of photocatalytic titania coatings on polymeric substrates by HiPIMS," *Vacuum* **86**, 1880 (2012).
- <sup>200</sup> S. Konstantinidis, J. P. Dauchot, and M. Hecq, "Titanium oxide thin films deposited by high-power impulse magnetron sputtering," *Thin Solid Films* **515**, 1182 (2006).
- <sup>201</sup> W. Schönberger, H. Bartsch, S. Schippel, and T. Bachmann, "Deposition of rutile TiO<sub>2</sub> films by pulsed and high power pulsed magnetron sputtering," *Surf. Coat. Technol.* **293**, 16 (2016).
- <sup>202</sup> E. Lecoq, J. Guillot, D. Duday, J.-B. Chemin, and P. Choquet, "Elaboration of a wide range of TiO<sub>2</sub> micro/nanostructures by high power impulse inverted cylindrical magnetron sputtering," *J. Phys D: Appl. Phys.* **47**, 195201 (2014).
- <sup>203</sup> D. Benzeggouta, M. C. Hugon, J. Bretagne, and M. Ganciu, "Study of a HPPMS discharge in Ar/O<sub>2</sub> mixture: I. Discharge characteristics with Ru cathode," *Plasma Sources Sci. Technol.* **18**, 045025 (2009).
- <sup>204</sup> J. P. Fortier, B. Baloukas, O. Zabeida, J. E. Klemberg-Sapieha, and L. Martinu, "Thermochromic VO<sub>2</sub> thin films deposited by HiPIMS," *Solar Energy Materials and Solar Cells* **125**, 291 (2014).
- <sup>205</sup> S. Loquai, B. Baloukas, J. E. Klemberg-Sapieha, and L. Martinu, "HiPIMS-deposited thermochromic VO<sub>2</sub> films with high environmental stability," *Solar Energy Materials and Solar Cells* **160**, 217 (2017).

- <sup>206</sup> T. Lin, L. Wang, X. Wang, Y. Zhang, and Y. Yu, "Influence of bias voltage on microstructure and phase transition properties of VO<sub>2</sub> thin film synthesized by HiPIMS," *Surf. Coat. Technol.* **305**, 110 (2016).
- <sup>207</sup> W. D. Sproul, D. J. Christie, and D. C. Carter, "The reactive sputter deposition of aluminum oxide coatings using high power pulsed magnetron sputtering (HPPMS)," 47th Ann. Techn. Conf. Proc., Dallas, TX, 2004 (Society of Vacuum Coaters), p. 96.
- <sup>208</sup> M. Hála, R. Vernhes, O. Zabeida, E. Bousser, J. E. Klemberg-Sapieha, R. Sargent, and L. Martinu, "Growth and properties of high index Ta<sub>2</sub>O<sub>5</sub> optical coatings prepared by HiPIMS and other methods," *Surf. Coat. Technol.* **241**, 33 (2014).
- <sup>209</sup> K. Sarakinos, J. Alami, C. Klever, and M. Wuttig, "Process stabilization and enhancement of deposition rate during reactive high power pulsed magnetron sputtering of zirconium oxide," *Surf. Coat. Technol.* **202**, 5033 (2008).
- <sup>210</sup> X. Zhao, J. Jin, J.-C. Cheng, J.-W. Lee, K.-H. Wu, and K.-C. Liu, "Effect of pulsed off-times on the reactive HiPIMS preparation of zirconia thin films," *Vacuum* **118**, 38 (2015).
- <sup>211</sup> S. Sørderby, A. Aijaz, U. Helmersson, K. Sarakinos, and P. Eklund, "Deposition of yttria-stabilized zirconia thin films by high power impulse magnetron sputtering and pulsed magnetron sputtering," *Surf. Coat. Technol.* **240**, 1 (2014).
- <sup>212</sup> S. Sørderby, B. H. Christensen, K. P. Almqvist, L. P. Nielsen, and P. Eklund, "Industrial-scale high power impulse magnetron sputtering of yttria-stabilized zirconia on porous NiO/YSZ fuel cell anodes," *Surf. Coat. Technol.* **281**, 150 (2015).
- <sup>213</sup> S. Kment, Z. Hubicka, J. Krysa, J. Olejnick, M. Cada, I. Gregora, M. Zlamal, M. Brunclikova, Z. Remes, N. Liu, L. Wang, R. Kirchgeorg, C. Y. Lee, and P. Schmuki, "High-power pulsed plasma deposition of hematite photoanode for PEC water splitting," *Catalysis Today* **230**, 8 (2014).
- <sup>214</sup> S. Konstantinidis, A. Hemberg, J. P. Dauchot, and M. Hecq, "Deposition of zinc oxide layers by high-power impulse magnetron sputtering," *J. Vac. Sci. Technol. B* **25**, L19 (2007).
- <sup>215</sup> J. Vlček, A. Belosludtsev, J. Rezek, J. Houška, J. Čapek, R. Čerstvý, and S. Haviar, "High-rate reactive high-power impulse magnetron sputtering of hard and optically transparent HfO<sub>2</sub> films," *Surf. Coat. Technol.* **290**, 58 (2016).
- <sup>216</sup> A. Hemberg, J.-P. Dauchot, R. Snyders, and S. Konstantinidis, "Evaporation-assisted high-power impulse magnetron sputtering: The deposition of tungsten oxide as a case study," *J. Vac. Sci. Technol. A* **30**, 040604 (2012).

- <sup>217</sup> J. Olejníček, M. Brunclíková, Š. Kment, Z. Hubička, H. Kmentová, P. Kšířová, M. Čada, M. Zlámal, and J. Krýsa, "WO<sub>3</sub> thin films prepared by sedimentation and plasma sputtering," *Chem. Eng. J.*, DOI 10.1016/j.cej.2016.09.083 (2017).
- <sup>218</sup> F. Horstmann, V. Sittinger, and B. Szyszka, "Heat treatable indium tin oxide films deposited with high power pulse magnetron sputtering," *Thin Solid Films* **517**, 3178 (2009).
- <sup>219</sup> C.-H. Wu, F.-C. Yang, W.-C. Chen, and C.-L. Chang, "Influence of oxygen/argon reaction gas ratio on optical and electrical characteristics of amorphous IGZO thin films coated by HiPIMS process," *Surf. Coat. Technol.* **303**, Part A, 209 (2016).
- <sup>220</sup> M. Mikan, U. Helmersson, H. Rinnert, J. Ghanbaja, D. Muller, and D. Horwat, "Room temperature deposition of homogeneous, highly transparent and conductive Al-doped ZnO films by reactive high power impulse magnetron sputtering," *Solar Energy Materials and Solar Cells* **157**, 742 (2016).
- <sup>221</sup> D. Horwat, M. Mikan, and W. Chamorro, "New strategies for the synthesis of ZnO and Al-doped ZnO films by reactive magnetron sputtering at room temperature," *Phys. Status Solidi C* **13**, 951 (2016).
- <sup>222</sup> M. Hála, R. Vernhes, O. Zabeida, J.-E. Klemberg-Sapieha, and L. Martinu, "Reactive HiPIMS deposition of SiO<sub>2</sub>/Ta<sub>2</sub>O<sub>5</sub> optical interference filters," *J. Appl. Phys.* **116**, 213302 (2014).
- <sup>223</sup> K. Bobzin, T. Brögelmann, G. Grundmeier, T. de los Arcos, M. Wiesing, and N. C. Kruppe, "(Cr,Al)N/(Cr,Al)ON oxy-nitride coatings deposited by hybrid dcMS/HPPMS for plastics processing applications," *Surf. Coat. Technol.* **308**, 394 (2016).
- <sup>224</sup> T. Hänninen, S. Schmidt, J. Jensen, L. Hultman, and H. Högberg, "Silicon oxynitride films deposited by reactive high power impulse magnetron sputtering using nitrous oxide as a single-source precursor," *J. Vacuum Sci. Technol. A* **33**, 05E121 (2015).
- <sup>225</sup> H. Högberg, L. Tengdelius, M. Samuelsson, F. Eriksson, E. Broitman, J. Lu, J. Jensen, and L. Hultman, "Reactive sputtering of  $\delta$ -ZrH<sub>2</sub> thin films by high power impulse magnetron sputtering and direct current magnetron sputtering," *J. Vac. Sci. Technol. A* **32**, 041510 (2014).
- <sup>226</sup> A. Halbe, P. Johnson, S. Jackson, R. Weiss, U. Avachat, A. Welsh, and A. P. Ehasarian, "High efficiency copper indium gallium diselenide (CIGS) by high power impulse magnetron sputtering (HIPIMS): A promising and scalable application in thin-film photovoltaics," *MRS Proc.* **1210**, 1210\_Q06\_09 (2009).
- <sup>227</sup> S. Schmidt, C. Goyenola, G. K. Gueorguiev, J. Jensen, G. Greczynski, I. G. Ivanov, Z. Czigány, and L. Hultman, "Reactive high power impulse magnetron sputtering of CF<sub>x</sub> thin films in mixed Ar/CF<sub>4</sub> and Ar/C<sub>4</sub>F<sub>8</sub> discharges," *Thin Solid Films* **542**, 21 (2013).

- <sup>228</sup> S. Schmidt, Z. Czigány, J. Wissting, G. Greczynski, E. Janzén, J. Jensen, I. G. Ivanov, and L. Hultman, "A comparative study of direct current magnetron sputtering and high power impulse magnetron sputtering processes for CN<sub>x</sub> thin film growth with different inert gases," *Diamond and Related Materials* **64**, 13 (2016).
- <sup>229</sup> T. Kimura, H. Kamata, S. Nakao, and K. Azuma, "Preparation of titanium-doped diamond-like carbon films with electrical conductivity using high power pulsed magnetron sputtering system with bipolar pulse voltage source for substrate," *IEEE Trans. Plasma Sci.* **44**, 3083 (2016).